Robotic Granular Jamming

Jiang, Allen

Awarding institution:
King's College London

KING'S College LONDON

University of London

Robotic Granular Jamming

by Allen Jiang

A thesis submitted in partial fulfillment of the requirements for the degree of
'Doctor of Philosophy' in Robotics

to

King's College London
University of London
School of Natural and Mathematical Sciences
Department of Informatics
Centre for Robotics Research

June 2014

I herewith declare that I have produced this PhD thesis without the prohibited assistance of third parties and without making use of aids other than those specified; notions taken over directly or indirectly from other sources have been identified as such. This PhD thesis has not previously been presented in identical or similar form to any other British or foreign examination board.

London, June 2014

Acknowledgements

A PhD is a journey. It's difficult road traveled by the candidate, yet never alone. There are many who have supported me during this three year adventure. On a personal level, I have to thank my friends and family for telling me to "add oil," a Chinese phrase which translates to "keep going" and "don't give up." In particular, I thank my parents Tsang Ming and Hui Ju Jiang for their support, both during my PhD and my life leading up to it. I also would like to thank my two hilarious brothers Andrew and Anthony for bringing me back down to earth, when I've received too much praise for my work. I also thank my other half, Connie Qian for everything.

Of course, I have to give my sincerest gratitude towards my great supervisors:
Thrishantha Nanayakkara, Kaspar Althoefer, and Prokar Dasgupta. Ultimately, it was through their guidance and support that made this PhD possible. I was probably the most expensive PhD student they've supervised to date. So, I must also thank them greatly for their aid and providing me a means to dedicate my energy directly into research.

That said, I must also acknowledge the following funding bodies: the Guy's and St Thomas' Hospital Trust Foundation under grant code R090705 in the framework of the

GSTT Charity Award - Developing Clinician-Scientific Interfaces in Robotic Assisted Surgery; the Engineering and Physical Sciences Research Council (EPSRC), UK, under grant agreements EP/I028773/1 and EP/I028757/1 (REINS); and by the Seventh Framework Programme of the European Commission under grant agreements 287728, 270138, 231640, and 246371 in the framework of EU projects STIFF-FLOP, DARWIN, HANDLE, and COSMOS, respectively. Additionally, I would like to acknowledge my collaborators at Scuola Superiore Sant'Anna (SSSA), University College London (UCL), and the Tokyo Institute of Technology (TITECH).

I would also like to thank my colleagues for their collaborative efforts and suggestions. In particular, I thank Tommaso Ranzani, Tomaso Aste, Hui Xie, Min Li, Helge Wurdemann, Angela Faragasso, Joao Bimbo, Toshio Takayama, Giada Gerboni, and Ali Ataollahi. I would also like to acknowledge the hard work put in by the undergraduate and master-level students I supervised: Samson, Palash, Rocio, Fey, Laura, George, Nader, and David. The comprehensiveness of the experiments could not have been performed without their assistance.

Abstract

Granular jamming is a phenomenon where discrete granules can transition their macro behavior between a fluid-like and a solid-like state. In the context of soft robotics, this thesis examines granular jamming in three key aspects. The first aspect investigates the modeling of the granule behavior as it is jammed and unjammed. A simplified model was developed where the macro stiffness of the granules in different states is encompassed in one variable, E. In an engineering context, the usage of this one variable enables structures of different types to be quantitatively compared. The second aspect investigates the structure of mechanisms using granule jamming. For the granules, experiments were performed on different shapes, sizes, and materials. The results show that there can be a significant change in the stiffness range and profile when a parameter of the granule is changed. The properties of the membrane holding the granules and properties of the interparticle fluid were also studied for their affect on the behavior of the stiffnesses. For the membrane, the boundary layer applying the external stress, different materials and designs were found to have as much as a significant impact as changing granule type. For the interparticle fluid, the effects of air and water as the inter-granule fluid were compared, which showed that there is no significant difference between the stiffness range. However, the use of water can shrink the transition region between the fluid-like and solid-

like states of granular behavior. While this smaller transition region limits the tunability of compliance for a granular jamming mechanism, it gives the added benefit of requiring less volume of fluid to create vacuum, due to the incompressibility to water. This effectively untethers granular jamming mechanisms from cumbersome vacuum pumps, a key step in mobilizing the technology in the context of robotics. Lastly, this thesis focuses on the aspect of control for granular jamming. This encompasses the development of granular jamming-based actuators and the control of those actuators though impedance control.

Contents

List of Figures

List of Tables

Chapter 1

Introduction

Abstract

Jamming is a phenomenon where particulate matter can transition between fluid-like and solid-like states. This thesis focuses on the application of granular jamming to robotics. In particular, the effects of granule size, shape, and material, along with the effects of the boundary conditions, are studied to design a variable stiffness flexible manipulator. Further investigations on the difference between dry and wet granules are also performed.

1.1 Introduction

Medical robotics today is making use of a variety of robotic types, from the rigid robotic arms for minimally invasive surgeries (MIS) to flexible endoscopes for natural orifice transluminal endoscopic surgery (NOTES). While the success rate between traditional laparoscopic surgery and robot assisted laparoscopic surgery is similar, patients who have undergone robotic surgery recover significantly faster and incur lower costs [1, 2]. However, while these systems are good for MIS, they still have several drawbacks in surgeries designed to be even less invasive, such as NOTES [3] and laparo-endoscopic single-site surgery (LESS). Rigid robotics, such as the da Vinci robot, are difficult to use in these surgeries because the instruments clash with each other [4]. On the other hand, while flexible endoscopes provide increased maneuverability and require fewer Trocar ports, they have lower platform stability than their rigid counterparts and visualization which is not independent of the instruments [5, 6]. Thus, to take advantage of the stability and performance of rigid robotics as well as the maneuverability and access requirements of a flexible system, a variable stiffness robot is a clear contender.

There are several mechanisms for stiffness control, one of which is granular jamming. Granular jamming is a phenomenon where a system of particles, which normally behaves like a fluid, can transition into a solid-like state [7, 8]. Jamming occurs when the maximum packing concentration is reached and a subset of the particles are in contact to form a stress-bearing network. A classic example is a sand castle. When packed tightly and "jammed," the grains retain a structure, rather than flow and crumble. In this instance, the shape of the sand grains affect the level of jamming which can occur. Likewise, an interparticle fluid like water can also affect the level of jamming by adding cohesion to the grains. Another example would be vacuum packed rice or coffee. When encased in an air-tight wrap and vacuumed, the granules become jam packed and the whole package

rigidifies. Upon opening the package, the granules become more loosely packed, transitioning the system to a soft, fluid-like state. This thesis investigates the driving factors in granular jamming for robotic applications. In Chapter 4, the effects of granule properties are investigated, such as shape, size, and material. In Chapter 5, the effects of the outer membrane material is investigated. Then, in Chapter 6, the difference between air and water as interparticle fluids is investigated.

Granular jamming itself is only a variable stiffness mechanism, not an actuator. Thus, additional research was done with granular-jamming based actuators for minimally invasive surgical applications. More constraints are placed on actuators in magnetic resonance imaging (MRI) environments, where electric and piezoceramic motors can cause interference with the MRI scanner [9, 10]. Thus, pneumatic actuators are considered ideal MR-compatible actuators for their decoupling with electromagnetism [11]. Moreover, pneumatic actuators have lightweight and compliant structures, making them a popular choice for general robotics [12]. However, pneumatic actuators and muscles cannot control their inherent stiffness or impedance when unactuated.

To provide pneumatic actuators with stiffness or impedance control, granular media is filled within the actuator membrane. When pressurized with positive pressure, the granules neither contribute nor hinder the performance of the actuator. However, when vacuumed, the actuator increases in rigidity via granular jamming. This is discussed in greater detail in Chapter 7.

1.2 Aims and Objectives

Project Aim

This research aims to develop a snake-like soft robot for minimally invasive surgeries. This includes the development of soft actuators and variable stiffness mechanisms.

Project Objectives

- **Develop a variable stiffness mechanism which can be independently controlled.**
  Often tendon-driven and pre-curved tubes can be used as variable stiffness mechanisms for snake-like robots. However, while each section of the robot can exhibit a different stiffness, the stiffness of the tip is dependent of the stiffness at the base. Thus, a system in which the tip can be rigid while the base is soft, is the objective of the proposed technology.

- **Develop the stiffness mechanism to exhibit a range of stiffnesses which can be dynamically tuned.**
  Some variable stiffness mechanisms are binary in nature, where they can transition only between soft and rigid behaviors. This technology should be able to exhibit a range of stiffnesses to dynamically control the impedance of the robot.

- **Develop the mechanism to meet minimally invasive surgery criteria.**
  The developed mechanism should be miniaturizable to fit in standard Trocar port sizes of 15 mm or less. It should also be made of materials which can be sterilized with conventional methods.

1.3 Research Contributions

This work gave rise to many research publications, including 3 journal submissions, 9 peer-reviewed international conference papers (IEEE IROS, ASME IDETC, IEEE EMBC, AIP P&G, Hamlyn, and WCE), and 2 workshop papers. A full list of publications can be found in Appendix A.

Contribution to the Science of Flexible Robotics

As flexible and soft robotics gains traction, new mechanisms must be developed to enable soft robots to perform meaningful tasks. The research into robotic granular jamming in this thesis provides the field of flexible robotics with a fundamental foundation. The use of granular media creates robots which can bend and squeeze into tight spaces, while also being able to stiffen and articulate to perform tasks. This thesis underlines key features in a granular jamming system which give rise to its ability to operate in robotic applications. Novel contributions to the field include the following:

- Modeling for engineering: The variable E, the elastic modulus, is used loosely to represent the stiffness of a granule filled cantilever. Introduced in Chapter 3, this approximation enables granular jamming mechanisms of different designs to be quantitatively compared, as shown in subsequent chapters.

- Granular material: Experiments were performed to identify the impact of different particle parameters on the stiffness range of a jammed and unjammed system. The results given in Chapter 4 show that the size and shape of the granules impact the jamming performance, stiffness of the individual particles dictate the stiffness of the macro system, and an increase in surface friction can increase stiffness and improve hysteresis. Chapter 4 also shows experiments on the coupling of granules,

an area largely unexplored.

- Membrane significance: Chapter 5 shows that the membrane material and design can significantly impact the granular jamming behavior. This is most predominately seen when comparing a thin, latex membrane to a thicker, non-elastic plastic. The plastic dramatically increases the stiffness range of the system. A novel investigation on coupling the membrane with the granules showed that hysteresis can be improved by the design of the membrane.

- Inteparticle fluid: Typically air fills the gaps between granules and is evacuated to create vacuum pressure. However, Chapter 6 shows that the use of incompressible fluids, such as water, as the interparticle fluid can unetether mechanisms from vacuum pumps in favor of smaller, more mobile syringe pumps.

- Variable stiffness actuators: Chapter 7 introduces prototypes for novel soft actuators which can also change stiffness.

- Controlling uncertain systems: Chapter 8 demonstrates how the variability in granular jamming systems can be compensated by the use of visual servoing. Additionally, the chapter introduces a model-free adaptive controller that can be used to control the impedance of the robot to its environment.

This thesis also investigates granular jamming triaxially, where experiments measure the granular jamming system in bending, tension, and compression, another first in the field of flexible robotics.

Chapter 2

Background and Related Work

Abstract

This chapter introduces the field of flexible manipulators, snake-like, and tentacle-like robots in the context of medical robotics. It then provides a background of these robot types with variable stiffness designs. Lastly, the chapter discusses the background and previous work of granular jamming, a variable stiffness mechanism for flexible and soft robotics.

2.1 Introduction

Current medical robotics, particularly surgical manipulators, reduce patient trauma after operations, but have rigid arms which limit their dexterity, or range of motion. In particular, laparoscopic surgeries, also known as minimally invasive surgeries (MIS), use flexible manipulators to deploy sensors and surgical tools through one to three key holes in the patient. Nonetheless, while it has been beneficial to insert cameras or tactile sensors into the body, most laparoscopic tools lack the ability to wrap around an organ, let alone remain compliant enough to not disturb it. Robots like the da Vinci robot are limited to operating on one side of the organ, whereas a continuum or highly articulated manipulator may operate from behind the organ, as well [4]. Proposed here is a novel new flexible manipulator design, which uses granular jamming in the joints of a highly articulated robot, to serve as a surgical tool which can exhibit compliance or rigidity.

2.2 Flexible Manipulator Designs

The contemporary field of flexible manipulators is dominated by two major types of designs, continuum robots [13, 14, 15, 16, 14] and highly articulated robots [17, 18]. Continuum robots are typically tendon or rod driven, though they can also be pneumatic or hydraulic. The main principle behind continuum serpentine robots is to actuate a spine-like structure with a mechanical muscle or tendon. Though the most common type of flexible manipulator, tendon driven systems, generally suffer from backlash and large external footprints [19, 20]. Tendon driven robots can achieve some degree of variable stiffness by tensioning or slacking wires, but the stiffness of the tip cannot be greater than the stiffness at the base. Highly articulated robots, on the other hand, use motor-driven jointed segments for actuation. Because a motor is required to drive each degree

of freedom (DOF) at each joint, highly articulated robots tend to be much larger than their continuum counterparts. Flexible manipulators like the I-snake by Imperial College London [18] and the Highly Articulated Robot Probe (HARP) by Carnegie Mellon University [21] are already making significant headway in the field of flexible manipulators. However, both types of robots, as well as the Da Vinci surgical robot, are unable to vary the stiffness along the length of the manipulator. This makes it difficult for them to operate around moving organs like the heart, where compliance is more preferable than rigidity. These robots also have limitations to the degrees of freedoms (DOF) they can exhibit, as the Carnegie Mellon HARP is limited to the number of rods that can be used for bending and the Imperial I-snake only has one DOF at each joint.

2.3 Variable Stiffness Designs

It is important to develop a robot manipulator which can vary its stiffness, because perfectly rigid and semi-rigid instruments cause clashing at the entry point [4]. The ability to squeeze and bend, while being able to rigidify when required, would be a better solution because it applies less stress on the body [22]. In terms of variable stiffness manipulators, various joint prototypes have been developed in the scientific community. These designs typically rely on spring tensioning to stiffen a particular joint [23, 24]. However, such designs require at least one dedicated motor for each degree of freedom to be stiffened, meaning each joint may need an additional one or two motors to control its stiffness.
A group in this field developed a soft robot based on thermally activated joints, in which a solder-based mechanism is used to lock and release joints [25]. This technique has a limited ability to vary level the stiffness. In other words, the solder is either fully rigid or completely soft, as opposed to partially rigid. Other groups have created manipulators which consist of pre-curved concentric tubes [26, 27]. This design uses a series of

telescopic cannula tubes of varying stiffness to extend the distal tip of the robot. The combination of the pre-curved tubes and stiffnesses can create different shapes and rigidities [16]. However, like tendon driven systems, the segments near the tip of the manipulator must be less stiff than the preceding segments. While the concentric tubes do benefit from small diameters, the inherent design of the robot cannot quickly adapt and requires a good map of its environment. One group created a variable stiffness continuum robot based on layer jamming, where a spiral of overlapping scales under a flexible membrane can be stiffened via vacuum pressure [28]. This design benefits from a hollow core, useful for passing tools to a target at the distal tip. However, the drawback is its limited curvature, as the scales must remain overlapped.

2.4 Granular Jamming

Building upon the pioneering work by Heinrich Jaefer, Tomaso Aste, and Andrea Liu, this thesis proposes to use bead-filled columns to control the stiffness of each joint based on the granular jamming principle. The columns surround each joint linkage; and when they are partially inflated, then the joints are soft, malleable, and can be compliantly manipulated with an external device. When air is evacuated from the column, the beads compress together, and the geometric shape and friction between beads will cause them to lock in place, rigidifying the joint at the given orientation [29]. The main advantage of this design is that just one column would be required to control the stiffness of a two DOF joint. Furthermore, every joint can be linked to a single pipeline, and joints can independently vary their stiffness with a micro-valve.

This set up can be used for scaffolding purposes, known as a retractor, and is similar to the Vacu-SL endoscope developed by the Delft University of Technology [22]. When in its compliant state, doctors can deform and position the manipulator inside the patient.

When the air is evacuated from the manipulator, the rigidified structure will serve as a scaffold to support the body cavity, such as holding up hanging organs or fat. Unlike the Vacu-SL endoscope, which engages the entire manipulator with the same stiffness, the proposed design can control and vary the rigidity along the manipulator. In other terms, this manipulator would be able to have rigid ends and a soft middle. While the rigid ends are performing tasks, the soft middle would absorb movements from beating organs.

By adding positive pressure to the columns in the multiple column design found in Fig. 7.1, actuation can be achieved. With a braided sleeve around each column, the variable stiffness elements would double as McKibben actuators. Using pulse-modulated valves for each column, the manipulator can be both actuated and varied in stiffness with a single pump. In a laparoscopic setting, this type of mechanism not only has the benefit of compliance and passivity, but can also be designed to be compatible with magnetic resonance imaging (MRI), by utilizing passive, one-way, rubber valves.

Work with granular jamming has been initially studied by other groups, most notably with the universal robotic gripper [29], a tendon-actuated elephant trunk-like manipulator [30], and a deformable ball robot [31]. Additional research has been done by [32] for an emergency vacuum splint, [6, 22] for an endoscopic device, and [33, 34, 35] for haptic devices. However, these works only give preliminary discussions on the driving factors of granular jamming's stiffness range, hysteresis, and variability. Likewise, the robots developed by previous groups primarily use granular jamming as a variable stiffness mechanism in conjunction with tendons or other actuators. Preliminary work on integration between pneumatic actuators and granular jamming have been explored by [36] and [37], but are either not applicable to a snake-like robot or not truly an integration between pneumatic actuators and granular jamming.

Chapter 3

Modeling Robotic Granular Jamming

Abstract

Understanding the interaction between particles in different states is a difficult problem. Physicists, chemical engineers, civil engineers, and now roboticists are interested in understanding the effects of particle friction, stiffness, damping, and geometry for both particle-scale interactions and macro-scale behavior. This chapter describes the common correlations used to model a robotic granular jamming system in two main ways. First is to use packing factor and friction models to estimate the jamming stiffness at the granule level, and the second is to reduce the model by taking a macroscopic view. This second approach reduces the model by encompassing the variables which contribute to the jamming stiffness into a single variable E, an elastic modulus. The aim is to eventually use simulations to design granules and membranes, as well as provide a measure to which different granular systems can be quantitatively compared.

3.1 Introduction

Granular jamming is a subsection of soft matter physics and fluid mechanics, where interactions between granules are investigated. Research in this area is primarily done by physicists. However, as granules make up some 70% of industrial processes such as mining, construction, agriculture, metals, and pharmaceuticals, the study of particles are also of interest to civil, chemical, and mechanical engineers. With the introduction of granular jamming as a variable stiffness mechanism, granular systems and granular flows are becoming a growing interest to roboticists.

Simulations have also been done by several other groups, most notably [38, 39, 40, 41, 42] and [43]. Based on their work, this chapter describes various means to model granular packing and jamming. First, Section 3.2 covers the means to calculate the packing factor of granules within a volume and physics-based equations on particle contacts. Then, Section 3.3 covers a macro-scopic view of method of modeling granular jamming, where the entire structure–granules and membrane–are examined as one object.

3.2 Micro-scale Modeling

To estimate the ideal properties of the granular jammed system, a joint segment of a snake-like robot, a numerical model was used to calculate its stiffness. The joint is modeled as a cylinder 15 mm in diameter and 40 mm in length filled with granules at a maximum packing ratio. The granules are also assumed to be perfect, elastic spheres, 4 mm in diameter.

The joint segment was subjugated to three types of tests: bending, tension, and compression. In bending, the joint is fixed at one end and loaded at the tip. In tension, both ends are fixed and the joint undergoes 20% of engineering strain. Similarly, the compression

test consists of compressing the joint by 20% strain.

3.2.1 Volume fraction

The following approximations are based on the assumption that the granules are elastic spheres. The packing factor for granules is affected by three main aspects: granule diameter, interparticle friction, and the relative material density of the granule to the surrounding fluid [44]. The latter aspect is described in greater detail by [45]. The pressure level of the fluid affects the stiffness of the joint; a fluid at low pressure–the fluid is evacuated from the joint–increases the granular packing factor. In general, the packing factor ϕ is defined as follows:

Affected by both size and shape, the volume fraction is an important factor to maximize, with the granular system achieving better stiffness ranges at higher packing rates. The volume fraction ϕ can be found with the following equation:

$$\phi = \frac{V_{granules}}{V_{total}} \tag{3.1}$$

V_{total} is the volume of the cylindrical membrane, which is 3141.59 mm^3. The volume fraction for the 8 mm diameter, round beads is ϕ_{8mm} = 0.682. Comparatively, for the 4 mm round beads ϕ_{4mm} = 0.864, and 4 mm cube beads $\phi_{4mmcube}$ = 0.703. Despite being a good indicator of granular performance, however, there are other contributing factors for picking an ideal granule type, since a high ϕ value does not correspond to a low variance or hysteresis.

To estimate the joint's unjammed stiffness, the minimum packing factor ϕ_{RLP} is guessed. Known as the random loose packing factor, ϕ_{RLP} is discussed by [44] and is defined as the minimum packing factor for granules in a static state. However, we take ϕ_{RLP} to represent the packing factor for a given joint setup in its "soft" state, where are granules

are in a minimum state static equilibrium.

Though the absolute value of ϕ_{RLP} is different depending on granule properties and interparticle forces, a higher ϕ_{RLP} corresponds to a softer state. For example, spherical bead granules with no friction or cohesive forces to other granules would exhibit a ϕ_{RLP} = 0.64 value, whereas the same granules with high friction between grains can be as low as ϕ_{RLP} = 0.55.

3.2.2 Numerical model of particle interactions

3.2.2.1 Bending

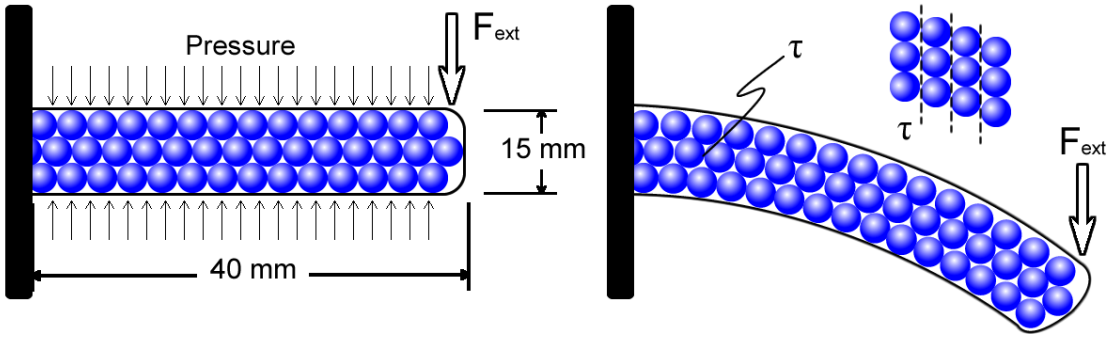

Figure 3.1: Diagram of the joint segment. The left diagram is the joint in its normal state, and the right diagram is it in its deflected state. Here, the deflected state is estimated as a series of shear flows across vertical layers of granules, with τ representing the shear stress at each layer.

To estimate the joint's jammed stiffness, other considerations must be made. The force required to bend the joint is first estimated from the shear stress τ acting on the joint, which can be found in terms of the solid fraction f, hydrodynamic viscosity η_H, shear rate $\dot{\gamma}$, interparticle static friction μ_s, and particle pressure P^s [46, 47]. The relationship for air τ_d and liquid τ_l systems are the following:

$$\begin{aligned} \tau_d &= (1 - f_d)\eta_H \dot{\gamma} + f_d \mu_s P^s \\ \tau_l &= (1 - f_l)\eta_H \dot{\gamma} + f_l \mu_s P^s \end{aligned} \tag{3.2}$$

where f is the equilibrium solid fraction $f = N_c/N$. N_c represents the number of granules in transient solid clusters per unit volume, and N is the total number of grains per unit volume. Note that a fully jammed state does not necessarily mean $f = 1$. However, if the shear rate shown in Fig. 3.1 is quasistatic, $\dot{\gamma} = 0$. Because the granules are randomly packed, f_d for dry granules should be estimated as:

$$\begin{aligned} f_d &\approx \tfrac{1}{1+\frac{I}{\mu_k}} \\ I &= \tfrac{\dot{\gamma} d}{\sqrt{P^s/\rho_p}} \end{aligned} \tag{3.3}$$

where μ_k is interparticle kinetic friction, I is the inertial number for dry granules, d is the diameter of each granule, and ρ_p is the density of each granule.

For granules in liquids, f_l is estimated by the following:

$$f_l = \frac{N_c}{N} \approx \frac{1}{1 + \frac{\eta_H \dot{\gamma}}{P^s \mu_k}} \tag{3.4}$$

From [46, 48], particle pressure P^s is defined as the "mean normal stress exerted by the particles," and is

$$P^s = (1/3)\sigma \tag{3.5}$$

where σ is the pressure differential on the joint (e.g. in the case of full vacuum, σ = 101 kPa or 14.6 PSI-A).

Finally, the conversion from shear stresses in Eq. 3.2 to the external bending force F_{ext} is as follows:

$$F_{ext} = \tau A \tag{3.6}$$

where A is the cross-sectional area of the joint.

The values used to calculate the load force at the joint tip is outlined in table 3.1. For the pneumatic system, the internal joint pressure level is set to 18 kPa (2.6 PSI-A) to reflect the pressure used in the experiments. Thus, σ was set to 83 kPa (12 PSI-A), resulting in a loading force of 0.43 N. For the hydraulic system, σ is estimated to occur at full water evacuation, and thusly set to 101 kPa (14.6 PSI-A). This results in a force of 0.53 N, higher than its pneumatic counterpart.

Table 3.1: Bending simulation results - dry 4 mm diameter spherical granules

	Full Vacuum	**90% Vacuum**	**Half Vacuum**	**Atmosphere**
F_{ext} (N)	**5.35**	**4.82**	**2.67**	**0.00**
τ (kPa)	30.30	27.28	15.15	0.00
σ (kPa)	101	91	50.5	0.00
A (mm^2)	176.7	176.7	176.7	176.7
η_H (kPa-s)	1	1	1	1
$\dot{\gamma}$ (mm/s)	1	1	1	1
μ_k	0.4	0.4	0.4	0.4
μ_s	0.9	0.9	0.9	0.9
P^s (kPa)	33.7	30.3	16.83	0.00
d (mm)	4	4	4	4
ρ_p (kg/m^3)	2500	2500	2500	2500

3.2.2.2 Tension

Given the cohesion-less properties of the granules, the tensile force should be directly dependent on the stiffness of the membrane material. Thus, the tensile experimental results in Section 5.3.3 are expected to match the membrane tensile analysis in Section 5.3.1 for all pressure levels.

Table 3.2: Bending simulation results - wet vs dry 1 mm diameter spherical granules

	Hydraulic	**Pneumatic**
F_{ext} (N)	**0.53**	**0.43**
τ (kPa)	6.73	5.53
σ (kPa)	101	83
A (mm^2)	78.5	78.5
η_H (kPa-s)	1	1
$\dot{\gamma}$ (mm/s)	1	1
μ_k	0.2	0.2
μ_s	0.2	0.2
P^s (kPa)	33.7	27.7
d (mm)		1
ρ_p (kg/m^3)		1180

3.2.2.3 Compression

The compression tests are similar to triaxial shear tests, and thus a stress-dilatancy relation is used. From [49], the loading stress can be written as F_{ext}/A, giving rise to the static equation

$$\frac{F_{ext}}{A} = \tan(\alpha)\tan(\phi_u + \beta)\sigma \tag{3.7}$$

where α is a geometrical property of the packing such that $\alpha = \arctan(l_p/d)$. β is the angle between granule centers. Thus, for a perfect packing, $\alpha = \beta = 60°$. ϕ_u is the friction angle, also known as the angle of repose. For glass spheres, this is $\phi_u = 17°$. Substituting in the values, an ideal system would withstand a stress F_{ext}/A of 0.68 MPa before deflecting.

3.3 Macro-scale Modeling

This section examines the granular jamming mechanism as a whole. Thus, rather than modeling granule interactions, this section models the joint segment as one object.

3.3.1 Cantilever beam

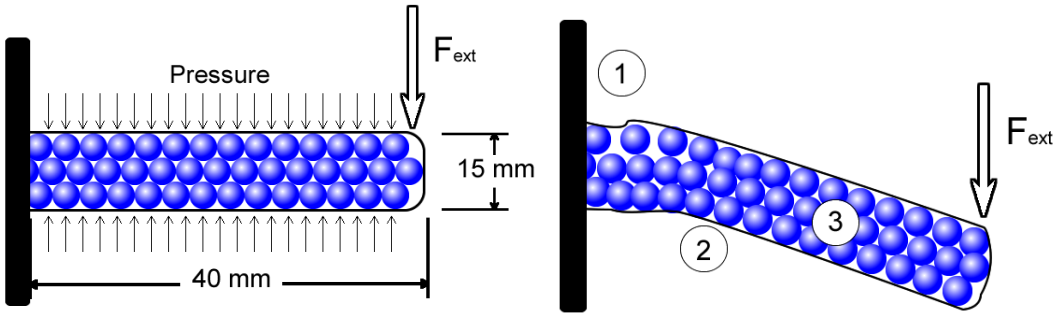

Figure 3.2: Diagram of the joint segment as a cantilever. The left diagram is the system in its normal state, and the right diagram is it in its deflected state. Region 1 undergoes tension and granules lose contact with each other, whereas region 2 experiences compression. Region 3 is where particles remain in their normal configuration.

To understand the behavior of granular jamming joint, it is modeled as a one end fixed cantilever beam undergoing a force at the tip, as seen in Fig. 3.2. The purpose of these simulations is to study the effect of Young's modulus E in the context of granular jamming. The total bending moment M is the following:

$$| M |=| L || F_{ext} | \tag{3.8}$$

where M is the total moment, L is the length of the beam, and F_{ext} is the externally applied force. For our experiments, L was 40 mm, and will be likewise used for our simulations. The moment of at single point along the beam is characterized by the following:

$$M = F_{ext}(L - d) \tag{3.9}$$

where d is the distance from the fixed end. From Eq. 3.9, the change in moment decreases linearly as d approaches the tip. Thus, with the fixed end undergoing the largest moment, the jammed system will bend the most at the base, as seen in Fig. 5.1.

The beam bending behavior can be written as a fixed-ended solid cylinder undergoing a point load at the free tip, and it is written as follows:

$$y(d) = \frac{F_{ext}d^2(3L - d)}{6EI} \tag{3.10}$$

where w and t are the width and thickness of the beam, and $y(d)$ is the perpendicular displacement of the beam along distance d. Fig. 3.3 shows the calculated beam bending shape and corresponding E value from Eq. 3.10, where the tip deflection distance $y(L)$ is kept constant at 10 mm and F_{ext} is from experimental data.

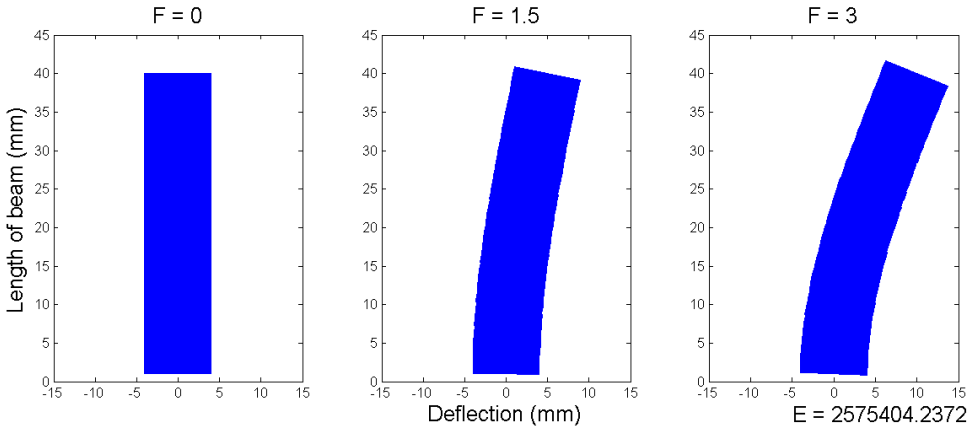

Figure 3.3: Calculated beam bending to find the equivalent Young's modulus E, given a tip force F_{ext} and tip displacement $y(L)$.

The maximum deflection, which occurs at the tip $y(d)$ where $d = L$, can be simplified from Eq. 3.10 to

$$y(L) = \frac{F_{ext}L^3}{3EI} \tag{3.11}$$

The area moment of intertia I is given as:

$$I = \frac{\pi r^4}{4} \tag{3.12}$$

with r as the radius of the joint.

Thus, from the experimental bending results, and rearranging Eq. 3.11, E can be calculated as:

$$E = \frac{4}{3}\frac{F_{ext}L^3}{\pi r^4(y(L))} \tag{3.13}$$

From Eq. 3.13, the Young's modulus of the joint can be approximated, assuming the joint is an elastic material. Although the joint can behave in a nonlinear fashion, as well as exhibit inelastic behavior, the approximation with E serves as a sufficient quantitative measure to compare stiffnesses of different granular jamming systems.

3.4 Discussion

In Section 3.2.1, an investigation on the volume fraction and packing factors is made. Given the geometry of the membrane's cylindrical shape and the shapes and sizes of the granules, the volume fraction can be estimated. Because the rigidity of the joint is dependent on the jammed, or "solid," state of the granules, the assumption is made that higher volume fractions, or more densely packed granules, will result in higher rigidity. Similarly, the lower the random loose packing, the less rigid. Though the absolute stiffness is not derived from these equations, the volume fraction and random loose packing ratio

models can be a quick measure to rank different granule types for their stiffness range. This can be used to for a first-pass design criterion for granule size and shape.

To investigate further the stiffness range of granular jamming, Sections 3.2.2.1, 3.2.2.2, 3.2.2.3 estimate achievable stiffness of the joint in bending, tension, and compression, respectively. Due to the complexity of modeling particle contacts given random packing configurations and shapes, the numerical models used assume perfectly elastic spherical granules. Nonetheless, the equations give an estimate value for the joint in different jammed states. When compared to experimental data in Chapter 4, these models overestimate the stiffness. The modeled stiffness are within the same order of magnitude as the experimental results, but with the research in this area in its early stages, further improvements on the model have not been developed. Another method used to estimate the particle interactions, such as jamming, has been to use the discrete element method (DEM). It is a computer model used to track each particle's location and contacts in small, discrete time segments. Though a popular tool, the parameters for DEM primarily depend on experimental data, and the DEM outputs remain to be approximations.

However, the model used in Section 3.2.2.1 provides a estimating in comparing dry and wet granules. The model shows that the jammed behavior between dry and wet granules are similar, and the same relation is found in the experimental results in Chapter 6.

In Section 3.3.1, the joint is modeled as a cantilever to estimate the stiffness. Though the joint can behave nonlinearly, the cantilever model is a useful tool to quantify the stiffness of the granular jamming system. By encompassing the stiffness of the granule jamming system into E, results between different joint setups can be compared. Systems with different types of granules, for example, can be approximated as cylindrical beams of different types of solid material. Thus, the resulting Young's modulus E quantifies its properties on a macro-scale.

Chapter 4

The Effects of Granules in Granular Jamming

Abstract

The stiffness range and profile of granular jamming mechanism is dependent on the properties of the granules. The size, shape, and material properties of the granules can vary the stiffness range, hysteresis, and variability of the device. A comprehensive list of experiments were performed to characterize the behavior of the mechanism's stiffness properties with different types of granules. It was found that small, cube-shaped granules with a high friction coefficient had many of the most desirable properties. In a more general sense, results show that the size and shape of the granules impact the jamming performance, stiffness of the individual particles dictate the stiffness of the macro system, and an increase in surface friction can increase stiffness and improve hysteresis. The experiments also show that the coupling of granules, such as tying them along a string, can also significantly improve the stiffness.

4.1 Introduction

Current groups investigating granular jamming for robotic applications have experimentally tested a variety of granule types to optimize their robotic system. Groups in the field have typically settled either on ground coffee [29, 30, 50] or spherical granules [31, 33, 22], with more recent research favoring the former. Nonetheless, this chapter is a comprehensive look at the driving factors in granular jamming by quantifying the effects of granule shape, size, and material properties. The last section of this chapter quantifies the following characteristics of ground coffee: stiffness range, variability, and hysteresis. Though ground coffee is a favored granular media, the analysis of other granule types will enable engineers to design a synthetic version that exhibits similar characteristics to ground coffee, without the drawbacks that coffee may have as an organic material. Not only is it unsuitable for sterilization in an autoclave, which requires it to be steamed at 121 degrees Celsius for 15 minutes, it is also at risk of characteristic changes that may occur from decomposition. Additionally, because granular jamming uses a vacuum to create the pressure differential, granules that outgas are highly undesirable. According to [51], ground coffee under vacuum can eventually re-inflate the membrane via outgassing, affecting the variability and stiffness range.

4.2 Methods

For the flexible endoscope, a joint segment was analyzed to better understand the effects of the membrane during granular jamming. The joint was a cylinder 15 mm in diameter and 40 mm in length, filled with granules. The average packing factor ϕ for each test was 0.61 +/- 0.01.

In our set-up, joint segment is a column that has a outer diameter of 15 mm and length of

40 mm with a 0.15 mm thickness. Several homogeneous granular materials were tested for this application, with separate experiments for granules in varying shape, size, and material. A volume of 5600 mm^3 of granular material was used for each type, as it was just enough to provide some rigidity to the column when under atmospheric pressure. The experiments were performed by fixing the base of the joint and deflecting the tip with a force sensor by 10 mm. The deflection rate was 1 mm/sec. Fig. 4.1 shows the experimental setup, where the joint segment is deflected horizontally via a linear rail. 5-10 trials were performed for each granule type at each pressure level.

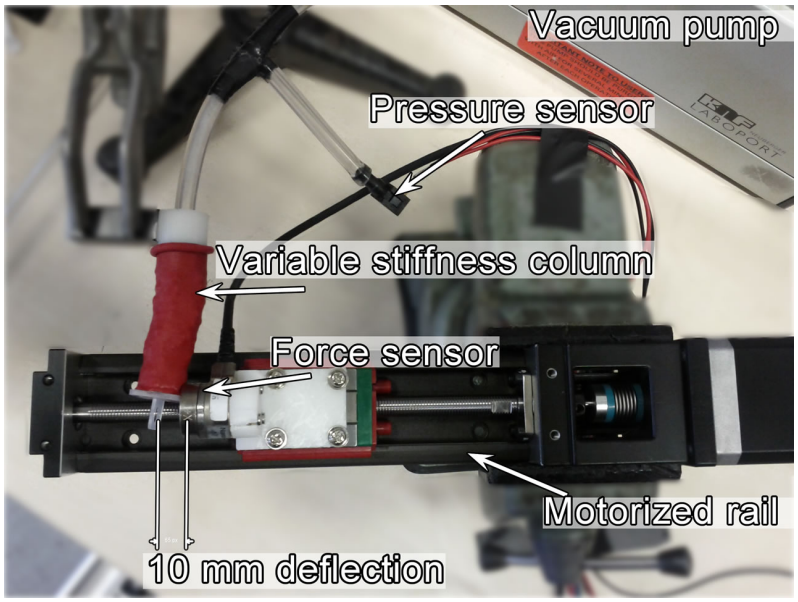

Figure 4.1: Experimental setup under atmospheric pressure with 10 mm deflection

The joint segment's internal pressure is pumped to multiple levels of vacuum. With 101, 70, 35, and 10 kPa translating to 0%, 30%, 60%, and 90% vacuum. Full vacuum was not used, due to the limitation of the pump.

4.3 Granule Shape

Figure 4.2: The four granule types tested. From left: Smooth spherical, matte spherical, smooth faceted, and matte cube.

The rigidity and softness of a granular jamming system is dependent on the granule properties. Thus, the first variable to consider is the granule shape. How does the geometrical properties of the granules affect the stiffness range?

The four shapes of granular materials picked were beads of different construction: smooth spherical, smooth faceted, matte spherical, and matte cubes. The terms smooth and matte describe the surface characteristic of the granules. These four were chosen based on commercial availability and price.

The experiments consisted of deflecting each column 10 mm with 1 mm step increments forwards and backwards. The force was recorded for each distance to calculate the stiffness of the column. This test was done for atmospheric (101 kPa), 70 kPa, 35 kPa internal vacuum pressures on the absolute pressure scale.

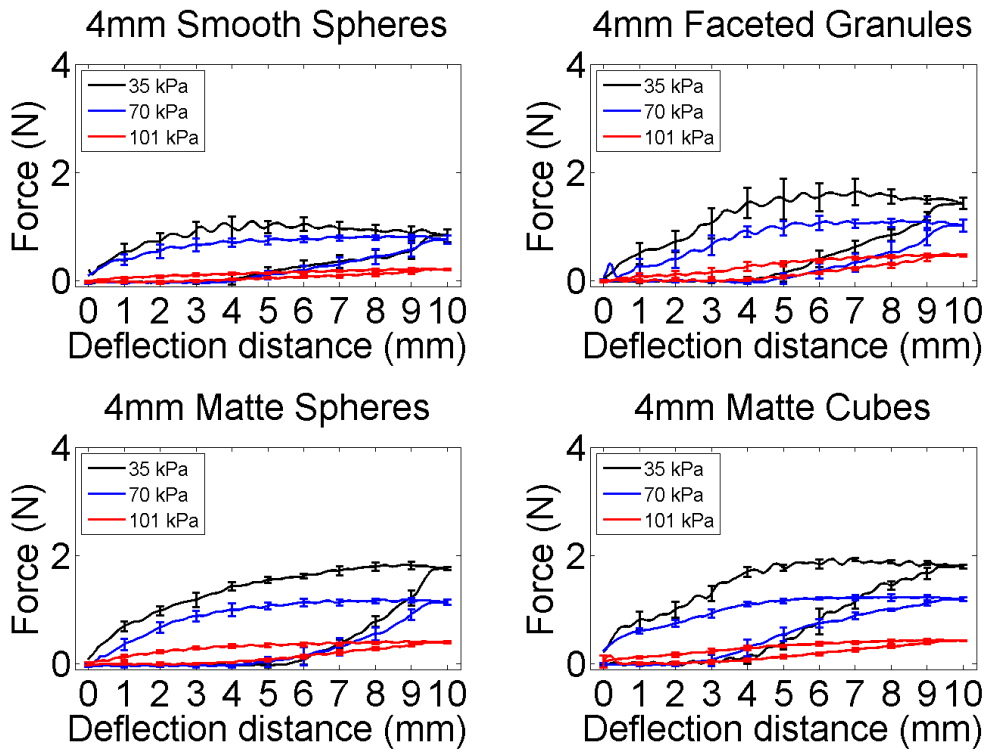

Figure 4.3: Comparison of the 4 types of granules tested at absolute pressures 35 kPa (black), 70 kPa (blue), and 105 kPa (red). The granules are smooth spheres, faceted granules, matte spheres, and matte cubes.

Fig. 4.3 show the comparisons between the four types of granules tested. Each test shows that the granules approach and saturate at a maximum force. Our tests show that the matte cube granules worked best, as they exhibited the most friction between each other. Additionally, the cube beads exhibited the widest range of stiffness, with a difference of 1.5 N between the highest and lowest vacuumed states. Conversely, the smooth sphere granules performed the worst, as the spherical shape of the granules and smooth surface limited its ability to maintain a jammed state. For the cube granules, the high contact area and efficient packing shape made it ideal for jamming. However, it should be noted that the cube beads exhibited less stiffness when the granules were not arranged in parallel. In other words, when the cubes were mixed in diagonal and parallel orientations, the

stiffness of the column dropped. This increases the amount of variance the cube granules have.

From Fig. 4.3, there is a clear sign of hysteresis. It should be noted that during the return phase, a 0 value in force denotes a loss of contact between the element and the force sensor. When this occurs, the tested element would not return to its original position. Thus, the variable stiffness element undergoes "permanent" deformation, with some elastic deformation, as well. In the case of granular jamming, this so-called "permanent" deformation remains so as long as the granule states remain the same. If the state changes, such as if joint is unjammed, it can be reset to an undeformed position. The variability is a measure of the joint's behavior between trials, where the joint undergoes "permanent" deformations and resets.

Table 4.1 summarizes the properties of the four granules shapes shown in Fig. 4.2 and 4.3.

Table 4.1: Summary of granule shape experimental results

Granule Type	**Pressure (kPa)**	**Force (N)**	**Hysteresis**	**Variability (N)**	**E (MPa)**
Smooth Spheres	101	0.22	0.57	0.02	0.19
	70	0.83	0.71	0.09	0.71
	35	1.10	0.75	0.13	0.94
Faceted Granules	101	0.51	0.49	0.04	0.44
	70	1.11	0.70	0.12	0.95
	35	1.65	0.68	0.14	1.41
Matte Spheres	101	0.42	0.58	0.03	0.36
	70	1.19	0.74	0.09	1.02
	35	1.83	0.76	0.09	1.57
Matte Cubes	101	0.44	0.44	0.04	0.38
	70	1.23	0.49	0.07	1.06
	35	1.94	0.56	0.10	1.67

4.4 Granule Size

4.4.1 Size: Spheres

Figure 4.4: 8, 6, and 4 mm diameter plastic spheres.

As seen in the bending model in Section 3.2.2.1, friction is a driving factor in the achievable stiffnesses of a jammed system. Thus, it is possible for the size of the granules to also impact the stiffness, as the smaller the granule, the larger the surface area to volume ratio there is. An increase in surface area could increase the friction between granules. However, this section only investigates marco-level particle sizes. In other words, granules are of a size so that tens to hundreds are within the membrane, rather than thousands or millions. The size experiments also ignore other factors which may come into play for small particles, such as electrostatic forces.

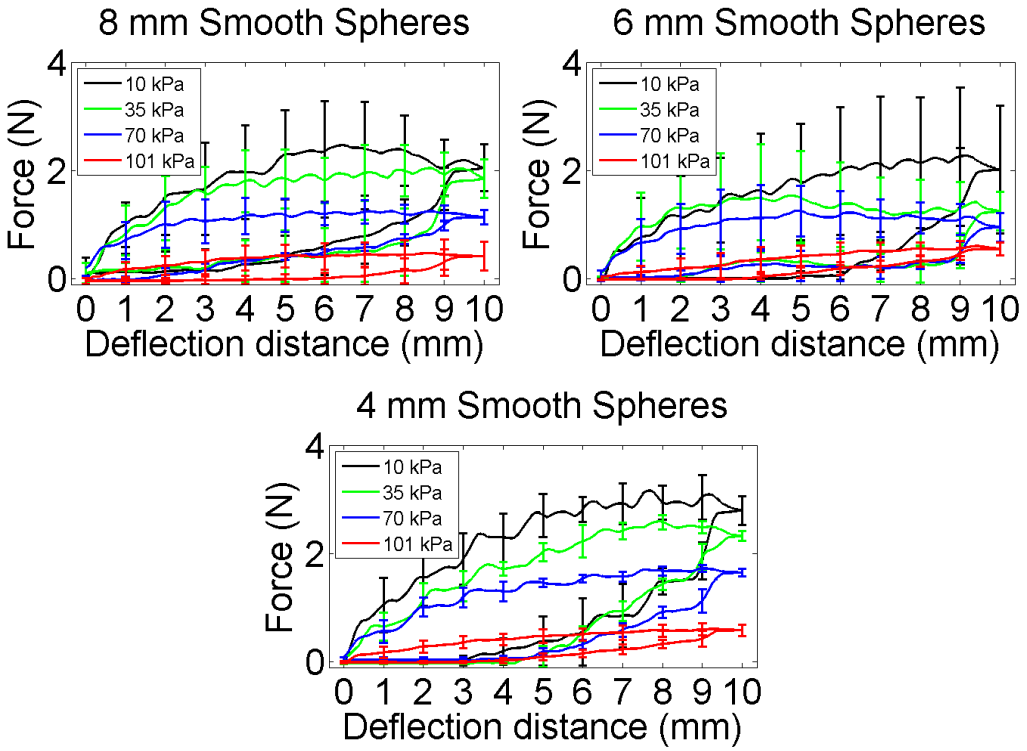

Figure 4.5: Here, 8, 6, and 4 mm diameter commercially available, round, plastic beads are tested. Because of the fixed size of the membrane, the 4 mm beads were found to have the highest stiffness and least variability.

Fig. 4.5 shows that smaller granules do perform better, with higher stiffnesses. However, there is a cost in hysteresis and variability. This is possibly due to the higher variability in the random packing of the granules, as the constant volume of the joint column limits the 8 mm diameter granules to fewer packing configurations than the 4 mm diameter granules.

4.4.2 Size: Cubes

Figure 4.6: 4, 2, and 1.5 mm plastic cubes.

As shown in Section 4.3, the geometry of the individual granules is significant as well. Thus, the significance of size was also examined for cubes. The shape of cube granules yielded results with much less variability than the sphere beads.

The 2 mm granules have a higher peak force than the larger 4 mm and smaller 1.5 mm granules, as shown in Fig. 4.7. This suggests that there is a optimal size for a given volume. It should be noted that the 2 mm size could be a local optimum, and that smaller granules could still exhibit higher stiffnesses.

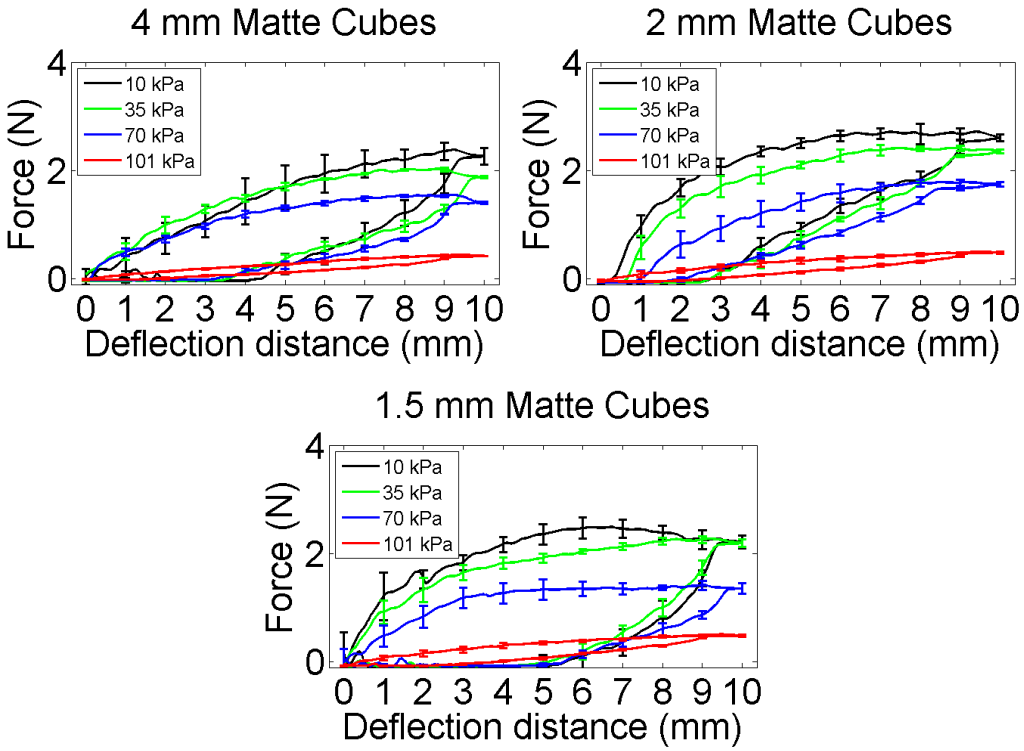

Figure 4.7: Tests on plastic cube beads show that 2 mm granules have a higher stiffness than larger 4 mm and smaller 1.5 mm granules.

Figs. 4.5 and 4.7 also show that the stiffness of the joint at the 101 kPa level, the unjammed state, increases as the bead size decreases. This suggests that there is a stiffness range which can be offset by granule size.

Table 4.2: Summary of granule size experimental results

Granule Type	Pressure (kPa)	Force (N)	Hysteresis	Variability (N)	E (MPa)
8 mm Spheres	101	0.48	0.57	0.83	0.41
	70	1.25	0.60	0.09	1.07
	35	2.04	0.67	0.13	1.75
	10	2.47	0.67	0.13	2.12
6 mm Spheres	101	0.61	0.57	0.11	0.52
	70	1.26	0.75	0.28	1.08
	35	1.54	0.77	0.44	1.32
	10	2.27	0.76	0.57	1.95
4 mm Spheres	101	0.61	0.63	0.08	0.52
	70	1.73	0.68	0.11	1.49
	35	2.59	0.67	0.14	2.22
	10	3.16	0.70	0.31	2.71
4 mm Cubes	101	0.45	0.44	0.01	0.39
	70	1.55	0.66	0.08	1.33
	35	2.03	0.67	0.06	1.74
	10	2.38	0.62	0.20	2.04
2 mm Cubes	101	0.50	0.49	0.03	0.43
	70	1.79	0.40	0.08	1.54
	35	2.42	0.52	0.08	2.08
	10	2.72	0.54	0.10	2.34
1.5 mm Cubes	101	0.51	0.60	0.02	0.44
	70	1.42	0.79	0.10	1.22
	35	2.27	0.75	0.11	1.95
	10	2.49	0.83	0.19	2.14

4.5 Granule Material

4.5.1 Solid rubber granules

Figure 4.8: 4 mm solid rubber granules.

Based on the work in [42], deformable granules were tested to verify their simulations. They postulated that deformable granules, with their overlapping stiffness, would improve the total tangential force between granules. [42] notes that this total tangential force is limited by the Coulomb frictional limit, as past this value the grains begin to slide across each other. For our tests, we used polyurethane rubber with a hardness of Shore 70A. However, Fig. 4.9 shows that despite the added traction between individual granules to adjacent neighbors, the deformability of the granules themselves decreased the upper bound of the stiffness range.

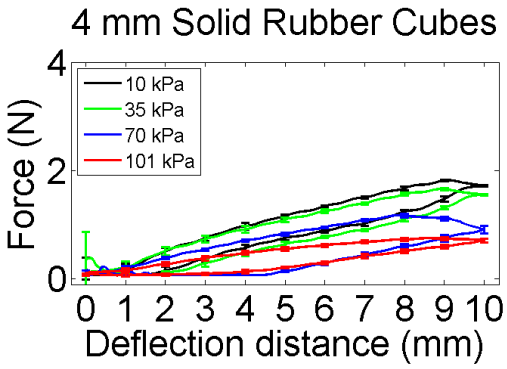

Figure 4.9: Tests on solid rubber cube beads show that while the variability is low at 0.05, the peak force is also low at 1.8 N. However, unlike the solid, plastic beads, these granules exhibit a much more linear profile for both pushing and returning.

The results in Fig. 4.9 show that rubber granules are less stiff than plastic or glass granules, with the stiffness of these granules at 10 kPa on par with matte plastic cubes at 35 kPa. However, the hysteresis and variability are significantly improved. This suggests that the interaction between rubber granules decreases both hysteresis and variability over plastic and glass materials.

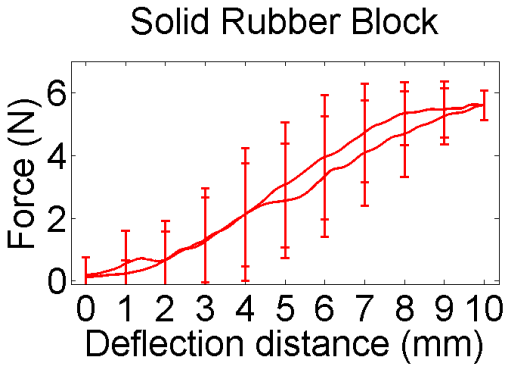

Figure 4.10: Results on a single rubber block. Note this plot is set to a different scale. Hysteresis = 0.11, variance = 1.17 N, E = 2.84 MPa

For comparison, a solid block (10x10x40 mm) of the same polyurethane rubber was

measured and had a peak force of 5.47 N. This shows that, even at its 10 kPa jammed state, the rubber granules behave as a softer material. Of course, the solid rubber block does not have the advantage of varying its stiffness.

4.5.2 Hollow rubber granules

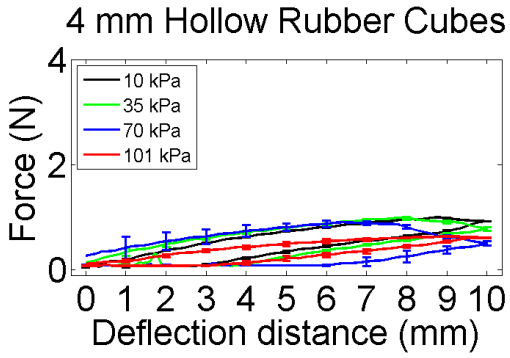

Figure 4.11: The hollow rubber cubes had similar profiles, despite varying the pressure. There was only a 0.35 N improvement from atmospheric pressure to near vacuum.

To investigate the behavior of granules with a spring coefficient and negligible damping, hollow rubber grains were made and tested, as seen in Fig. 4.11. The same polyurethane rubber was used. Plastic molds were printed with a rapid prototyping machine, and sheets of half of the hollow cubes were pressed together to create airtight, hollow rubber granules that held an internal pressure at an atmospheric 101 kPa (15 PSI).

The results in Fig. 4.11 show that hollow rubber cubes provide little benefit over solid rubber cube granules. Not only were the stiffnesses lower, but there was no improvement in hysteresis or variability.

Comparing these results to those in Fig. 4.9, the data suggests that damping is not a significant player in granular jamming, as the hysteresis and variability are similar. Also, the lower spring constant of the hollow rubber granules resulted in significantly lower

stiffnesses when jammed. Thus suggests that granules with higher spring constants also provide the jammed joint with a higher stiffness.

4.5.3 Composite granules

Figure 4.12: 4 mm rubber/plastic composite cubes.

Fig. 4.12 shows the composite granules, which are made of solid plastic granules individually covered in a 0.5 mm layer of the polyurethane rubber. From the solid and hollow rubber granule tests, hysteresis is significantly improved over solid materials, but at a cost of stiffness. Hence, a composite of solid and soft materials may give rise to a granule with the benefits of both material types.

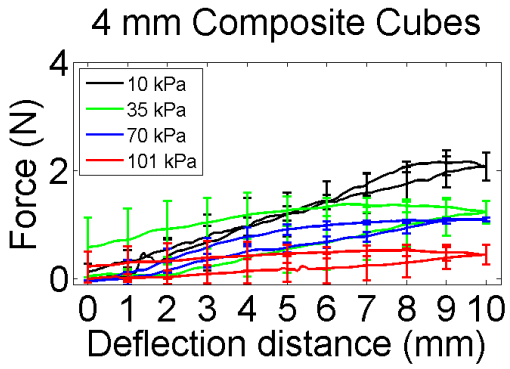

Figure 4.13: Results for a composite, cube granule type, where the center of each particle is solid plastic surrounded by a layer of rubber. The force only peaked at 2.16 N, but had a very low level of hysteresis.

The results in Fig. 4.13 show that the composite cubes improved the force range over purely rubber granules, and improved both the hysteresis and variability over purely plastic granules. Most interestingly, at 10 kPa, the composite granules displayed the lowest amount of hysteresis among all the granule types tested.

Table 4.3: Summary of granule material experimental results

Granule Type	**Pressure (kPa)**	**Force (N)**	**Hysteresis**	**Variability (N)**	**E (MPa)**
Solid Rubber Cubes	101	0.75	0.44	0.03	0.64
	70	1.17	0.59	0.03	1.00
	35	1.66	0.35	0.05	1.43
	10	1.82	0.31	0.05	1.56
Hollow Rubber Cubes	101	0.64	0.43	0.03	0.55
	70	0.90	0.76	0.07	0.77
	35	0.99	0.56	0.03	0.85
	10	1.00	0.44	0.02	0.86
Composite Cubes	101	0.53	0.34	0.20	0.45
	70	1.11	0.24	0.09	0.95
	35	1.38	0.54	0.35	1.18
	10	2.16	0.11	0.24	1.85

4.6 Coupled Granules

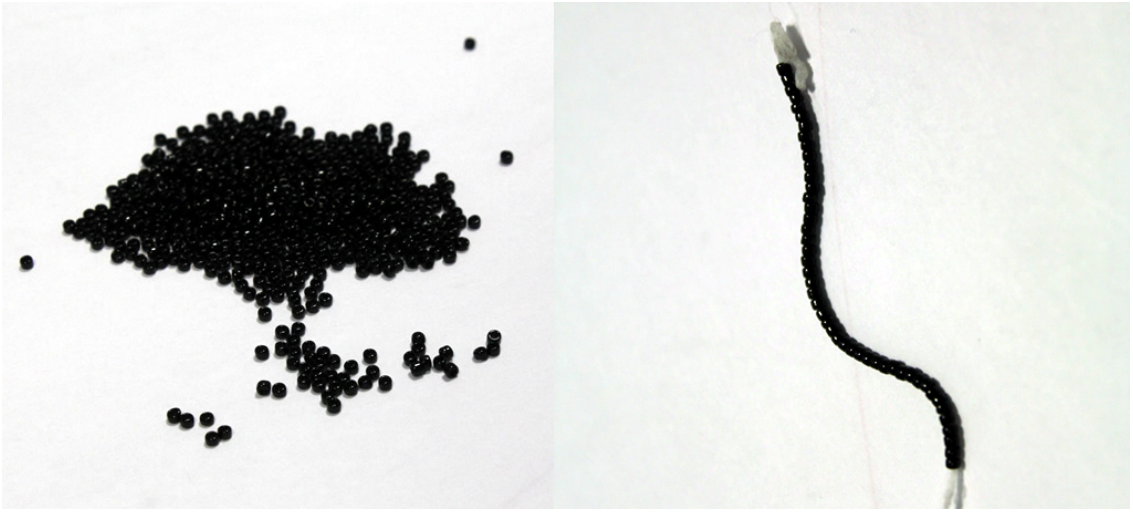

Figure 4.14: A comparison to decoupled (left) and coupled granules (right).

To vary their body stiffness, invertebrates have a hydrostatic skeleton which consists of fluid-filled cavities that resist muscle contraction. These counteracting forces stiffen the body or limb [52]. Granular jamming operates similarly by applying an external stress on loose particles [53]. Inspired by the biological stiffening mechanism, granules were coupled together to simulate the connective tissue fibers within muscles which help increase the stiffness [54]. The coupled granules were made with particles linked together by a flexible strand.

Note that the granules in this test are 1.5 mm diameter spheres, and the ends of the flexible strand were not tied to the membrane.

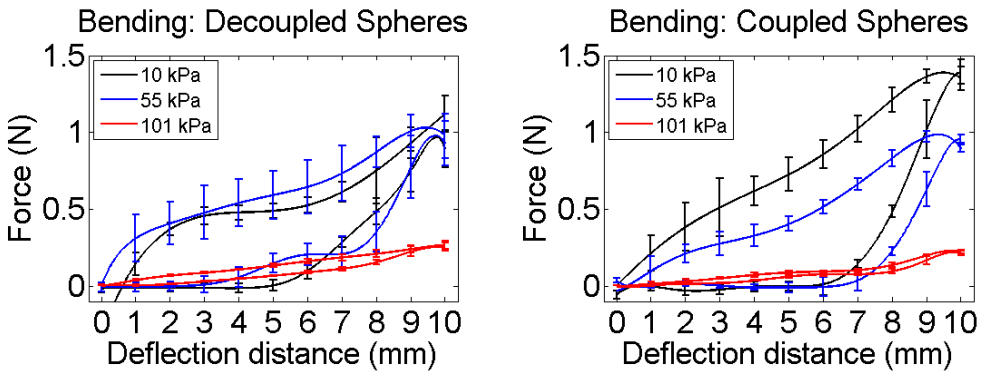

Figure 4.15: Results of bending decoupled and coupled granules at atmospheric, 50%, and 90% vacuum.

Fig. 4.15 shows a comparison between the coupled and decoupled spheres. The coupled granules are have a 50% improvement in stiffness.

Because there is now a strong cohesive force, the flexible strand, between the granules, a tensile test was also performed to examine the effects of jamming when the joint is pulled.

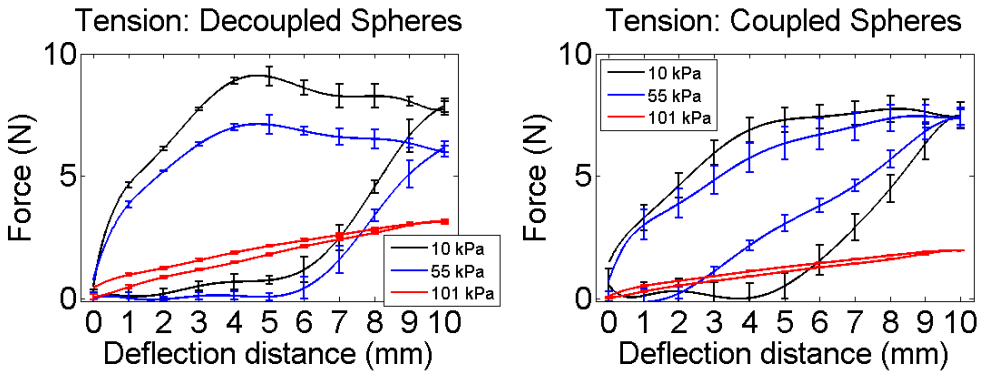

Figure 4.16: Results of tensioning decoupled and coupled granules at atmospheric, 50%, and 90% vacuum.

4.7 Ground Coffee

The properties of four different sizes of ground coffee were experimentally measured, as shown in Fig. 4.17. The average particle sizes are 4 mm, 2 mm, 1 mm, and fine (powder-like). These sizes reflect the largest measurable granule from each grinding. For each of the tests, about 1 gram of coffee was used to fill the joint.

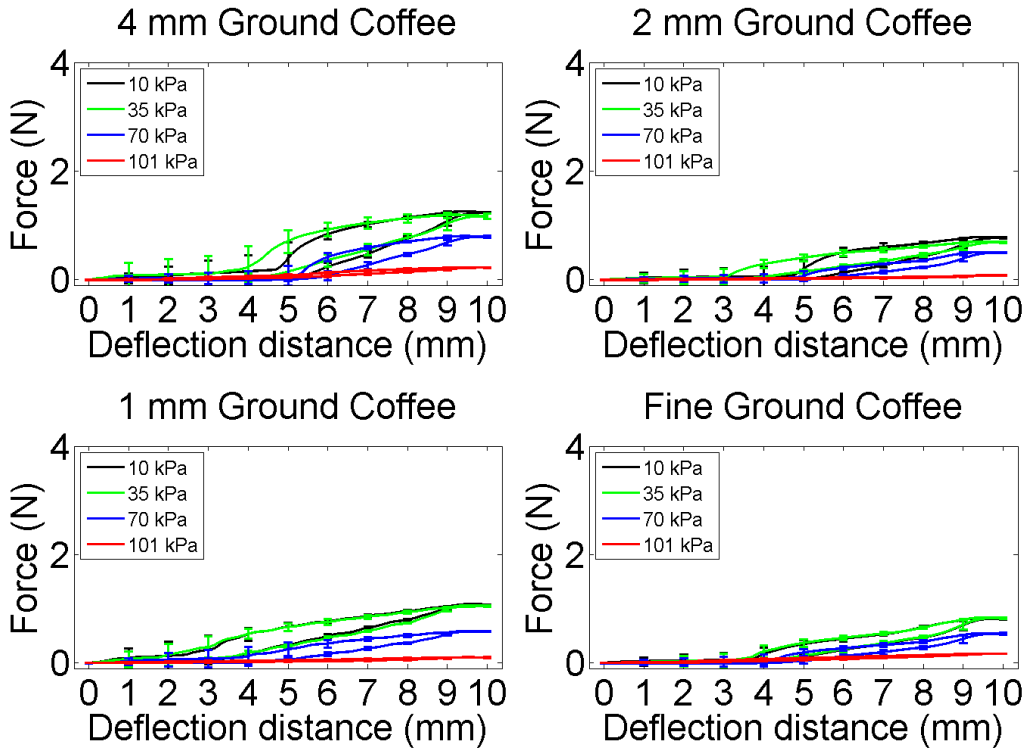

Figure 4.17: Four different sizes of ground coffee particles were tested: 4 mm, 2 mm, 1 mm, and fine (powder-like).

From Fig. 4.17 and Table 4.4, it can be seen that coffee granule size affects the stiffness of the joint. From these results, the 1 mm size is a local maximum, whereas the 4 mm is the global maximum. This is consistent with the results found from the size experiments in Section 4.4, where smaller sizes is not necessarily better in terms of achievable stiffness. Likewise, smaller sizes improve the hysteresis and variability of the joint.

Table 4.4: Summary of coffee granule material experimental results

Granule Type	Pressure (kPa)	Force (N)	Hysteresis	Variability (N)	E (MPa)
4 mm Coffee	101	0.22	0.32	0.01	0.19
	70	0.80	0.38	0.04	0.69
	35	1.19	0.43	0.10	1.02
	10	1.25	0.43	0.07	1.07
2 mm Coffee	101	0.08	0.28	0.01	0.07
	70	0.51	0.39	0.02	0.43
	35	0.70	0.37	0.04	0.60
	10	0.78	0.44	0.05	0.67
1 mm Coffee	101	0.10	0.29	0.01	0.09
	70	0.59	0.38	0.04	0.51
	35	1.06	0.34	0.05	0.91
	10	1.08	0.31	0.05	0.93
Fine Coffee	101	0.17	0.24	0.01	0.15
	70	0.55	0.36	0.03	0.47
	35	0.84	0.32	0.04	0.72
	10	0.83	0.33	0.04	0.71

4.8 Discussion

From Tables 4.1 to 4.4, we find that at atmospheric pressure, the peak forces are similar for all granule types. The medium sized granules, chiefly the 2-4 mm sizes, achieved higher peak forces under vacuum than granules of a larger or smaller size. This indicates that there could be an optimum size for granules. However, the 2-4 mm size may only be a local optimum, since very small grains may experience other significant factors such as cohesion from electrostatic forces or intermolecular bonding. Studies of these effects are outside the scope of this thesis.

The force-deflection profile of many of the tests display a plateau effect, where the measured force no longer increases as the system is further deflected, most notably seen in Fig. 4.5 and 4.7. This is possibly a result of granules shifting and losing contact, known

as dislocations, with adjacent particles, particularly in the tensioned side of the system, as demonstrated in Fig. 3.2. At that point, the main resisting force could be the membrane itself, which has a maximum value.

While the rubber granules in Fig. 4.9 and 4.11 proved to be insufficiently stiff, the linearity and low hysteresis of their profiles could be attributed to the decreased probability of shear between individual granules. As shown in Fig. 4.13, a new, composite bead type did achieve better linearity, albeit little improvement for stiffness. Nonetheless, the linearity of the stiffness and lower hysteresis will simplify the control scheme for the manipulator.

There were several experimental limitations for these investigations. The granules tested in each category were not uniformly sized, with a measurement difference of about 5-10% between "identical" sets of granules. Also, the volume fraction differed between certain trials, as different packing configurations yielded more or fewer granules inside the membrane. This could have increased the size of some of the error bars, as well as the limited number of trials.

Many further improvements can be made to increase the overall stiffness, increase the linearity of the stiffness, and decrease the variance, possibly with interlocking granules or internal sub-membranes. The experiments suggest the following: volume fraction and granule stiffness affects the overall stiffness of the jammed matter and inter-particle traction affects the variability, hysteresis, and linearity of the stiffness. For the composite granules, the inter-particle traction prevents the granules from sliding between each other, as well as from sliding against the latex membrane.

Chapter 5

The Effects of Membranes in Granular Jamming

Abstract

Many studies have evaluated the effects of different granule types by experimentally varying the sizes, shapes, and material properties of the particles. However, the role of the membrane in determining the possible range of stiffness or the variability of granular jamming has not been well studied. This chapter investigates the effects and significance of membranes for a granular jamming system. Five hygienic membrane materials were experimentally tested and analyzed in order to find the amount of flexibility and stiffness they provide when the system is in an unjammed and jammed state, respectively. This chapter presents results which show that the membrane plays a significant role in granular jamming stiffness in that a stiffer membrane can result in a stiffer jammed state without significantly impacting the unjammed stiffness. Also coupling the membrane to the granules can reduce the hysteresis of deflecting the joint.

5.1 Introduction

This chapter aims to comprehensively examine several types of membrane materials suitable for a granular jamming-based medical robot. The sterilizable membranes should be soft and flexible to maintain good contact with the granules, as previous works show that such an interaction improves the hysteresis [55]. Their effects on the stiffness range, hysteresis, and variability will open a broader range of granular jamming analysis, aiding in the optimization of such systems using the technology. The membrane experimental results presented in this chapter will be the first for variable stiffness robotics, and will be an aid in designs of new devices such as a MIS tunable stiffness endoscope.

5.2 Methods

For the flexible endoscope, a joint segment was analyzed to better understand the effects of the membrane during granular jamming. The joint was a cylinder 15 mm in diameter and 40 mm in length, filled with 4 mm diameter glass spheres. The average packing factor ϕ for each test was 0.61 +/- 0.01. As the chapter is focused on the membranes, a reference material of glass was chosen for the granules. Glass was used for its hardness and frictional properties, as well as being a classic granule type in literature. The 4 mm diameter size was chosen based on the author's previous work, which showed that 4 mm is an ideal size for the given joint dimensions [56, 55].

To comprehensively record the behavior and effect of membranes in granular jamming, three types of tests were performed on the granular jammed joint: Bending, tensile, and compression tests. These tests are meant to categorize the behaviors of the joint from tasks the robot will perform. Because the granules and membranes are decoupled, the joint may behave as different equivalent materials for the three types of tasks it must

perform. For example, in turning or lifting, the behavior of the joint may have a different stiffness characteristic than for pulling or pushing. The bending tests correspond to these turning or lifting manipulation tasks, the tension tests correspond to pulling tasks, and the compression tests correspond to pushing tasks the joint and robot will perform.

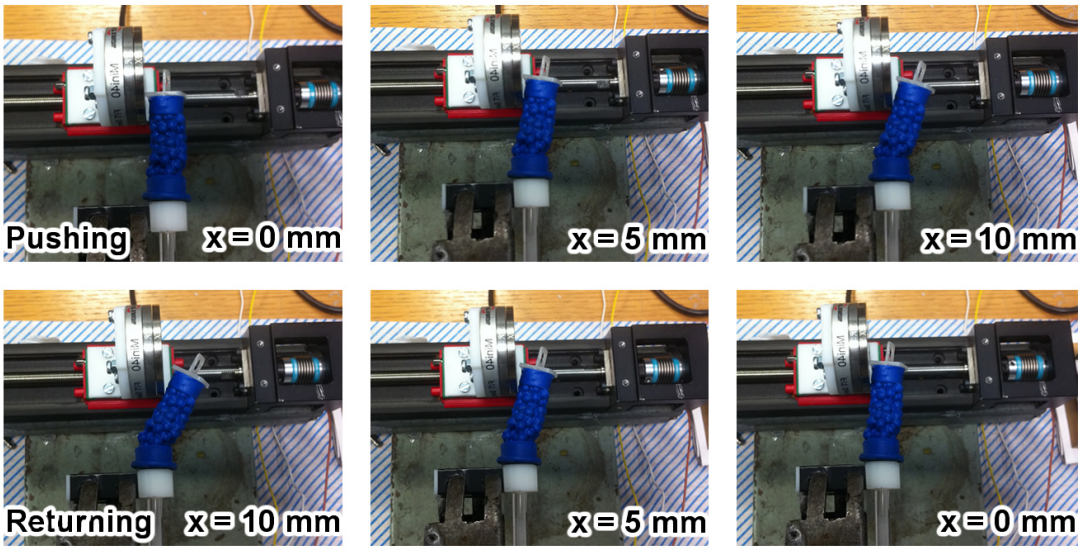

Figure 5.1: Screenshots of the bending experimental setup, showing the pushing and returning of a single joint.

The five different membranes tested were the following: latex, nitrile, vinyl, vitrile, and polythene. The former four materials were chosen based on their applications in the medical field, particularly surgical gloves. Latex is the most commonly used surgical membrane, with nitrile and vinyl commonly used as latex-free substitutes. Vitrile is a mixture of vinyl and nitrile, offering increased strength over pure vinyl and increased flexbility over pure nitrile. The polythene material was chosen from its applications in the food industry, such as vacuum packaged goods. Polythene is a low-density polyethylene, the most commonly used non-toxic plastic material.

The experiments were repeated at three different pressure levels: 101 kPa (15 PSI-A), 55

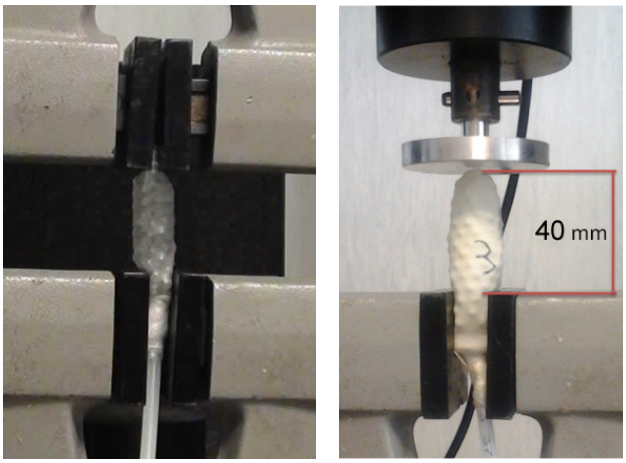

Figure 5.2: Left: Tension test setup. Right: Compression test setup.

kPa (7.5 PSI-A), and 10 kPa (1.5 PSI-A). The pressures were achieved by a two-stage, oil-based vacuum pump (Mastercool 90066-2V-220) and measured by an absolute pressure sensor (Honeywell 0-30 PSI). Thus, all pressure measurements were done in absolute pressure.

Additionally, tensile tests were performed on the membranes to quantify the Young's modulus of each material. These experiments were done at atmospheric pressure (101 kPa/15 PSI-A) without granules.

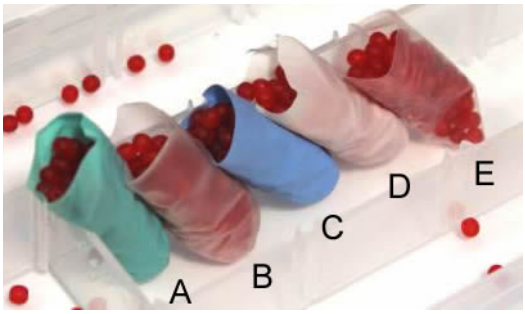

Figure 5.3: The various membranes tested for their effect on a granular jamming joint were, from left to right: A) vitrile, B) vinyl, C) nitrile, D) latex, and E) polythene.

For the bending tests, the joint tip was deflected horizontally by a motorized linear rail

for a distance of 10 mm at a speed of 1 mm/sec, as seen in Fig. 5.1. The resistive force done by the joint was measured by an ATI Nano17 Force/Torque Sensor. This experimental setup was controlled and recorded with LabVIEW. Ten experimental trials were performed for each membrane at each pressure level.

The tensile experimental setup can be seen in Fig. 5.2. The ends of the joint are held in place by grippers, and are deflected with a 20% strain. The velocity of the tensioning was 10 mm/min. Five experimental trials were performed for each membrane at each pressure level.

Fig. 5.2 shows the compression experimental setup. Similar to the tensile experiments, the joint's base was fixed using grippers, and a displacement of 20% strain was performed. The velocity of the compression tests were also set to 10 mm/min. Five trials were performed on each membrane at for the three pressure levels.

The tension and compression experiments were done with an Instron 5900 Testing System. Data from the first trial of each experiment with the Instron were not used, due to the Mullins effect [57].

The hysteresis value H is normalized for each experiment and is calculated by the difference in area of the loading (top) and unloading (bottom) curves divided by the area of the loading curve ($H = \frac{A_{load} - A_{unload}}{A_{load}}$).

5.3 Membrane Material

Figs. 5.4, 5.5, 5.7, and 5.9 refer to the experimental data captured in loading and unloading the system. Figs. 5.6, 5.8, and 5.10 summarize the relationship between pressure and effective Young's modulus for each membrane type from the experimental results for the bending, tensile, and compression tests, respectively. The individual results show the measured force or stress for given deflections, the hysteresis, and the variability for each

of the membranes under each test.

5.3.1 Membrane tensile analysis

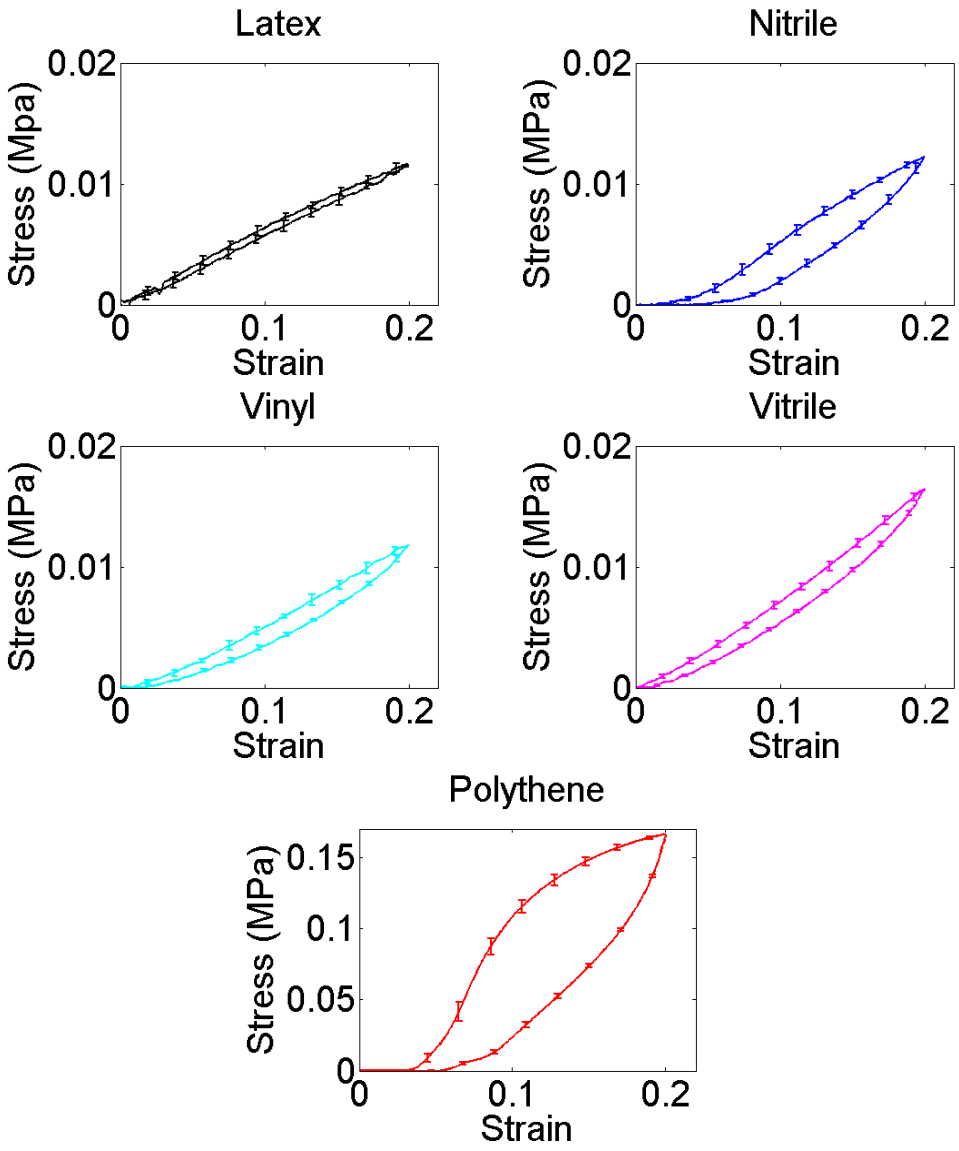

Figure 5.4: Five different membranes tested with 20% tensile strain. (Note: Polythene is on a different scale to show detail)

To see the behavior of the membrane and empirically measure the effective Young's modulus E, tensile tests were performed on the membranes themselves. Young's modulus

E was calculated by the slope of a linear plot fitted onto the experimental results, as $E = stress/strain$. The empty membrane cylinders were subjugated to 20% strain. The thickenesses of the membranes were 0.07 mm, with the expection of the polythene, which was 0.06 mm in thickness. The volume of the membrane cylinders were all 7070 mm^3.

Under tensile strain, latex, vinyl, and vitrile exhibit fairly linear behavior with very little hysteresis, as shown in Fig. 5.4. Nitrile has a relatively large hysteresis, similar to that of the polythene. In the case of polythene, E was still derived from a fitted linear curve, despite the nonlinear behavior. This was approximation was taken, as it exhibited ten times greater stress than the former four membrane types and the resulting E value also showed to similarly greater. From observation, the polythene material's large hysteresis is due to permanent deformation caused by stretching the membrane.

Table 5.1: Summary of membrane properties

Membrane Type	**E (MPa)**	**Stress (MPa)**	**Hysteresis**	**Variability**
Latex	0.06	0.01	0.07	0.006
Nitrile	0.06	0.01	0.52	0.004
Vinyl	0.06	0.01	0.24	0.006
Vitrile	0.08	0.02	0.20	0.007
Polythene	0.83	0.17	0.53	0.060

5.3.2 Bending results

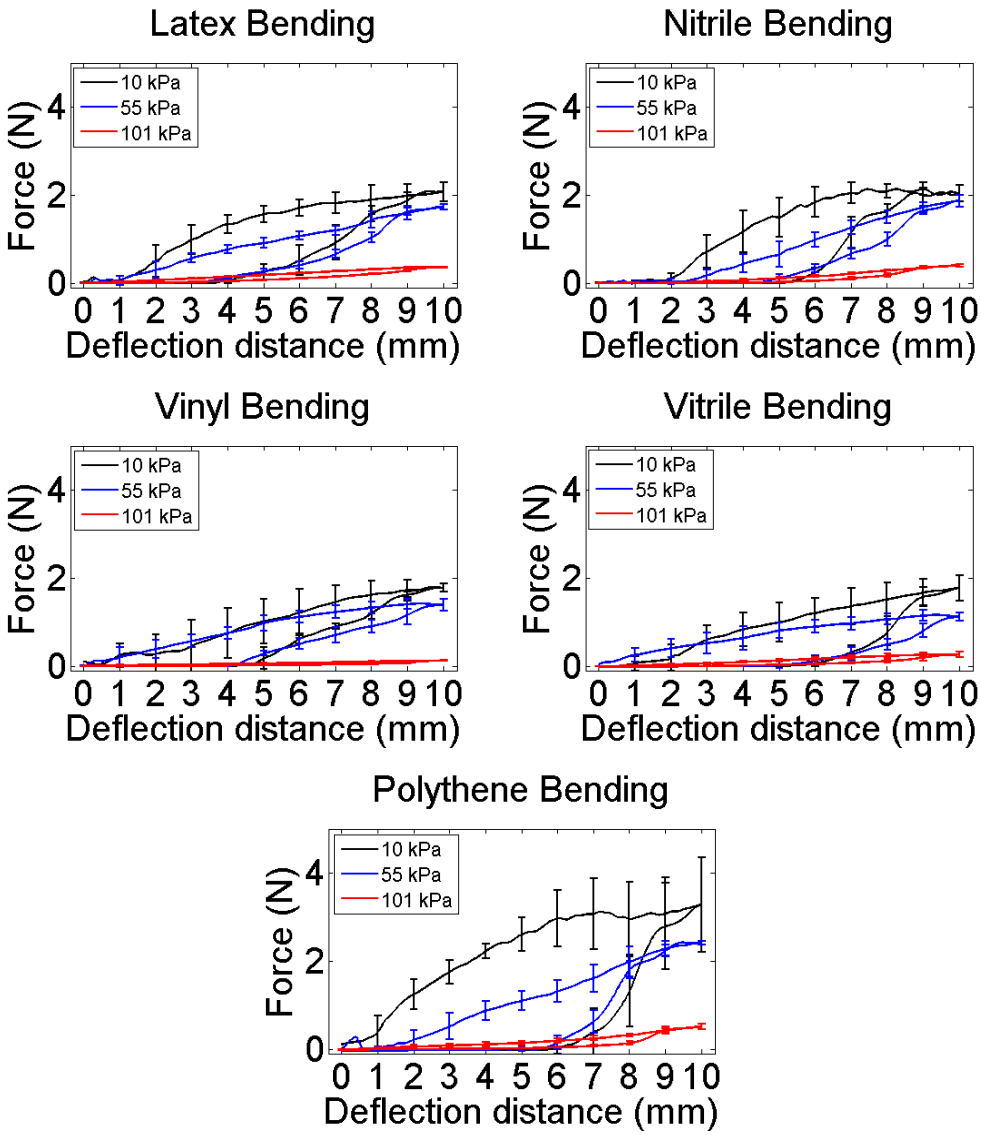

Figure 5.5: Bending experimental results from the five membrane types (latex, nitrile, vinyl, vitrile, and polythene) for three internal pressures (101, 55, and 10 kPa).

From section 3.2.2.1, there is a maximum a bending force of 4.82 N as E increases infinitely, suggesting that the material with the highest E will exhibit the greatest bending force. From the membrane results in Fig. 5.4, polythene was the stiffest membrane type.

Thus, will it exert 4.82 N?

In Fig. 5.5, polythene indeed showed to achieve the highest bending force at 3.12 N, about 30% greater than the next highest, nitrile. However, not only was this at a cost of hysteresis and variability, but failed to achieve the 4.82 N from the numerical model. This shows that a ten-fold increase in E, as seen in Fig. 5.4, does not increase the bending force by the same amount. The poor performance in hysteresis is due to the high level of permanent deformation the joint undergoes after being loaded, but not from the membrane itself; namely, the interaction between the granules and the membrane, as well as granules to granule interactions, caused the joint as a whole to deform permanently. At 7 mm, the joint is no longer in contact with the force sensor on the return trip, and thus no forces are recorded. On the same macro scale, each of the joints exhibit similar amounts of hysteresis at atmospheric pressure. Without a pressure differential, the resistance to bending and the elasticity of the joint is dominated by the membrane, rather than the granules. Nitrile and latex have the second and third highest stiffness ranges, and they perform better than polythene in terms of both hyseresis and variability. Those two materials perform similarly across all the measured parameters with each other, as well. Vinyl and vitrile have lowest stiffness ranges, and have similar amounts of variability with latex and nitrile.

Fig. 5.6 summarizes the E values for each of the membranes under different pressures. Latex and nitrile exhibited similar properties, while vinyl and vitrile also behaved similarly. Polythene showed the largest E, indicating that the membrane's E value correlates to the elasticity and stiffness of the joint as a whole. Section 3.3.1 shows how E was derived.

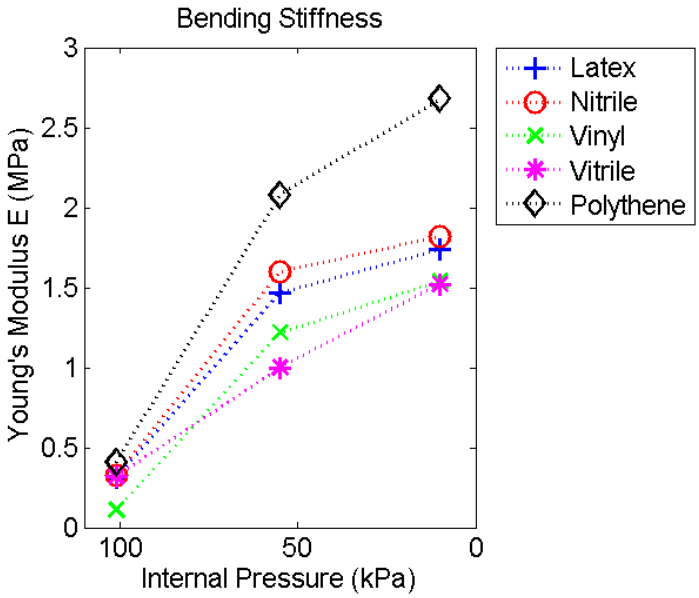

Figure 5.6: Relationship between vacuum pressure and stiffness for bending

A pairwise Mann-Whitney U test was perfomed to ascertain whether the influence of different membranes on the variability of the peak stiffness of the joint were significantly different from each other. In the unjammed state (pressure = 101 kPa), all pairs were significantly different with the latex-vitrile pair of $p < 0.005$, and all other pairs giving $p < 0.0003$. Since the peak stiffness of the unjammed state mainly depends on the membrane stiffness, this implies that there is a base level difference in the bending stiffness due to the different types of membranes we selected for this experiment. Some pairwise comparisons changed their level of statistical significance when we applied the maximum level of vacuum (10 kPa), such as with vinyl and vitrile losing a significant difference ($p > 0.8$). This implies that there is an interaction effect between the type of membrane and the level of vacuum. In order to test whether there is a significant overall interaction effect between pressure and membrane type, we performed an n-way ANOVA test. We found that, while both the pressure and membrane type have a significant effect on the stiffness of the joint separately ($p < 0.0001$), there is also a significant interaction effect

between the membrane type and pressure ($p < 0.0001$).

In addition to the statistical tests on the peak lateral force, we tested whether membrane type causes a significant difference in the force/strain profiles shown in Fig. 5.4. Each force profile is significantly different from others ($p < 0.0001$) for the 10 kPa pressure level. For the 101 kPa pressure level, only nitrile and vitrile are similar ($p > 0.1$).

Table 5.2: Summary of membrane effects in bending experimental results

Membrane Type	**Pressure (kPa)**	**Force (N)**	**Hysteresis**	**Variability (N)**	**E (MPa)**
Latex	101	0.36	0.42	0.01	0.31
	55	1.72	0.43	0.08	1.47
	10	2.03	0.51	0.17	1.74
Nitrile	101	0.39	0.36	0.02	0.33
	55	1.86	0.40	0.09	1.60
	10	2.12	0.51	0.14	1.82
Vinyl	101	0.13	0.52	0.01	0.11
	55	1.42	0.50	0.12	1.22
	10	1.79	0.44	0.21	1.54
Vitrile	101	0.27	0.55	0.02	0.32
	55	1.16	0.69	0.11	1.00
	10	1.77	0.61	0.18	1.52
Polythene	101	0.48	0.49	0.03	0.41
	55	2.42	0.48	0.13	2.08
	10	3.12	0.73	0.36	2.68

5.3.3 Tensile results

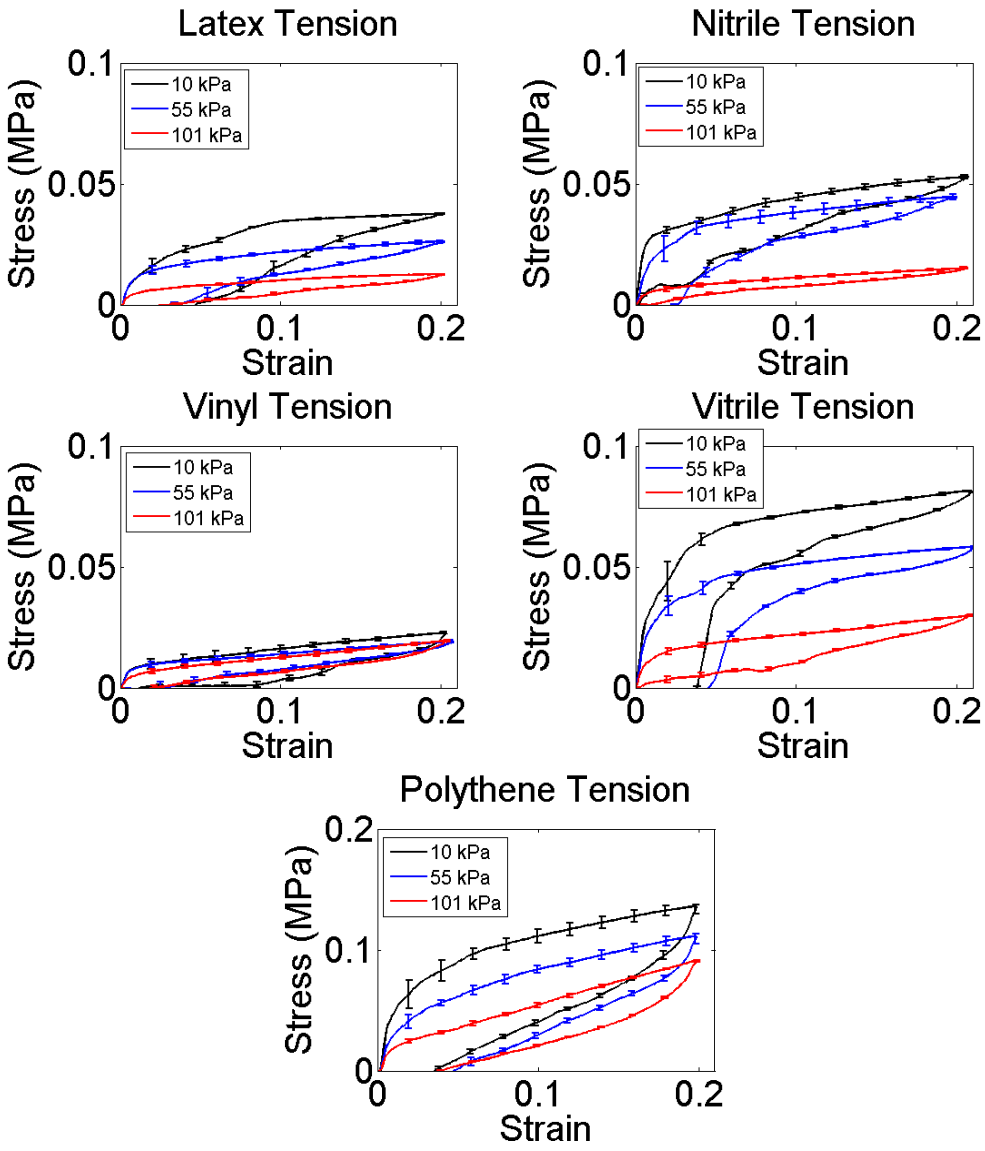

Figure 5.7: Tensile experimental results from the five membrane types (latex, nitrile, vinyl, vitrile, and polythene) for three internal pressures (101, 55, and 10 kPa) (Note: polythene is on a different scale for detail).

The tensile tests demonstrate that, in tension, the mechanical properties of the membrane affect the performance of the joints in jammed states. At an atmospheric 101 kPa internal pressure, the joint behaved similarly to the membrane-only tensile test in Section 5.3.1.

However, lower pressures altered the joint's stiffness characteristics.

Fig. 5.7 and Table 5.3 show that the mechanical properties of latex, nitrile, and vinyl are rather similar, but nitrile presents a larger hysteresis. On the other hand the polythene is one order of magnitude stiffer than the other membranes and for a 20% strain, it undergoes permanent deformation thus presenting a higher hysteresis. In general, the granule-filled joints in these tensile tests present an elastic (linear) behavior for small deformation, after which the slope of the graphs changes considerably. Indeed, the joint tends to act as a unique material; after this linear region the mechanical behaviour of the joint can be compared to a sample after reaching its yield stress. The internal particles have been separated from the applied load. According to this interpretation in the employment of the joint in stiffness varying applications in order to take advantage at best of the different performances of the joint in should be used in the pseudoelastic tract thus for a range of deformation that it is different for each vacuum level.

The latex membrane filled with glass spheres in the case of atmospheric pressure presents a trend similar to the membrane alone. When 55 kPa vacuum is applied the slope of the initial elastic tract more than doubles from 0.56 MPa to 1.6 MPa; when the vacuum is increased to 10 kPa the slope of the initial tract further increase to 1.8 MPa. Hysteresis in the case of the test performed at atmospheric pressure is 0.0038 and increases considerably when vacuum is applied to 0.0108 at 55 kPa up to 0.0138 at 10 kPa, confirming that a high level of energy is dissipated in the jammed configuration due to internal friction and permanent deformation of the membrane.

Similarly to the latex membrane, nitrile has a behavior mainly due to the elastic properties of the membrane at atmospheric pressure. When vacuum is applied, the slope of the elastic tract increases from 1.8 MPa of the atmospheric pressure, to 3 MPa at 55 kPa to 6.3 at 10 kPa. It is interesting to observe that the elastic tract for 10 kPa extends to higher

deformation than in the case of latex.

When at atmospheric pressure, the Young's modulus E of the joint with each membrane are similar to the values found in the membrane-only tests, apart from polythene. Thus, without jamming, the tensile strength of the joint is limited by the membrane, with granules playing little effect. However, with vacuum, latex, nitrile, and vitrile doubled and tripled their E values. Vinyl displayed no significant change, and polythene increased by 50%.

From the variability standpoint, the variability between trials were fairly low, 1-2 orders of magnitude smaller than those from the bending tests.

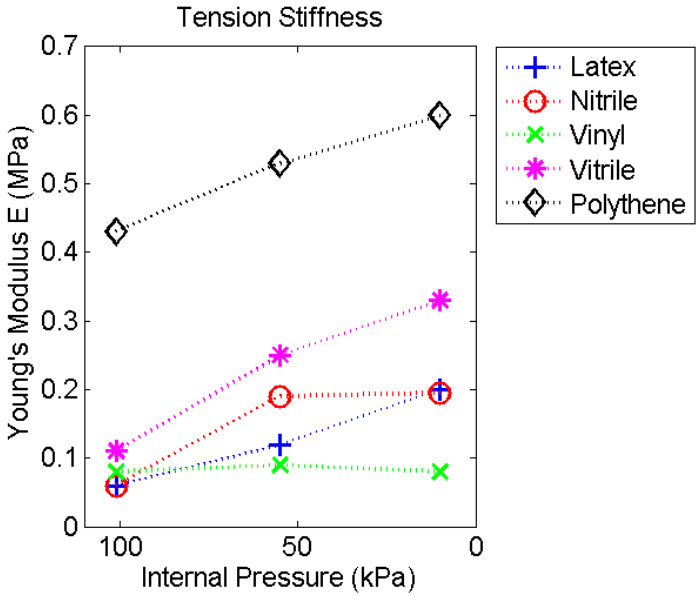

Figure 5.8: Relationship between vacuum pressure and stiffness for tension

Fig. 5.8 shows some materials, such as nitrile, vinyl, and vitrile decrease in stiffness from 55 to 10 kPa. On the other hand, latex and polythene increase linearly as more vacuum is drawn.

Performing pairwise Mann-Whitney U tests on the peak stresses show that, at 101 kPa, all membranes were significantly different from each other ($p < 0.008$), with the exception

of nitrile and vinyl ($p > 0.4$). At 10 kPa, these membranes, like all other pairs, become significantly different ($p < 0.008$). This indicates that though membranes may exhibit similar properties when the joint is unjammed, they become distinct when vacuum is applied implying a significant interaction effect between the membrane types and level of vacuum.

The Mann-Whitney U tests for the stress/strain profiles show that, at 10 kPa, each membrane is significantly different from the others ($p < 0.0001$), apart from latex and nitrile ($p > 0.1$). At 101 kPa, latex is similar to nitrile and vinyl ($p > 0.2$), and nitrile is somewhat similar to vinyl ($p > 0.05$).

Table 5.3: Summary of membrane effects in tension experimental results

Membrane Type	Pressure (kPa)	Stress (MPa)	Hysteresis	Variability (MPa)	E (MPa)
Latex	101	0.01	0.40	0.0002	0.06
	55	0.03	0.36	0.0010	0.12
	10	0.04	0.30	0.0011	0.20
Nitrile	101	0.02	0.26	0.0009	0.06
	55	0.04	0.28	0.0020	0.19
	10	0.05	0.30	0.0005	0.19
Vinyl	101	0.02	0.37	0.0006	0.08
	55	0.02	0.35	0.0009	0.09
	10	0.02	0.53	0.0012	0.08
Vitrile	101	0.03	0.40	0.0006	0.11
	55	0.06	0.30	0.0013	0.25
	10	0.08	0.27	0.0014	0.33
Polythene	101	0.11	0.40	0.0010	0.43
	55	0.14	0.43	0.0030	0.53
	10	0.19	0.42	0.0042	0.60

5.3.4 Compression results

In most elastic materials, such as rubber, the Young's modulus can be found from tension or compression. However, because the structure of the joint is composed of granular

material, it is possible for the joint to behave differently under compression than under tension.

The compression tests differ largely from either the bending or tensile tests, as the joints show relatively little stress until 0.15 to 0.18 compressive strain. The reason for this is likely two-fold. The first is due to the granules having restructured and repacked to a different jammed state after the first cycle. The dotted lines in Fig. 5.9 show this occurring, as granule rearrangement can be seen in drops in stress. Secondly, the membrane could have undergone permanent changes, known as the Mullins effect, after the first cycle. As the membrane behavior stabilizes after this first cycle, the analysis is done on the subsequent trials.

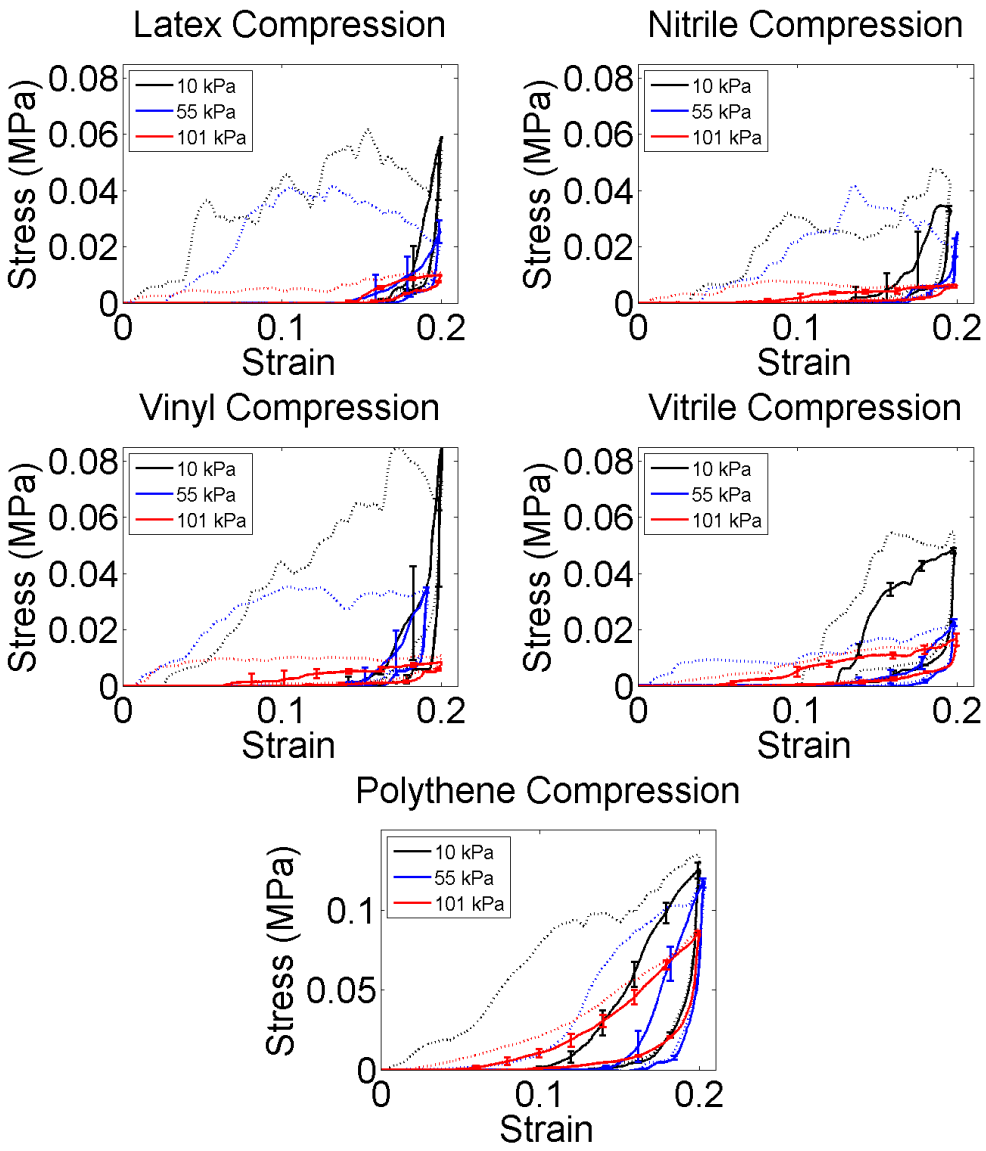

Figure 5.9: Compression experimental results from the five membrane types (latex, nitrile, vinyl, vitrile, and polythene) for three internal pressures (101, 55, and 10 kPa). The dotted lines represent the first loading cycle, which was omitted from the analysis due to the Mullins effect. (Note: polythene is on a different scale for detail), with 4 mm smooth glass spherical granules.

In Fig. 5.9 and Table 5.4, the hysteresis of each membrane varies significantly between atmospheric and vacuumed pressures. In atmospheric conditions, the values of hysteresis for all the membranes are about 2-3 times larger than at medium vacuum. Vitrile and

polythene have similar hysteresis values at 10 kPa with atmospheric pressure, whereas the other membranes do not show such an increase in hysteresis. Through observation, the higher hysteresis at atmospheric pressure can be attributed to the membranes' inability to return to its initial shape when the Instron returns to its initial position. However, at 55 kPa, the stress the membrane imposes on the granules enable them to maintain the joint structure after the Instron moves back. This same behavior is observed at 10 kPa for latex, nitrile, and vinyl. For vitrile and polythene, the 20% compressive strain is observed to cause some permanent deformation in the joint, possibly from a restructuring of the granules.

Like the tensile results, from the variability standpoint, the variability between trials were fairly low, 1-2 orders of magnitude smaller than those from the bending tests.

Young's modulus E was calculated from the slope of the non-zero values between 0.18 to 0.2 strain.

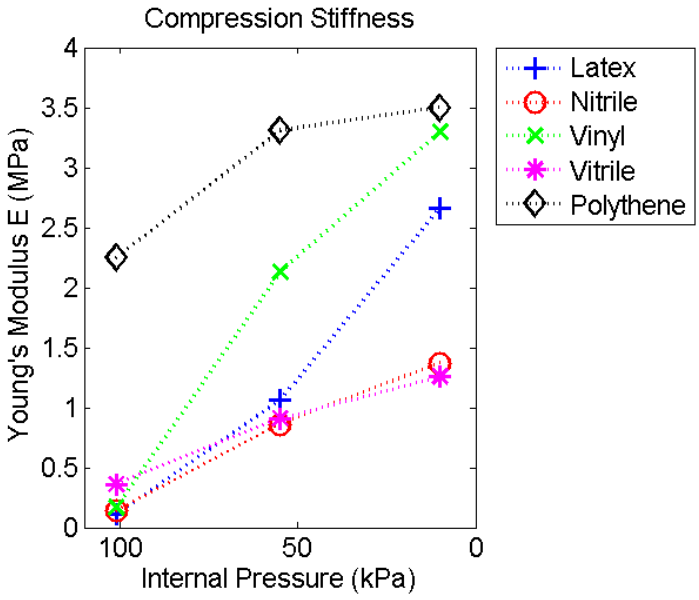

Figure 5.10: Relationship between vacuum pressure and stiffness for compression

Fig. 5.10 shows that polythene remained the stiffest material at 10 kPa, though vinyl

exhibited a close stiffness of E = 3.3 MPa. In fact, vinyl showed a drastically larger stiffness range than any other material, with latex a close second. Nitrile and vitrile behaved very similarly in this test.

The pairwise Mann-Whitney U tests for the peak stresses show that, at 101 kPa, each pair is significantly different ($p < 0.008$), though nitrile and vinyl were only mildly different ($p < 0.01$). At 55 kPa, several membrane pairs converge, with latex, nitrile, and vinyl behaving similarly ($p > 0.1$). However, at 10 kPa, all membranes become significantly different from each other ($p < 0.008$), implying that at high vacuum levels, there is a significant interaction effect between the membrane types and the level of vacuum.

The Mann-Whitney U tests for stress/strain compression profiles shows that vinyl and vitrile are mildly similar ($p > 0.05$) at 10 kPa, with all other membrane combinations are distinct ($p < 0.005$). At 101 kPa, the five membranes were significantly different from each other ($p < 0.005$).

Table 5.4: Summary of membrane effects in compression experimental results

Membrane Type	**Pressure (kPa)**	**Stress (MPa)**	**Hysteresis**	**Variability (MPa)**	**E (MPa)**
Latex	101	0.01	0.12	0.0002	0.11
	55	0.03	0.06	0.0009	1.06
	10	0.06	0.04	0.0006	2.66
Nitrile	101	0.01	0.28	0.0003	0.14
	55	0.02	0.02	0.0002	0.86
	10	0.03	0.09	0.0010	1.37
Vinyl	101	0.01	0.30	0.0006	0.17
	55	0.03	0.07	0.0007	2.13
	10	0.08	0.05	0.0016	3.30
Vitrile	101	0.01	0.29	0.0005	0.36
	55	0.02	0.09	0.0005	0.91
	10	0.05	0.21	0.0005	1.26
Polythene	101	0.09	0.20	0.0012	2.25
	55	0.12	0.09	0.0014	3.31
	10	0.13	0.17	0.0017	3.50

5.4 Membrane Coupling

The stiffness of the granular jammed joint no longer significantly improves after a certain deflection point, possibly as the granules shift or no are longer able to maintain good contact with each other. At these instances, the membrane is effectively the only thing resisting the external force.

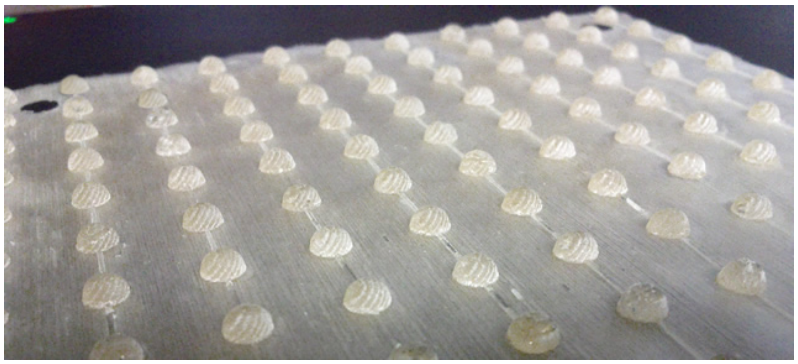

Figure 5.11: A sheet of latex rubber used to create a "bumpy" membrane to couple the granules to the membrane.

To reduce membrane movement, a custom the membrane was designed by embedding 4 mm half-spheres, made of the same membrane material, along the inside of the membrane itself, as shown in Fig. 5.11. This membrane was made with latex.

Fig 5.12 shows that membrane coupling significantly improves the hysteresis and linearity of the system. The results show an improvement over non-coupled, smooth latex. However, although the 10 kPa force was higher than in the smooth latex test in Fig. 5.5, there is a large variance.

Nonetheless, the results from this membrane coupling experiment open a new path of granular jamming system design.

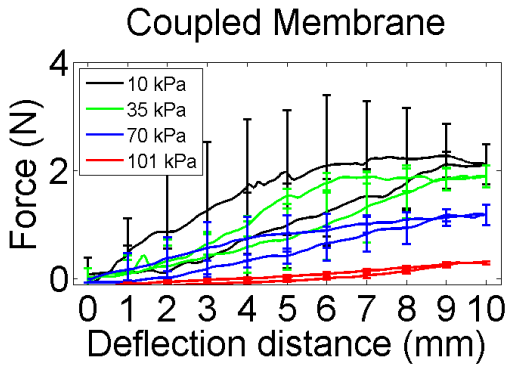

Figure 5.12: Measured data of 4 mm plastic spheres in a latex membrane with 4 mm half-domes lining the inside. The force peaked at 2.27 N.

Table 5.5: Summary of membrane effects in coupling experimental results

Membrane Type	Pressure (kPa)	Force (N)	Hysteresis	Variability (N)	E (MPa)
"Bumpy" Latex	101	0.30	0.13	0.03	0.26
	70	1.20	0.32	0.20	1.03
	35	1.90	0.26	0.29	1.63
	10	2.27	0.37	0.67	1.95

5.5 Discussion

The comprehensive tests on latex, nitrile, vinyl, vitrile (blend of vinyl and nitrile), and polythene presented in this chapter spark many interesting points in the world of robotic granular jamming. The material of the membrane affects not just the stiffness range, but the variability and hysteresis, as well. In the case of the polythene, a high stiffness was achieved, likely due to its high tensile modulus characteristic. However, as polythene does not stretch elastically it has a high level of hysteresis in a trial. Nonetheless, this does not limit granular jamming from being repeatable per se. Despite hysteresis or inelastic deformation shown in Figs. 5.5, 5.7, and 5.9, once air is reintroduced into the joint, it is effectively reset and ready to operate again. In other words, when the joint as a whole exhibits inelastic behavior or "permanent" deformation, may it be from the membrane or

granules, the joint can retain its maximum stiffness characteristic upon unjamming and re-jamming the joint. The re-jamming process compensates for changes in previous granule packings and membrane deformations, as shown by the low variability in the results. This is unlike conventional materials where inelastic deformation can be permanent and often translates to poor repeatability. Thus, as a robotic mechanism, the variability between granular jamming trials is the important factor for its repeatability. For example, in the case of polythene in tension, while it exhibited an average of 42% hysteresis per trial, it only exhibited and average of 2.2% in variability between trials. These results provide design considerations for a variable stiffness flexible manipulator, where granular jamming is used to tune the rigidity of an endoscopic device, such as the device seen in Fig. 9.1. The endoscope is soft to be dexterous and compliant when inserted, but can become rigid to provide the camera with a stable platform. Though previous works show that the granules impact the stiffness range and profile of the robotic device, the results show that the membrane also plays a significant role ($p < 0.005$ between most membranes).

The conventional preconception is that a thin, flexible membrane is most ideal for granular jamming, such as latex rubber. However, The results show that this is not the case, with polythene consistently outperforming the rubber-based membranes in stiffness. At atmospheric pressure, the granule-filled joints for each of the membranes performed similarly to one another ($p > 0.1$ for nitrile and vitrile bending), with the exception of polythene. The rubber-like materials latex, nitrile, vinyl, and vitrile tended to have better hysteresis and low variability. However, when vacuumed to 55 kPa and 10 kPa, the joints began to behave much differently from each other. This could be attributed to the interaction between the granules and membrane. At atmospheric pressure, the granules play only a small role. When jammed, the membrane's ability to maintain stress on granules causes the joints to behave more solid-like. For example, during compression in atmo-

sphere, the granules are pushed together and thusly expand the latex membrane. At 10 kPa vacuum, the granules' attempt to expand the membrane is counteracted by the latex's constriction due to pressure. Thus, the measured stress increases 6-fold, as can be seen from Fig. 5.9. On the other hand, nitrile only had a 3-fold increase. This may be from the reduced flexibility of nitrile, as the membrane-only tests in Fig. 5.4 show that it experiences substantial hysteresis. Similarly for polythene, as the material's inherent properties resists expansion, the relative change between atmospheric and vacuum is only about a 50% increase in stiffness.

Additionally, the behaviors of the joints in the three overarching tests showed that, on a macro scale, the granular jamming system behaves as a different type of material in bending, tension, and compression, as the Young's modulus E change depending on the loading direction. Thus, future robotic manipulators using granular jamming must take the performance of desired tasks into consideration, as they differ.

The "bumpy" membrane, seen in Fig. 5.11 and 5.12, proved to less effective than the composite granules, but did significantly improve the hysteresis and linearity over both the 4 mm plastic spheres and cubes with decoupled membranes. While the variability was not improved, membrane coupling remains to be an interesting area to be explored in the field of jamming.

From Chapter 4, changing the granule shape and surface friction can greatly increase the stiffness of the joint. Changing from smooth glass spheres to matte plastic cubes increased the stiffness by 1.8 times. Chapter 4 also shows that stiffness can be increased by using smaller granules. Here, we show that the membrane properties is also a driving factor in achievable stiffness. Thus, future applications for granular jamming must use these factors in consideration.

Chapter 6

The Effects of Fluids in Granular Jamming

Abstract

Granular jamming is conventionally controlled with air, which reduces the mobility of the robot. This is because the compressibility of air requires large vacuum pumps or chambers. Instead, this chapter proposes the use of an incompressible fluid, such as water, to control the stiffness of the mechanism. This comparative study shows that a hydraulic granular jammed joint using de-aired water can both achieve the same stiffness level with just one twentieth of the volume extraction and maintain the same hysteresis level of an air-based system.

6.1 Introduction

This chapter introduces the use of de-aired water to untether granular jamming for a snake-like robot. The previous work on the robot joints involved examining granule types [56] and actuation techniques [55] for this minimally invasive surgical tool [58, 59]. This work was controlled by a vacuum pump which was significantly larger than the robot. For medical robotics, a tethered flexible manipulator is not uncommon, such as with current robotic endoscopes [6], highly articulated probes [21], catheters [16], and surgical platforms [60]. In fact, most robotic surgical tools use tendons, which require a significant amount of space for the backend mechanisms [61]. However, there is an increasing favor for laparo-endoscopic single-site surgery (LESS) and natural orifice translumenal endoscopic surgery (NOTES) [5], and such large backends can cause clashing and obstructions for the surgeons [4]. Similarly, while the snake-like robot itself could be miniaturized, the overall system remained tethered and not mobile. Ideally, a granular jamming module would be a self-contained system, which would allow each robot, snake-like or otherwise, to be attached and detached without contaminating the pneumatic lines by blood or debris. By converting granular jamming from an air-based, pneumatic system to a water-based, hydraulic system, we were able to untether the robot while achieving the same stiffness level [62, 63].

6.2 Methods

Hemispherical acrylic granules 1 mm in diameter were used as the granular media. The variable stiffness joint membrane is a 0.2 mm thick latex cylinder 10 mm diameter by 30 mm long cylinder (2.36 mL volume). Because the Core-snake must largely resist lateral disturbances, its perpendicular stiffness is most critical. As such, bending tests were

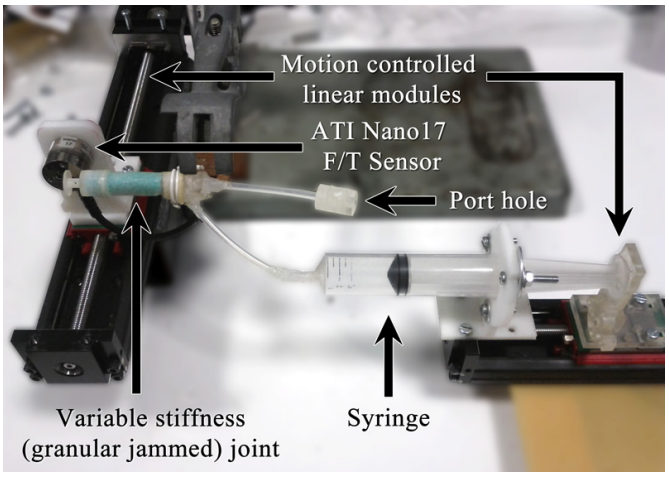

Figure 6.1: Experimental setup for the hydraulic test. For the pneumatic experiments, a pressure sensor was attached to the port hole.

performed. These tests consist of measuring the resulting force when deflecting the joint tip perpendicularly to its axis by 10 mm. An ATI Nano17 Force/Torque sensor measured the resultant force, and a Maxon EC-30 motor powered linear module controlled the deflection distance.

The first experiment consisted of an un-vacuumed pneumatic (air) fluid test. This baseline test was performed with an internal air pressure of 101 kPa (14.6 PSI absolute), which matches the external atmospheric pressure. The baseline test measures the lower bound of the joint's stiffness, or its "soft" state. The upper bound of the pneumatic experiment consisted of continuously vacuuming the joint to an internal air pressure of 18 kPa (2.6 PSI absolute). This was achieved with a Mastercool 90066-2V-220 Vacuum Pump attached to an intermediate 5.3 liter vacuum chamber. The internal joint pressure was measured in-line by a Honeywell 0-30 PSI Absolute pressure sensor. To compare the effectiveness of a pneumatic system in an untethered environment, an air syringe test was performed. Here, 10 mL of air was evacuated via a syringe, and the resulting force was measured.

The second experiment consisted of an un-extracted hydraulic (water) test. This test is similar to the air baseline test, with the exception that the spaces between granules are filled with water, rather than air. The upper bound of the hydraulic experiment consisted of a 10 mL syringe installed in place of the vacuum pump and evacuating the water within the joint. 0.5 mL was water was evacuated to achieve a stiffened joint. The water used is known as de-aired water, where water subjugated to a process of removing dissolved air inside the liquid. Water was placed within a vacuum chamber and vibrated, as the chamber pressure was decreased. This process was done to ensure a uniform and consistent water density. While other hydraulic systems may use oil as the base stock, the use of oil is outside the scope of this chapter. Likewise, polymer solutions and gels can also be interesting interparticle fluids, but are not covered here.

Several experiments were performed to validate the simulation results in Table 3.2, and to compare a hydraulic granular jamming system to a traditional pneumatic system. Between 5-10 trials were performed for each experiment.

6.3 Pneumatic Interparticle Fluid

To have a comparative base for the hydraulic baseline tests, a set of identical pneumatic baseline experiments were performed. One, the joint is in a compliant state; and two, the joint is in a rigid state.

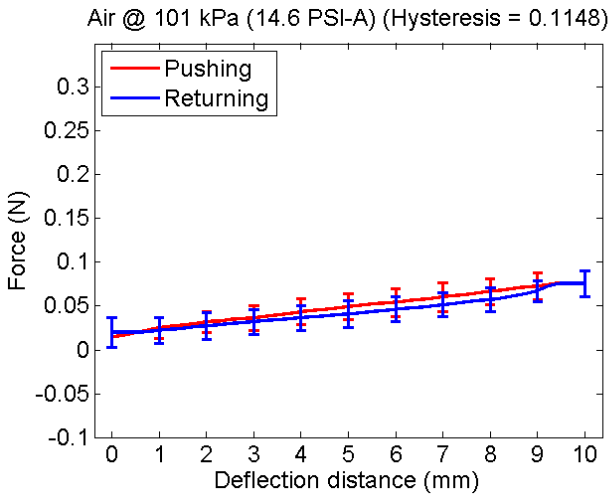

Figure 6.2: Air baseline experiment where the variable stiffness joint is deflected 10 mm, under atmospheric pressure.

Figure 6.2 shows the results of the pneumatic joint "softness" test, where the variable stiffness joint is deflected without a pressure differential to the environment. Here, the granules are in a minimal state of static equilibrium, in which they are settled, but are easily perturbed. This is taken to be the ϕ_{RLP} factor for the pneumatic joint. There is a very low amount of hysteresis at 11%, and low stiffness as well. The peak force measured was 0.08 N. There is a fairly linear behavior to the curves.

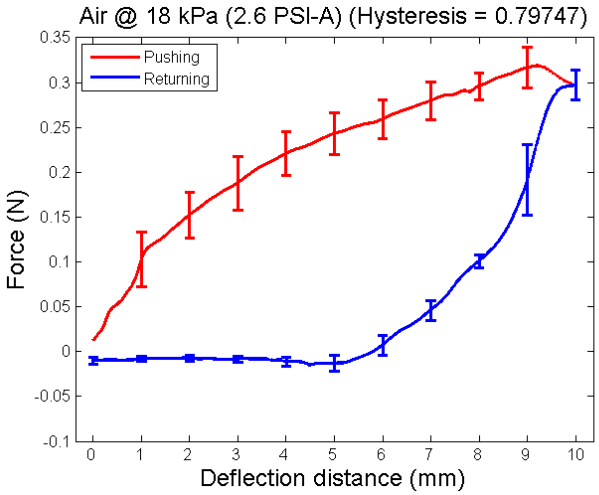

Figure 6.3: Experimental result with a continuous vacuum draw, with internal pressure set to 18 kPa (2.6 PSI-A).

With a continuous vacuum draw of 18 kPa, the variable stiffness joint is able to achieve 0.32 N at the 10 mm deflection mark, as shown in Fig. 6.3.

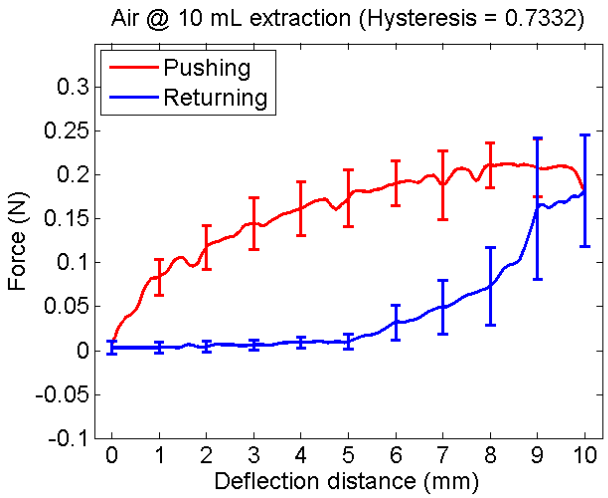

Figure 6.4: Experimental result with 10 mL of air evacuated via a syringe.

As shown in Fig. 6.4, a comparative experiment was performed to highlight the difference between a continuous vacuum draw system and a hydraulic system. The vacuum pump

was replaced with an air-filled syringe, and 10 mL of air was evacuated. This system achieved a peak force of 0.21 N.

Unlike the baseline test in Fig. 6.2, there is a visible cutoff point in the return phases for both the continuous vacuum draw test and air syringe test. In Fig. 6.3, the measurable force reaches 0 N at the 5 mm point, and in Fig. 6.4, it also occurs at the 5 mm point. At this point, the joint is no longer in contact with the force sensor, as the joint has permanently deformed to this state. Experimentally, the joint was reset before the subsequent trial.

Also unlike the baseline test, the pneumatic systems, while under vacuum, exhibit logarithmic plots for both the pushing and returning curves. The pushing curve in Fig. 6.4 quickly maxes out by the 5 mm point, whereas the pushing curve in Fig. 6.3 does not peak until the 8 mm point.

6.4 Hydraulic Interparticle Fluid

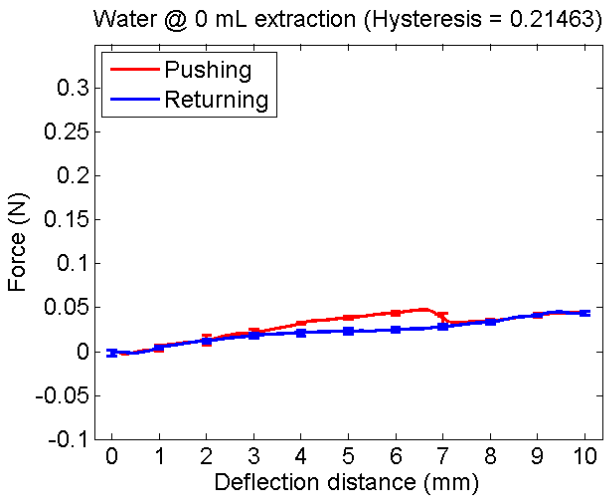

Figure 6.5: Water baseline experiment where the variable stiffness joint is deflected 10 mm, while filled with water and under atmospheric pressure.

In the water "softness" test, as seen in Fig. 6.5, there is a hysteresis level of 21%, and a peak stiffness of 0.04 N. The profile of this experiment is similar to the pneumatic compliant test in Fig. 6.2. However, the higher hysteresis and lower stiffness indicate that the water has a different influence on the granules.

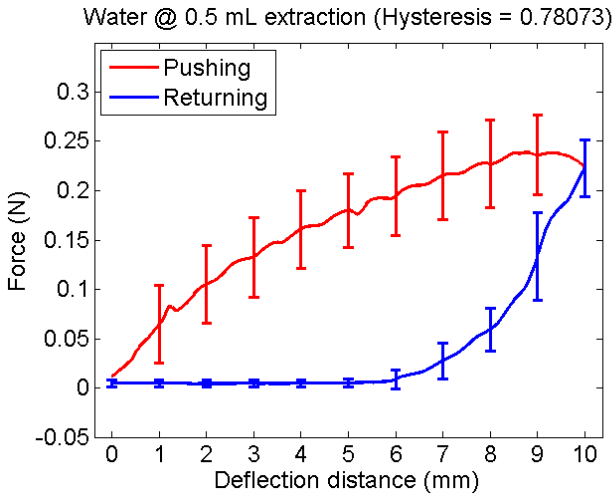

Figure 6.6: Experimental result with 0.5 mL of water evacuated via a syringe.

In contrast to the pneumatic systems, evacuating a 0.5 mL volume of water achieves a peak force of 0.24 N, as shown in Fig. 6.6. With 20 times less volume required, similar stiffnesses can be achieved by a hydraulic system over an air-dependent one.

The hysteresis in the hydraulic system is similar to the continuous vacuum draw test in Fig. 6.3. Fig. 6.6 shows that the hydraulic test also has a permanent deformation at 5 mm, another improvement over the cutoff seen in the air syringe test.

The plot for Fig. 6.6 displays a logarithmic tendency for both the pushing and returning curves, similar to the pneumatic experimental results. Unlike the air syringe test, however, Fig. 6.6 does not begin to max out until the 8.5 point.

6.5 Discussion

Although our experiments cannot confirm if the ideal ϕ_{RLP} was achieved, as the granules were not sufficiently perturbed by motion, the experiments suggest that the ϕ_{RLP} for a fluid is higher than for air. This can be seen from the decreased stiffness exhibited in the 0 mL water extraction test (Fig. 6.5) versus the 101 kPa air pressure test (Fig. 6.2). This difference in values is likely attributed to the fluid decreasing the friction between granules.

There is a clear difference between the simulation and experimental results, particularly in the estimation of maximum stiffness. Eqn. 3.2 and 3.6 calculate an estimated force F_{ext} of 0.53 N for the hydraulic system, but the experimental data show a measured force F_{ext} of 0.24 N, less than half the predicted value. Similarly, the pneumatic system was predicted to sustain a force of 0.43 N, but the experimentally measured force was only 0.32 N. There are several possibilities for these discrepancies. One explanation may be that the assumption that the granules are in an optimally jammed state–all of the granules are a clustered state ($f = N_c/N = 1$)–is not correct, as it could be possible that there are free granules ($N_f > 0$), reducing the overall stiffness of the joint. The other assumption was that hemispherical granules and spherical granules will exhibit the same results may also be incorrect. While the simulations assume spherical, the experimental granules were hemispherical. Additionally, friction losses and the movement of granules were not considered in the simulations, which could account for part of the difference in force values.

Figure 6.6 shows that a hydraulic system can achieve the same stiffness levels as a pneumatic system requiring 20 times more volume to decrease its internal air pressure, as shown in Fig. 6.4. The incompressibility of water creates a vacuum effect when the fluid is evacuated, and because the granules can make up 50-80% of the joint volume,

the amount of water required is small. In turn, the evacuation chamber can also be small, miniaturizing and mobilizing the system. From the hysteresis and curve behaviors, the hydraulic system is more similar to the continuous vacuum draw system. The stiffness characteristics of a water-filled joint in a unstiffened state were the same as an air-filled joint, as seen in Fig. 6.2.

However, while the use of water has many advantages over air, for a granular jamming system, there are also several disadvantages observed from our experiments. In a pneumatic system, particularly one involving a continuously running vacuum pump, leaks within the system would decrease the stiffness performance of granular jamming, but not render it unusable. For a hydraulic system, however, the fixed-volume syringe could not overcome leakages. When the hydraulic system began filling with air due to a leak, the variable stiffness joint could no longer stiffen, even if the syringe was drawn the full 10 mL. Reversing the syringe tended to expand the membrane, rather than release the air, as well. Another disadvantage of a hydraulic system is that the weight of water may be too much for the system. Though the hydraulic system can achieve the same stiffness as a pneumatic one, the mass of the water collected in a chamber at each joint would add weight to a multi-jointed snake. However, joint design or compensation related to the added weight is outside the scope of this chapter.

It should be noted that the hydraulic system could theoretically achieve a higher stiffness if the syringe in the experimental setup were more robust. Though the hydraulic pressure was not measured, the author estimates that full evacuation was not achieved in the joint. The brackets supporting the syringe were flexing during the experiment, which could have skewed the experimental results. The linear module and motor, however, were able to actuate and maintain a stable position.

To test the feasibility of transforming granular jamming into an untethered system, a 3

volt, battery powered DC motor was attached to the linear module controlling the syringe (Fig. 6.1). The motor was able to successfully jam the joint by evacuating 0.5 mL of water and holding its position on the linear module.

The lower force ranges found in this chapters is due to a change in joint size and granule type. In previous chapters, a 15 mm diameter by 40 mm long column was used, whereas this chapter used a 10 mm diameter by 30 mm long column. Eq. 3.12 shows that the moment of inertia I increases by a power of 4 as the radius increases. Also, the friction coefficient for the acrylic granules used in these experiments is lower than the granules used in previous chapters.

Chapter 7

Granular Jamming-based Actuators

Abstract

Soft robotics have opened a new field of flexible and dexterous manipulators. However, research on actuators to maximize a dexterous robot's workspace remain in their infancy. For a snake-like robot, actuation is emphasized on joint bending, which is the control of the bending angle and curvature. State of the art actuators can only independently control one of the two variables. This chapter presents a granular jamming integrated actuator (JIA) which can control both the bending angle and joint curvature independently. The JIA achieves this with its design, which consists of a granular-filled, bellowed walled membrane wrapped in a braided fiber sleeve. When inflated with positive pressure, the JIA actuates in the axial direction. When the air flow is reversed and vacuum is achieved, the granules within the actuator stiffen it. By using granular jamming, JIAs in a bundle can restrict the movement of a neighboring elongating actuator. Tests presented here show that a bundle of this actuator type can vary its bending curvature, while maintaining a desired angle, by modulating the pressure differential between actuators.

7.1 Introduction

Flexible and soft robotics is a growing field in the world, as these compliant mechanisms provide the benefit of dexterity. In the medical field, soft surgical robots provide the additional benefit of reducing the amount of bruising tools can cause a patient [6]. As the medical industry advances, interest for MIS in a magnetic resonance imaging scanner (MRI) has begun to grain traction. However, MRI environments sets limits to actuator types and designs, as electric and piezoceramic motors are not MR-compatible [9, 10]. Thus, pneumatic actuators are considered ideal MR-compatible actuators for their decoupling with electromagnetism, as these actuators are not dependent on metallic materials [11]. Moreover, pneumatic actuators can have lightweight and compliant structures, making them a popular choice for general robotics [12]. As granular jamming also uses pneumatics for control, it is possible to create a hybrid pneumatic actuator with granular media.

To enable pneumatic actuators with stiffness and impedance control, granular media is filled within the membrane, as shown in Fig. 7.3. When inflated with positive pressure, the granules neither contribute nor hinder the performance of the actuator. However, when vacuum is applied with negative pressure, the actuator increases in rigidity via granular jamming. Previous work by external groups have used granular jamming as a supplementary stiffness mechanism for a robot with different actuation mechanisms, though preliminary work on integration between pneumatic actuators and granular jamming have been explored by [36] and [37]. Nonetheless, these works are either not applicable to a snake-like robot or are not truly an integration between pneumatic actuators and granular jamming. Work by [55] is the first to present an integrated granular jamming McKibben actuator.

This chapter studies novel variable stiffness actuators based on granular jamming and

pneumatic muscles. The first design is a McKibben actuator filled with granules. The second is an elongating silicone actuator was filled with plastic granules to stiffen the structure when rigidity is required. The stiffened actuator can be used for two purposes. First, it is to provide platform stability to the robot. Secondly, a stiffened actuator is used to control the curvature of an actuator bundle. To the authors knowledge, the work presented here is the first integrated actuator capable of decoupled curvature and bending angle control. Minimally invasive surgical devices such as the Core-Snake [64] would benefit from this actuation system, as it increases the workspace and dexterity of the manipulator.

7.2 Contracting Actuators

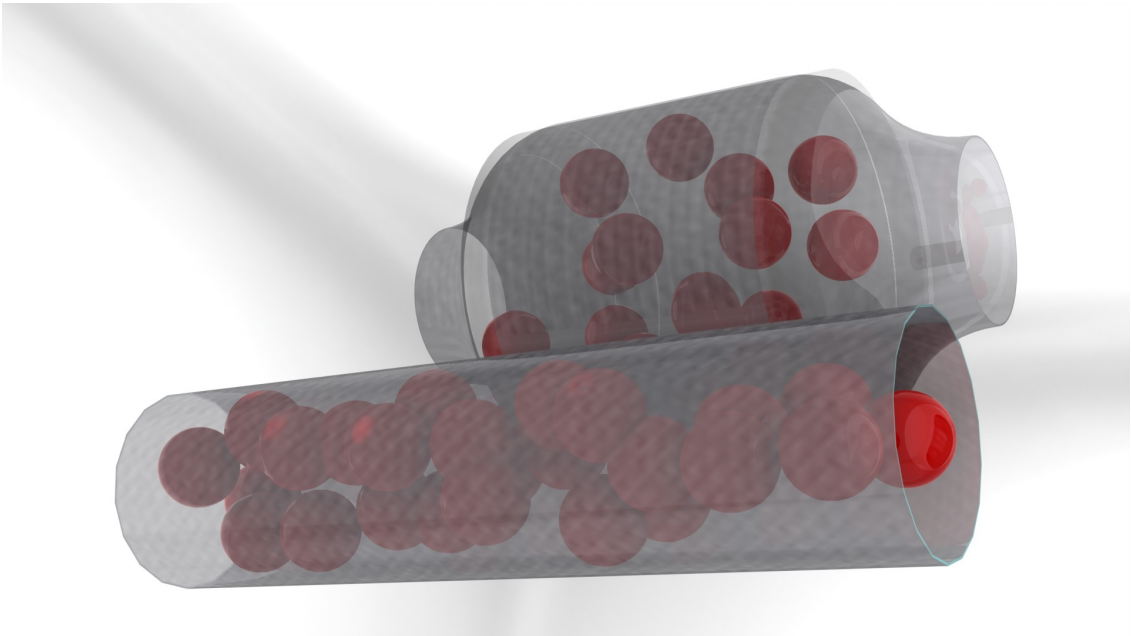

Figure 7.1: The interior of the pneumatic granular jamming integrated actuator designed for contraction (JIA-C). A cylindrical membrane is filled with granular media, and is also wrapped in a braided fiber sleeve. When inflated with positive pressure, the JIA-C contracts. When vacuum is applied, the actuator stiffens.

By reducing the pressure inside the membrane, the joint elements become stiff without a significant volume change. As a proof of concept that these granular systems can also exhibit actuation, we wrapped a mesh around each membrane, and inflated the elements with positive pressure. The elements acted like a pneumatic muscles and contracted. By placing three or more elements at each joint, actuation can be achieved with two degrees of freedom. This is similar to the design used by [37]. Their design consists of a McKibben actuator wrapped in several jamming modules. They achieve actuation by stiffening selected modules and contracting the single pneumatic muscle. However, by integrating the granular jamming element into a McKibben actuator itself and using several in parallel, we can increase the manipulator force. This is because the direction of actuation is not dependent on the stiffness of the jammed elements, but rather on the actuators themselves. Additionally, this design reduces the number of tubing required per joint by at least one. This is due to the fact that the actuation and stiffening mechanisms can share the same line, whereas [37]'s design requires an additional, independent line for the center actuator. Future designs of manipulator can reduce the number of required pneumatic lines even further. Two main lines, one for compressed air and another for vacuum, can run down the length of the robot, and each joint will have their own lines branching off of the two mains.

Our actuators respectively achieved 10% and 15% strain at gauge pressures of 10 and 40 PSI, respectively. This is about 2-4 times higher than unwounded shape memory alloy (SMA) wire, which achieve about 4% strain, not to mention that a pneumatic muscle can achieve much larger forces. Another advantage over SMAs or conventional push/pull rods is that this design, without metal components, could be compatible for magnetic resonance imaging (MRI). One issue with this design, however, is that when actuated, the increase in internal volume can rearrange the granules in an undesirable manner. While

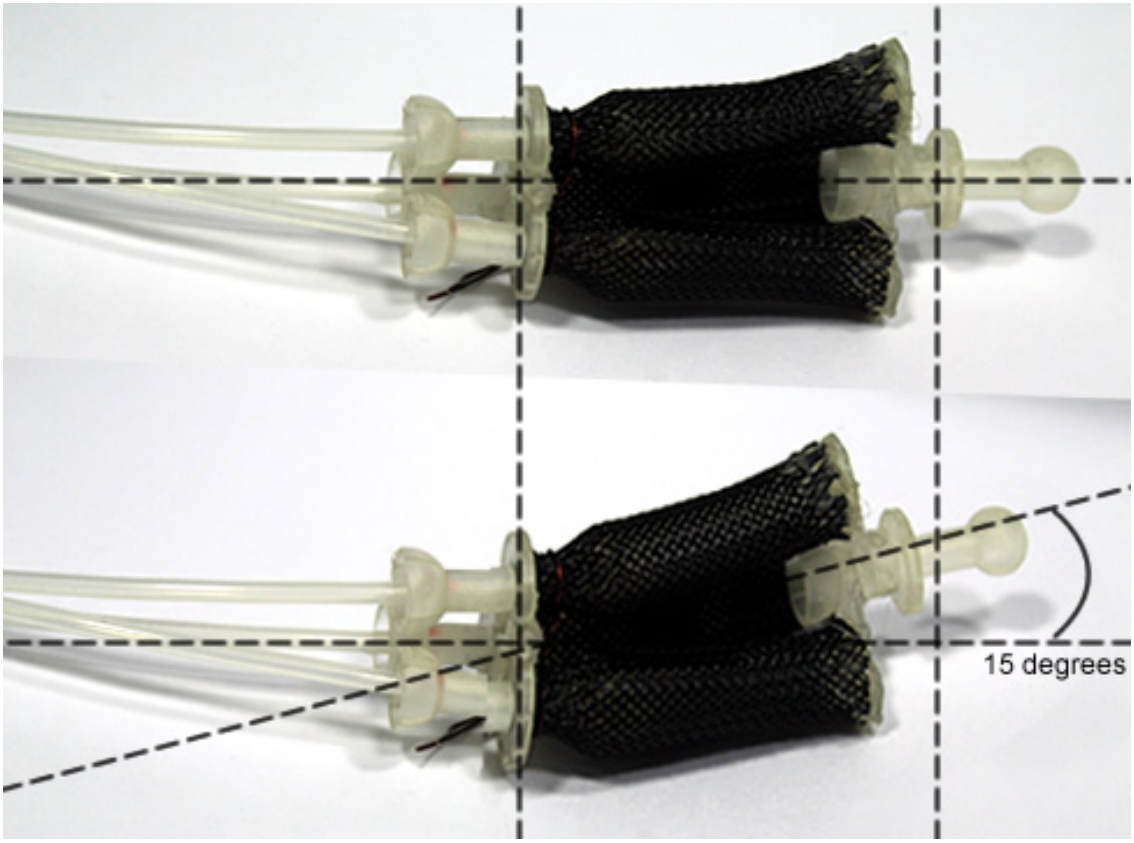

Figure 7.2: A set variable stiffness actuators shown with one actuator activated at 55 PSI absolute (40 PSI gauge). The change in angle is low at 15 degrees. Though all of the actuators were filled with granules, the two other elements were neither actuated or stiffened.

on its side, the problem is minimal, but when held vertically, the granules in an contracted actuator will collect at the bottom. This problem could be reduced by compartmentalizing the membrane's internal structure or futher coupling each granule to the membrane with strings. The use of density matched fluids could also be a potential solution.

Future work can be done on the bending profiles when one of the three segments at a joint is actuated, while the other two are unactuated, stiffened, semi-stiffened, and actuated. These profiles and the muscle control schemes are, however, beyond the scope of this chapter.

7.3 Expanding Actuators

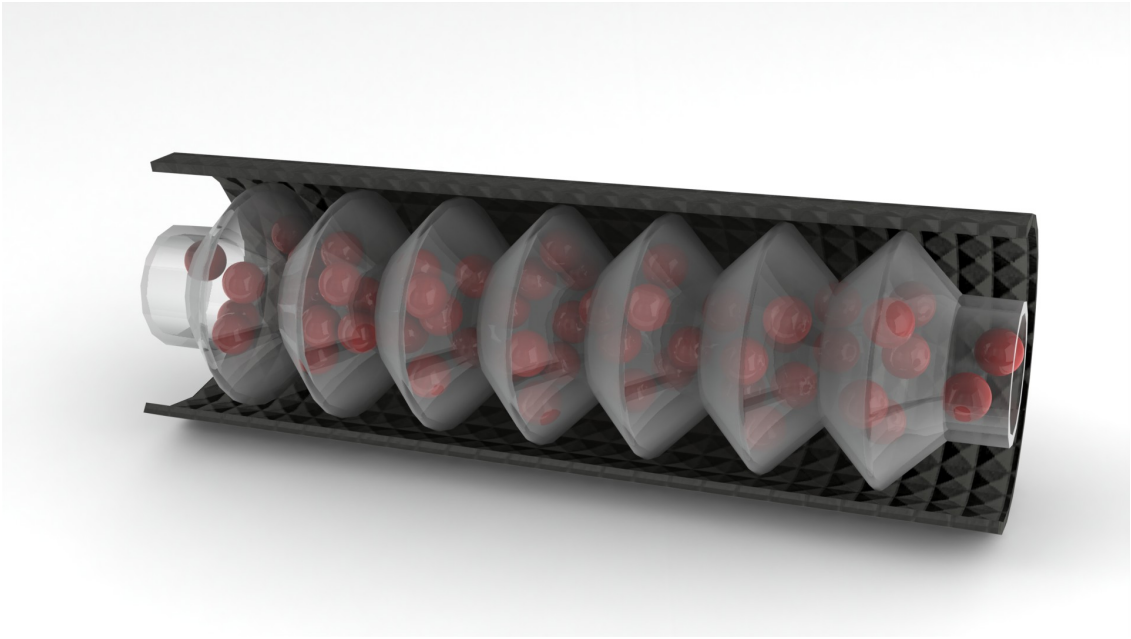

Figure 7.3: The interior of the pneumatic granular jamming integrated actuator designed for elongation (JIA-E). A cylindrical membrane is filled with granular media, and is also wrapped in a braided fiber sleeve. When inflated with positive pressure, the JIA-C elongates. When vacuum is applied, the actuator stiffens.

The JIA-E joint design is a 70 mm long, bellow walled cylinder with a 25 mm outer diameter, as shown in Fig. 7.3. The silicone was then filled with 4 mm spherical granules. The internal pressure of the joint was measured by a Honeywell 0-30 PSI absolute pressure sensor, positive pressure was achieved with a compressor, and vacuum was achieved with a Mastercool 90066-2V-220 vacuum pump. All pressure measurements are on an absolute scale. Forces and external loads were measured by an ATI Nano17 Force/Torque sensor. The data and motion controls were operated in LabView.

Three distinct tests were carried out on the granular jamming integrated actuator to characterize its abilities. The first is a strain test, in which the actuator is inflated between 125 kPa (18 PSI-A) to 175 kPa (25 PSI-A) of pressure. The resulting force and elongation

were then measured. The second test is a stiffness test where the actuator was set to a vacuum pressure of 55 kPa (8 PSI-A) and 20 kPa (2.3 PSI-A). The stiffness of the actuator at 101 kPa (15 PSI-A) was also tested for a stiffness range comparison. The stiffness test was performed by fixing one end and deflecting the tip of the actuator 20 mm, as an inflated actuator is most susceptible to perpendicular external loads. Lastly, a bending test was performed to characterize the variable bending angles and curvatures a bundle of actuators can achieve by alternating actuators between positive and vacuum pressure states. In this test, two granular jamming integrated actuators were placed in parallel, and the bending angle and curvature of the joint were measured as the pressure level between the two actuators was varied. The bends were captured with a digital camera and image processed in Matlab.

7.3.1 Elongation

Various designs were considered and tested for the pneumatic actuator, including the traditional McKibben actuator mechanism, fiber-lined smooth membrane, and bellowed walls with an outer braided fiber sleeve. Because granules are packed inside the actuator to double it as a stiffening mechanism, considerations for the granule distribution during and after actuation must be made. The increase in diameter of the JIA-C actuator when contracted can cause the granules to redistribute unevenly. Namely, when the diameter is increased, the granules fall under gravity to fill the new diameter. This affects the relaxed shape of the actuator, reducing its achievable strain for the next trial.

Thus, an elongating mechanism was designed, as the inner diameter remains constant when actuated. This prevents granules from collecting in one area.

The angle between the bellows was chosen at 40 degrees to make space to hold more granules, which effectively increases stiffness when needed. The granules tend to get

stuck between bellows of smaller angles which affect the natural shape of the membrane. Fig. 7.4 shows how a large angle can achieve higher granular packings, at a cost of maximum strain; similarly, a small angle is able to achieve a large strain, at the cost of the granular packing factor.

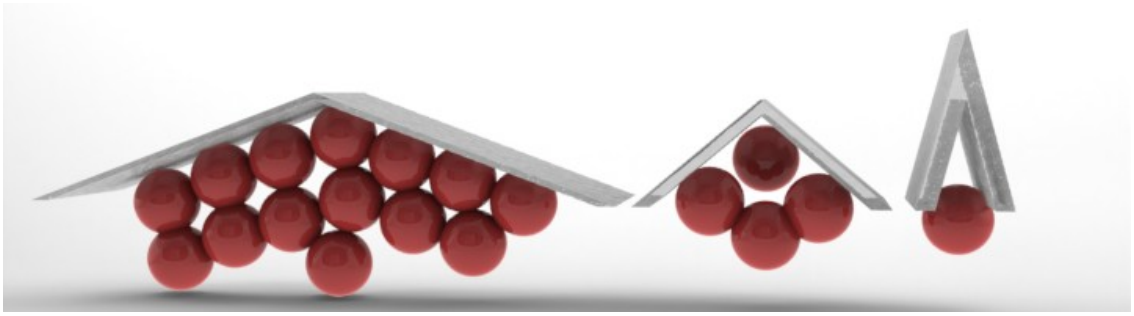

Figure 7.4: Trade-off between maximum elongation (strain) and granule packing. From left to right, the bellows angles are 20, 40, and 75 degrees.

Results from the elongation tests show that the actuator was able to achieve 30 to 35% strain, depending on the positive pressure input. Fig. 7.5 shows the relationship between input pressure, pushing force, and strain. There is a clear nonlinear profile of the actuator, given different pressures.

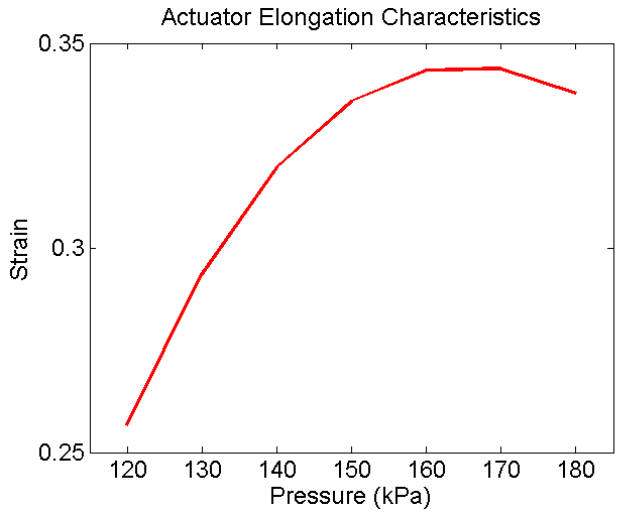

Figure 7.5: The granular jamming integrated pneumatic actuator elongation test.

7.3.2 Stiffness

From literature and Chapter 4, the shape and size of granules have an impact on the achievable stiffness range of an unjammed and jammed system. Since the investigation of an optimal granule design is outside the scope of this chapter, spherical granules were chosen for these experiments due to their "baseline" characteristics.

The packing factor of the granules also plays a significant role in the stiffness range [44]. Thus, the distribution of granules should be kept at an optimal level. As previously discussed, the elongation method of actuation and bellows angle help maintain the packing factor equal throughout the length of the actuator.

Fig. 7.6 shows the stiffness characteristics of a single jamming integrated actuator set at different vacuum pressure levels. For this actuator, the stiffness between the 20 kPa vacuum level and 55 kPa level were negligible, with peak forces of 0.51 and 0.50 N, respectively. However, there was a 65% improvement over the non-vacuumed state. The 101 kPa unjammed actuator only showed a 0.31 N force at the 20 mm deflection point.

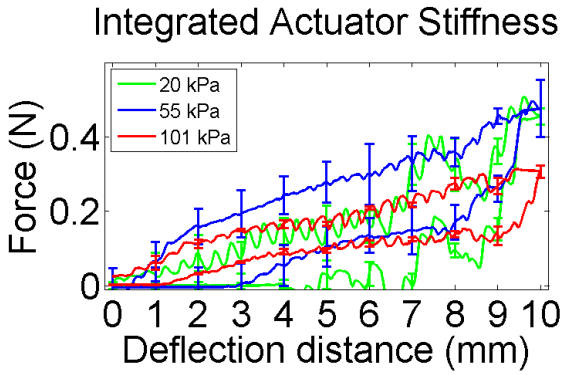

Figure 7.6: The granular jamming integrated pneumatic actuator stiffness test.

The normalized hysteresis values ($\frac{Area_{loading} - Area_{unloading}}{Area_{loading}}$) for the 20, 55, and 101 kPa pressures were 0.712, 0.68, and 0.61, respectively. The average variabilities of the load

and unloading trials were found to be 0.03, 0.06, and 0.01, respectively. Thus, the effect of jamming not only impairs the actuator from returning to its original posture, but does so differently between trials. This suggests a closed-loop controller should be used to compensate for the hysteresis and variability of the stiffened actuator.

7.3.3 Bending

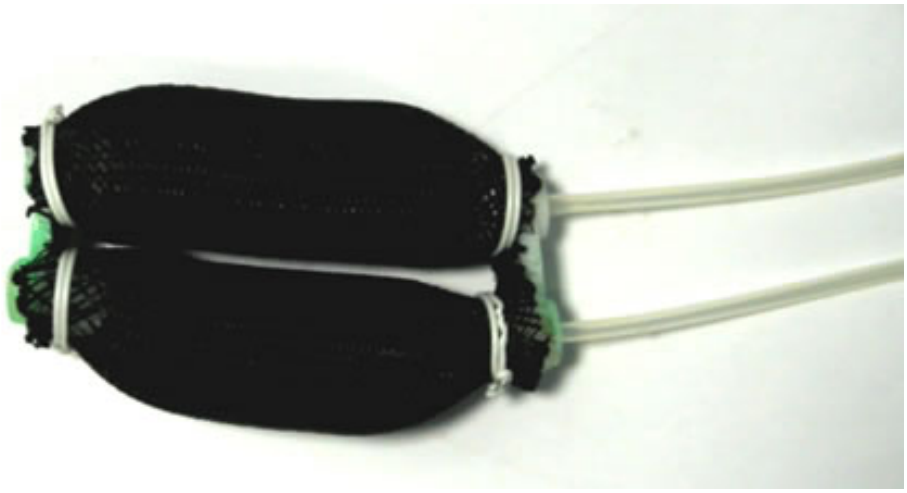

Figure 7.7: Bending can be achieved by joining multiple integrated actuators in parallel and stiffening or inflating alternating ones.

As this actuator is designed for a snake-like robot, multiple jamming integrated actuators can be placed in parallel, as shown in Fig. 7.7, to perform various bending profiles. The goal is to characterize, from modulating the pressure difference between elongated and stiffened jamming integrated actuators, the achievable bending angles and curvatures.

Traditional bending actuators and manipulators have the bending angle and curvature coupled. Curvature κ is equal to the inverse of the radius of a fitted circle, meaning a small and large radius are large and small curvatures, respectively. When increasing a bending angle, a typical actuator's curvature is also increased. This limits the actuator to a workspace with a radius smaller than the length of the bending mechanism. Thus, this

study investigates the possibility for an elongating, variable stiffness bundle of actuators to decouple the bending angle with curvature to increase the workspace area.

Combining the elongation and stiffening tests, bending tests were performed on a set of two parallel jamming integrated actuators. One actuator is elongated with positive pressure, while the other is stiffened with vacuum pressure.

7.3.3.1 Bending Angle

In developing the jamming integrated actuator system, we anticipated that the larger the pressure differential between the two parallel JIAs the greater the deflection angle. For example, the "weakest" case should occur when actuator 1 is at a low pressure and actuator 2 is unstiffened. The bending angle should be low, as actuator 1 is imposing the minimum strain, as shown from Fig. 7.5. A moderate case occurs when either a medium pressure is set for actuator 1 or a medium vacuum is pulled for actuator 2. In this case, actuator 1 either elongates further and bends the system more or the actuator 2 resists the elongation and causes the actuator to bend more. The "best" case is expected to be a high pressure for actuator 1 and a full vacuum for actuator 2, in which case the counteracting forces will curl the actuator the most.

Fig. 7.8 shows that this is not the case. In fact, the bending angle tends to be higher at the extreme ends of the spectrum. Thus, there is a region where the relationship between the pressure differential causes a smaller bending angle than when only one of the actuators are activated. Indeed, while the "best" case was found to be when actuator 1 was at 35 PSI and actuator 2 was at 3 PSI, the "weakest" case occurred when actuator 1 was at 30 PSI and actuator 2 was at 10 PSI.

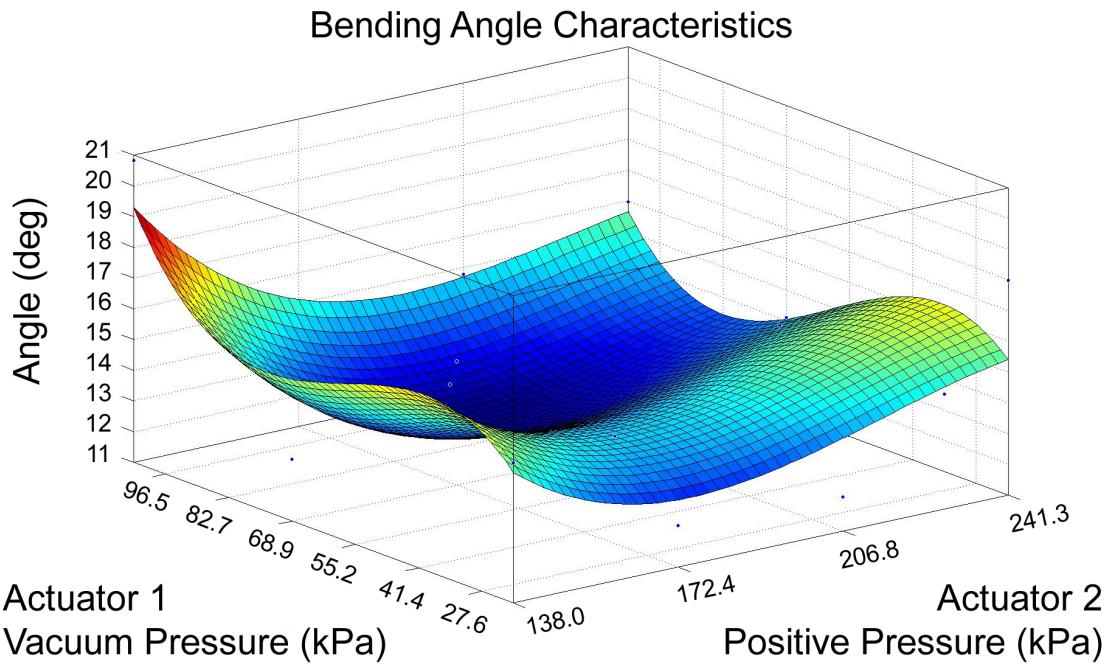

Figure 7.8: Bending angles given different combinations of positive and vacuum pressures

7.3.3.2 Curvature

To further analyze the bending of the two-actuator system, the curvatures were measured at different pressure differentials between the two actuators.

From the image, an edge detection algorithm is run to create a dataset of points along the outer edge of the system. Then, a best fit circle is overlaid on top of the detected points, as shown in Fig. 8.4. Curvature κ is then found as the inverse of the radius of the fitted circle.

The results, shown in Fig. 7.9, show that there is an trend of increasing curvature as the pressure differential between the two actuators is decreased. The highest curvature, or the bend with the tightest radius, occurred when actuator 1 was at 25 PSI and actuator 2 was at 15 PSI. The lowest curvature, or the widest radius, occurred when actuator 1 was

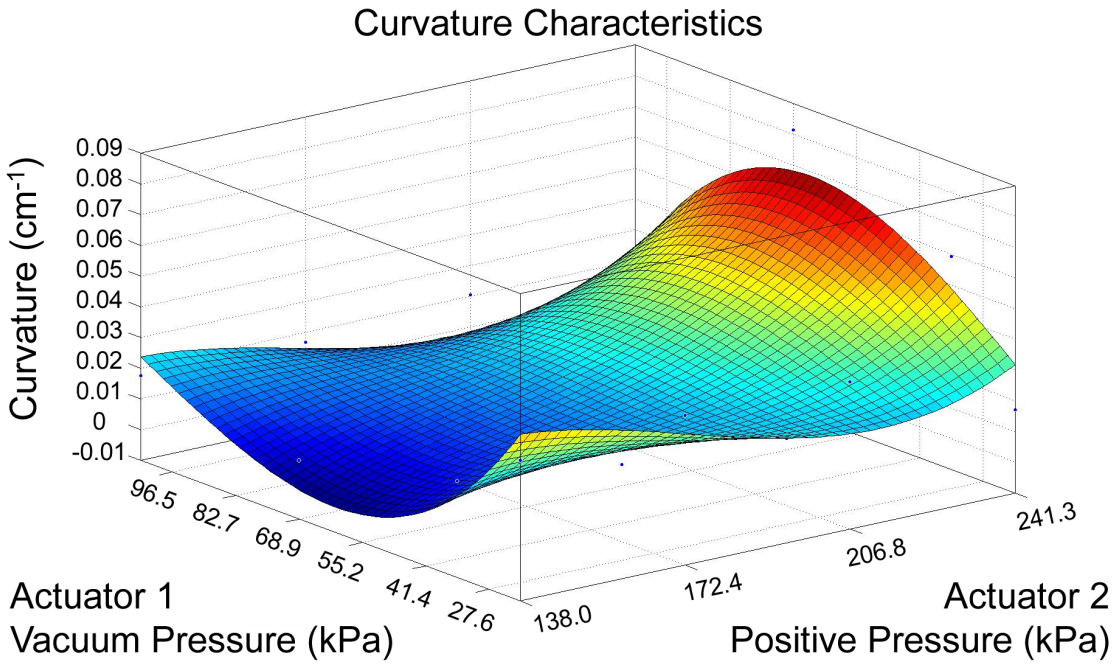

Figure 7.9: Curvatures given different combinations of positive and vacuum pressures

at 30 PSI and actuator 2 was at 3 PSI.

It should be noted that while Figs. 7.8 and 7.9 appear very different, they arise from the same set of data. This is due to the fact that two bends may have the same bending angle, but different curvatures. Fig. 7.10 illustrates this.

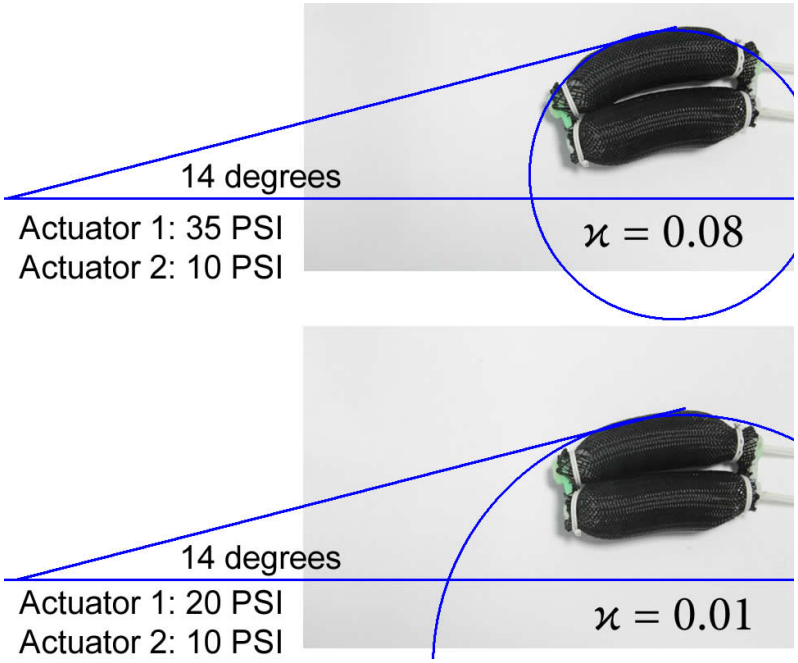

Figure 7.10: Demonstration of two JIA-E bundle profiles which exhibit the same bending angle, but different curvatures.

7.3.4 Discussion

This chapter introduced a new lightweight, impedance-controllable, variable bending pneumatic actuator design: the granular jamming integrated actuator (JIA).

The analysis showed that, in some cases, different levels of curvature have the same bending angle, as shown in Fig. 7.10. Thus, a controller can be developed to actuate the jamming integrated actuator bundle to a desired angle and curvature. Visual servoing is the key to controlling the bending profile of a JIA bundle. Fig. 8.2 outlines the controller, which takes the desired bundle bending profile, generates the positive and vacuum pressure levels for individual JIAs, and uses image processing to correct error from hysteresis and variability.

The bending angle and curvature trends were not expected, further solidifying the need to use visual servoing to compensate for the elongating and stiffening actuators. For the

bending angle, we expected the smallest bending angle to occur when the pressure difference between two actuators was smallest, and correlating positively with an increasing pressure difference. However, not only did the smallest pressure difference exhibit the largest bending angle, but there was a local minimum in the middle pressure gap (Fig. 7.8). One possible explanation is that as the pressure within the elongating actuator increases, the more it begins to straighten, due to the braided fiber sleeve. In other words, at low positive pressures, the elongating actuator is more willing to bend. At the same time, the stiffer the other actuator becomes, the more resistance to bending it exhibits. These two opposing forces then exhibit the smallest bending angle at mid-vacuum and mid-inflation pressure.

Similarly, we expected the curvature to increase given a larger pressure difference between two neighboring actuators. Instead, we found that the curvature can decrease even when the two actuators are set to a larger pressure differential (Fig. 7.9).

However, the results do show that different pressure relationships between two parallel actuators can achieve a variety of curvatures and bending angles. This 3d calibration surface can aid the actuator controller to quickly set the required pressure for a given desired bending profile. With the aid of a real-time visual servoing feedback loop, the actuator will increase its performance and stability.

During the initial design and prototyping process, stiffness observed was negatively affected when the granules exhibited a nonuniform distribution. Depending on the orientation of the actuator, the expansion of the volume causes the granules to gather at one end of the membrane. With the current design, the bellows, each at an angle of 40 degrees, tend to hold an evenly distributed granules. However, this limits the actuator to a maximum of 40% strain. An actuator with 75 degree bellows could achieve 400% strain. Further investigations on reducing granule sizes to fill the gaps should be performed.

Though, the usage of a larger quantity of smaller particles can increase the weight of the actuator, as well.

Chapter 8

Stiffness and Adaptive Control

Abstract

This chapter first describes a method to control the stiffness of a joint comprised of multiple granular jamming chambers. Thus, a desired stiffness of a joint can be mapped to the individual stiffnesses of each parallel chamber. Then the chapter describes the use of visual servoing to control the actuation of the robot. The last section describes a model-free method of controlling the impedance of a manipulator to dynamically maintain grip on an object. These control schemes compensate for the variability in the system, whether known or predicted on the fly.

8.1 Introduction

Active mechanisms have a large potential to become effective devices in robotics, but can only be as good as the control schemes implemented. Thus, this chapter describes several methods of control to properly operate the stiffness, actuation, and impedance of a granular jamming robot. For stiffness and actuation, focus is given on controlling a JIA bundle, as described in Chapter 7. For impedance, focus is given on controlling a robotic hand, where implementation can be applied to the Granular Jamming Assemblable Hand, as described in Chapter 9.

8.2 Stiffness Control

To control the stiffness of the flexible manipulator, each element at the joints will have a controlled stiffness k_{local}, which, when added together, make up the global stiffness K_{global} at that joint. This is for the multiple column design in Fig. 7.2.

$$K_{global} = \sum T k_{local} \tag{8.1}$$

which can be expanded to

$$\begin{pmatrix} K_{globalx} \\ K_{globaly} \\ K_{globalz} \end{pmatrix} = \sum_{i=1}^{N} \begin{bmatrix} \cos\theta_i & -\sin\theta_i & R\sin\theta_i \\ \sin\theta_i & \cos\theta_i & R\cos\theta_i \\ 0 & 0 & 1 \end{bmatrix} \begin{pmatrix} k_{localx} \\ k_{localy} \\ k_{localz} \end{pmatrix} \tag{8.2}$$

and

$$\begin{pmatrix} k_{localx} \\ k_{localy} \\ k_{localz} \end{pmatrix} = \begin{pmatrix} \frac{3E_iI}{L^3} \\ \frac{3E_iI}{L^3} \\ \frac{AE_{ti}}{L} \end{pmatrix} \tag{8.3}$$

N is the number of elements, θ_i is the position of an element defined by $(\frac{2\pi}{N})i$, k is the stiffness, R is the distance from the manipulator center to element center, E is the Young's modulus of an element, I is the area moment of inertia of an element, and A is the cross sectional area of an element.

To re-map a desired stiffness for the entire manipulator, there exists a solution where each element can exhibit the same stiffness. This allows for the use of just one motor pump to control the stiffness of the entire joint. The local k values for a desired $K_{desired}$ is

$$k_{guess} = (\sum T^{-1})K_{desired} + \sigma \tag{8.4}$$

where T is the transformation matrix and σ is a random variance.

In case $\sigma > 0$, as in a variance within the elements, Eqn. (8.4) can be iterated.

First, a global stiffness matrix K_{out} derived from the initial local guesses is initialized.

$$K_{out} = \sum_{i=1}^{N} T k_{guess} \tag{8.5}$$

Then, K_{out} is updated to match $K_{desired}$.

$$K_{out(n+1)} = (K_{out(n)} + \eta(K_{desired} - K_{out(n)})) \tag{8.6}$$

where η is the step size.

Finally, the new local stiffnesses k_{local} are derived from the updated K_{out}.

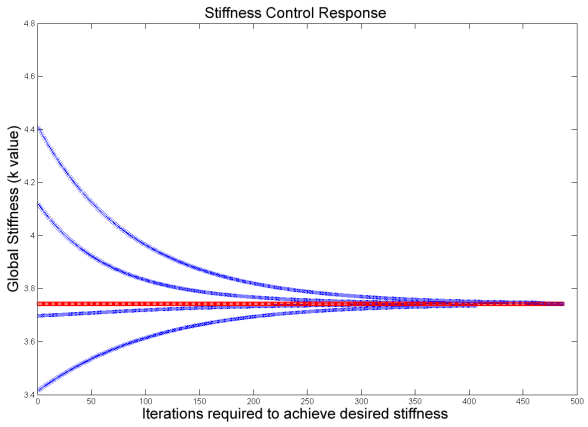

Figure 8.1: Within 400 iterations, the control scheme can compensate for a variance σ of 0.25. The red line is the desired stiffness, and the blue lines are different trials initiating from some point within the variance.

$$k_{local} = (\sum T^{-1})K_{out} \tag{8.7}$$

The new k_{local} matrix can be fed back into the actuation elements to compensate for random variances they may exhibit or experience.

In Fig. 8.1, it can be seen that the desired stiffness can be achieved after a few hundred iterations, which can be computed quickly, 1-2 seconds in MatLab on a 1.66 GHz Intel Core 2 Duo laptop with 4 GB of ram. While it is not real time, the stiffening aspect of the manipulator currently does not require operation in real time. A leeway of a few seconds for the device to rigidify is acceptable. It should be noted that this control scheme requires feedback on the current stiffness of the element. While not previously mentioned in this chapter, future work is to implement sensors in each element to measure its stiffness. A small pressure sensor or strain gage could serve to close the loop in the control.

8.3 Visual Servoing

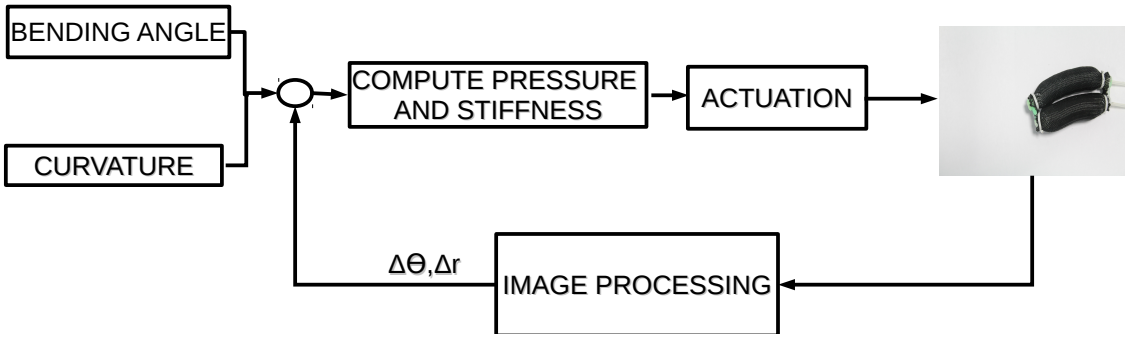

Figure 8.2: Visual servoing loop for an actuator bundle, courtesy Angela Faragasso.

In the case of actuating the manipulator, visual servoing can be used as a feedback mechanism to ensure the desired curvature and bending angle is reached. Visual servoing, or vision-based robot control, is a technique which uses image processing as a control law to reduce the error between detected features and desired features. In this case, the edge of the JIA-E, as described in Section 7.3, has a desired bending and curvature. Fig. 8.2 shows a block diagram of the control loop. An image of the actuator is captured and analyzed for its position; if there is an error between the current position and desired position, a signal is sent to the actuator to correct its position. The process repeats until the error is minimized and the desired position–bending angle and curvature–is reached. For the image processing phase, a data set of images containing the combination of four different values of vacuum and four pressures for elongation was taken, as shown in the curvature experiments in Figs. 7.8 and 7.9. The bending angle was computed using the Hough Transform to find the lines at the edges of the actuator bundle, obtained through the Canny edge detection algorithm, as seen in Fig. 8.3. This is the angle between an horizontal line at the bottom of the image and the line that best approximates the bend

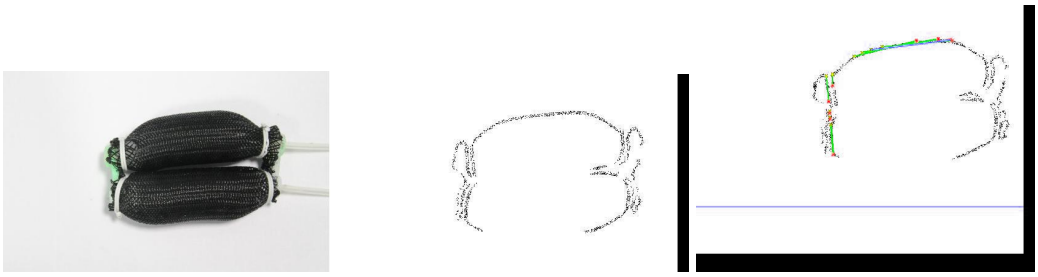

Figure 8.3: Image analysis for visual servoing. Top: Original image. Middle: Edge detection. Bottom: Hough transform

of the module. Fig. 8.3 shows this line as the blue line at the top of the image. As we expected, the bending angle increases when one of the actuators is stiffer or inflated, and tends to zero in the unactuated state.

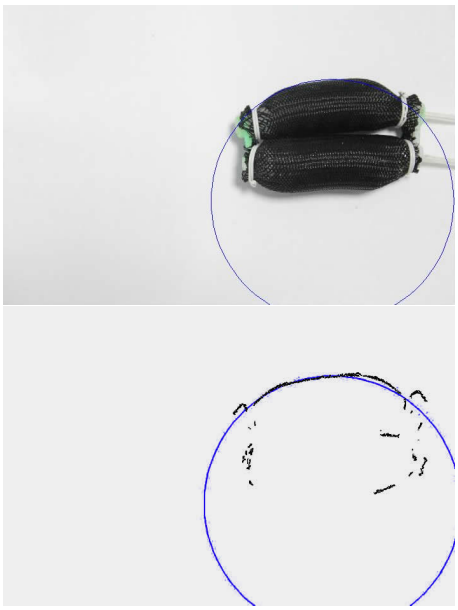

Figure 8.4: Usage of image processing to calculate the curvature of two parallel JIA-Es. Top: Best fit circle overlaid on the original image. Bottom: Best fit circle passing through detected edge.

To further analyze the bending profile of the actuator bundle, we computed the circle that best approximates the sensor's curvature. The radius and the center of the circle

were computed using the points on the edges of the image for the external border of the elongating actuator, seen in Fig. 8.4.

This section was done in collaboration with PhD student Angela Faragasso.

8.4 Adaptive Control

The theory of impedance control [65] - [67] suggests that in order to achieve a stable dynamic coupling between a body and a dynamic environment; the body should be able to adapt its internal impedance parameters (stiffness, damping, and inertia gains) imposed on the perceived error of manipulation. A number of applications can be named as examples of this appreciation such as robotic excavation [68], safe interaction with human companions [69], rehabilitation [70], prosthetics [71], exoskeletons [72], and biped locomotion [73]. Nevertheless, to date, one of the main challenges encountered in the field of robotics is to maintain the performance of impedance controllers in an uncertain environment [74], [75].

For grasping uncertain objects, wherein the target object's attributes are not well known, several groups use visual data and feedback. [76] uses 2D and 3D imaging to determine optimal grasping locations on the target object and [77] uses vision to maintain a grasp on a deformable, uncertain object. Other groups use active sensing, with [78, 79, 80] employing tactile sensors on the fingers and [81] examining joint torques to develop a model of the uncertain object. The third approach is to use historical data or learning to develop better grasps. This approach ranges from object templates with pre-calculated optimal grasps [82] to primitives and reinforcement learning [83].

Hybrid position/force control has been established by groups such as the NASA Jet Propulsion Laboratory (JPL), where in [74], a set of stability criteria were made for a known manipulator on an uncertain environment. However, the authors agree that a

trade-off between and accuracy of control exists. Another means for stability is the estimation of impedance parameters of the environment to reconcile the internal parameters of the manipulator as proposed in disturbance observers [75] and linear estimation of environment's impedance parameters [84]. However, these methods are lacking an answer to handling the arising metastability from dynamic interaction with an uncertain environment.

The solutions to manipulation in uncertain tasks such as non-linear model tracking for flexible arms with parametric uncertainty [85] [86], sliding mode control of robotic arms in uncertain environments [87], and time varying impedance centre to adaptively change the desired impedance [88] impose a demanding computational burden on the real-time controller.

Mounting elements capable of passively responding to the uncertainty of the object is a way of partially achieving adaptive impedance control. In [89], the authors have shown that the human brain learns internal models of the environment even in the presence of random disturbances. This highlights the importance of an internal mechanism to maintain a stable dynamic link with the environment. Adaptive predictive control in the human motor system [90], show how statistical distribution of motor primitives influence the efficacy of learning different force fields [91]. In [92], a probabilistic distribution is used to determine trajectories for an initial grasp.

This section investigates the concept of using a statistical representation of the existing robot and uncertain object interaction forces only to make adaptive control decisions. While previous work in the field focus on grasping a static object, this section presents a method to maintain grasp on an actively changing object. The proposed approach pose the advantage of allowing a robotic hand to be able to maintain stable contact with an object without the need of previous knowledge regarding the properties of the object such

as surface stiffness and friction. Furthermore, this method allows the robot to effectively cope with uncertainty from the external disturbance and hand-object interaction. We propose an adaptive control law that uses the knowledge of the statistics of interaction dynamics between the robot gripper and an uncertain object to compute a probability of failure given a critical threshold of grip force. The probability of risk is used as a feedback signal to make adjustments in the grip on the soft object with an uncertain internal impedance.

8.4.1 Probabilistic expectation of failure as a feedback signal to control grip force

Manipulating an object against a visco-elastic force field like opening a lid of a bottle, turning the door knob, holding a live animal, or gripping a soap bar without slipping are burdensome-free labours for human beings but, pose a high level of complexity to robotic manipulators. In particular, the complexity escalates when dealing with impedance parameters that undergo random variations.

8.4.2 Stochastic grip control task

Fig. 8.5 shows the three tasks being investigated in this section. In Fig. 8.5 (A), the uncertain cylinder has to be pulled against a spring known stiffness $K_l = 2[N/m]$ and in Fig. 8.5 (B), it has to be rotated by $30°/sec$ against a torsion spring of known stiffness $K_\theta = 0.0025[N/rad]$ that generates a torque $K_\theta\theta$ for a given rotation θ. In Fig. 8.5 (C), the object has a variable radius via inflation of the cylinder. The soft cylinder of diameter 5cm can be compressed to increase normal force subject to a limit of $1cm$.

In the case of pulling a cylinder of diameter D against a linear spring of stiffness K_l, the tangential friction force F_t at a compression x_o and spring extension of l, should meet the

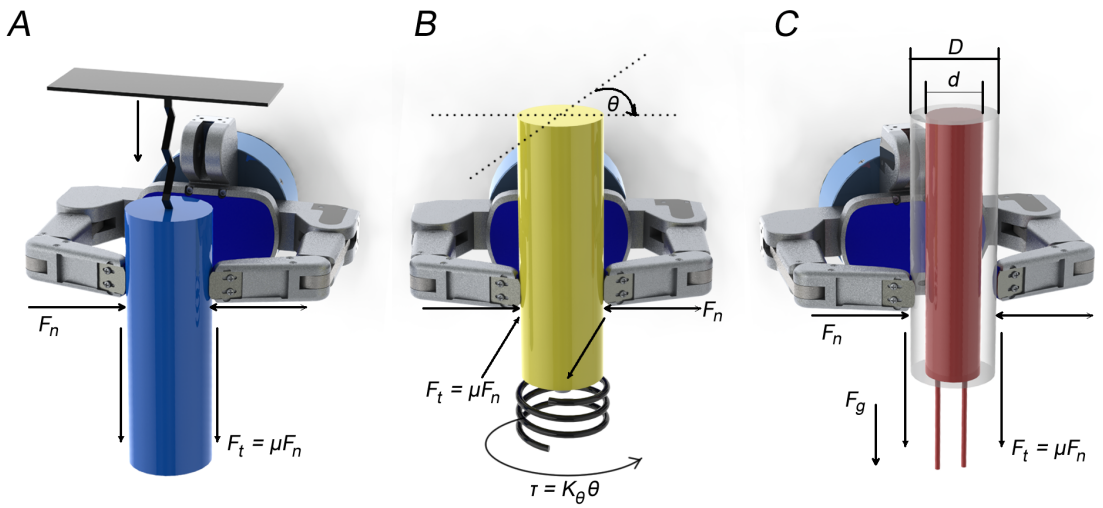

Figure 8.5: The Barrett hand gripping an uncertain in three different scenarios. A) The uncertain object is pulled against a linear sping. B) The object is rotated against a known torsional spring. C) The object is changing diameter by inflation. In all cases, we assume static friction is given by $F_t = \mu F_n$, where μ is the static coefficient of friction, F_t is the tangential force, F_n is the normal force, F_g is the force of gravity, D is the max cylinder diameter, and d is the minimum diameter.

condition given by

$$\begin{aligned} F_t &\geq K_l l \\ F_n &\geq \frac{K_l l}{\mu} \end{aligned} \tag{8.8}$$

assuming the cylinder were to be of certain internal impedance.

Under the same assumption, in the case of rotation against a spring of stiffness K_θ, the tangential friction force F_t at a compression x_o and rotation θ, should meet the condition

given by

$$\begin{aligned} F_t(D - x_o) &\geq K_\theta \theta \\ \mu F_n &\geq \frac{K_\theta \theta}{(D - x_o)} \\ F_n &\geq \frac{K_\theta \theta}{\mu(D - x_o)} \end{aligned} \tag{8.9}$$

In the variable radius case, gravity F_g is pulling the cylinder. Thus, the condition is given by

$$\begin{aligned} F_t &= F_g \\ F_n &\geq \frac{F_g}{\mu} \end{aligned} \tag{8.10}$$

Therefore, an overall environment to maintain grip is given by

$$F_n \geq F_n^* \tag{8.11}$$

where, F_n^* is the critical normal force, the minimum force required to maintain grip on an object.

8.4.3 Maintaining a stable grip using a non-compliant robot gripper

In the occurrence where the radial stiffness and damping coefficients of the cylinder are undergoing Gaussian variations, the measured normal force $F_N = N(\bar{K_o}, \sigma^2_{K_o})x_o +$

$N(\bar{C}_o, \sigma^2_{C_o})\dot{x_o}$, where $N(\cdot)$ denotes normal distribution of a random variable, $\bar{K}_o, \sigma^2_{K_o}$ are the expected value and variance of the stiffness coefficient of the soft cylinder respectively, and $\bar{C}_o, \sigma^2_{C_o}$, are those of the damping coefficient.

This implies that at any given time, the varying normal force should keep a safety margin ζ_f from the failure threshold given by

$$\zeta_f = N(\bar{K}_o, \sigma^2_{K_o})x_o + N(\bar{C}_o, \sigma^2_{C_o})\dot{x_o} - F^*_n. \tag{8.12}$$

Then the probability of failure can be found by

$$P(F_n \leq F^*_n) = \begin{cases} 0.5 - erf(\frac{\zeta_f}{\sqrt{2}\sigma_{F_n}}) & \text{if } \zeta_f > 0 \\ 0.5 + erf(\frac{-\zeta_f}{\sqrt{2}\sigma_{F_n}}) & \text{if } \zeta_f < 0 \end{cases} \tag{8.13}$$

where, the variance of the normal force $\sigma^2_{F_n}$ can be easily estimated by keeping a history of normal force measurements. Assuming the normal force F_n exhibits a Gaussian variation, the safety margin ζ_f can be defined so that $\zeta_f < \beta$. Then, it is important to understand how this β is constrained by σ_{F_n}, in order to design a controller that ensures stability of grasping despite the variability of the normal force F_n.

Let F_n be a random variable described by the Gaussian probability density function given by

$$g(F_n) = \frac{1}{\sqrt{2\pi}\sigma_{F_n}} \exp\left(-\frac{F_n^2}{2\sigma^2_{F_n}}\right) + \overline{F_n} \tag{8.14}$$

where $\overline{F_n}$ is the mean normal force.

Then, the probability of the normal force F_n falling below the safety margin of β, a distance from the critical force F^*_n, is given by

$$P\left(F_n < F^*_n + \beta\right) = \int_0^{F^*_n+\beta} g(F_n)dF_n \tag{8.15}$$

The limits of Eq. 8.15 can be re-written as given by

$$P\left(F_n < F_n^* + \beta\right) = \int_{(\frac{F_n^*+\beta}{2})-(\frac{F_n^*+\beta}{2})}^{(\frac{F_n^*+\beta}{2})+(\frac{F_n^*+\beta}{2})} g(F_n)dF_n \tag{8.16}$$

Following the mean value theorem of definite integrals of Gaussian density functions [94], there is an ϵ $(0 < \epsilon < \beta)$, so that the above integral in Eq. 8.16 can be simplified to the difference between the limits of the integral $(((\frac{F_n^*+\beta}{2}) - (\frac{F_n^*+\beta}{2})) - ((\frac{F_n^*+\beta}{2}) + (\frac{F_n^*+\beta}{2})) = F_n^* + \beta)$ multiplied by $g(\epsilon)$ as given in

$$P\left(F_n < F_n^* + \beta\right) = \frac{F_n^* + \beta}{\sqrt{2\pi}\sigma_{F_n}} g(\epsilon) \tag{8.17}$$

In order to obtain a constraint for the safety margin β in terms of the variability of the normal force σ_{F_n}, we take the derivative of the probability given in Eq. 8.17, given by

$$\begin{aligned} &\tfrac{\partial P(F_n < F_n^* + \beta)}{\partial \sigma_{F_n}} \\ &= \quad \frac{\partial}{\partial \sigma_{F_n}} \frac{F_n^* + \beta}{\sqrt{2\pi}\sigma_{F_n}} \exp\left(-\frac{\epsilon^2}{2\sigma_{F_n}^2}\right) + \overline{F_n} \\ &= \quad \frac{F_n^* + \beta}{\sqrt{2\pi}\sigma_{F_n}^2} \exp\left(-\frac{\epsilon^2}{2\sigma_{F_n}^2}\right) \Delta \end{aligned} \tag{8.18}$$

where Δ is $(\frac{\epsilon - \sigma_{F_n}^2}{\sigma_{F_n}^2})$.

According to Eq. 8.18, the probability of failure for a given safety margin β decreases when σ_{F_n} increases, only if $\frac{\partial P(F_n < F_n^* + \beta)}{\partial \sigma_{F_n}} < 0$. Since $\frac{F_n^* + \beta}{\sqrt{2\pi}\sigma_{F_n}^2} \exp\left(-\frac{\epsilon^2}{2\sigma_{F_n}^2}\right) > 0 \; \forall \beta, \epsilon$ in Eq. 8.18, this condition can be satisfied if $\Delta < 0$. This leads to the condition $\epsilon \leq \sigma_{F_n}^2$. Since $0 < \epsilon < \beta$, this condition for a stable grip can be re-written as $|\sqrt{\beta}| \leq \sigma_{F_n}$. Therefore, for a given constant value β, the estimation of failure increases with an increase in σ_{F_n}. If β is low, the probability of failure will be estimated to be low, though

the controller then runs the risk of a true failure. A higher β biases the system to increase the estimate of probability of failure, which in turn minimizes true failures. Thus, a grip control strategy that can increase σ_{F_n} will ensure a stable grip. On the right hand side of this condition, σ_{F_n} apparently increases if the object is held tightly while the impedance parameters undergo variation.

Based on the above insights, we propose that an estimate of the probability of failure in Eq. 8.17 for $\beta = 0$, can be used as a feedback signal to control the grip on the uncertain object using the grip control strategy given by

$$x_o(k+1) = x_o(k) + \eta(P\left(F_n \leq F_n^*\right) + \delta) \tag{8.19}$$

where δ is the offset used in this case to bias grip compression at high probability of failure, and η is an adaptation rate. When δ is small, tendency to grip increases, leading to an increase of σ_{F_n}. This decreases the possibility to violate the condition $|\sqrt{\beta}| \leq \sigma_{F_n}$ for stability. Therefore, in this case, we set $\delta = 0.3$, with $\delta = 0$ being neutral.

The Gaussian function on the top right hand corner of Fig. 8.6 shows how a probability of failure can be computed for a normal force F_n at any given time, given a variance for the normal force. The shape of the error function based grip control feedback signal $(0.8 - erf(\frac{\zeta_f}{\sqrt{2}\sigma_{F_n}}))$ in (8.19) is shown in the blue color curve of Fig. 8.6, where the function commands higher positive compression commands when the $(F_n^* - F_n)$ gets smaller, and reduces the grip if the probability of failure is sufficiently low. The major advantage of this approach is that it does not require the controller to know the values of the impedance parameters of the environment. Rather, a memory of past normal forces is enough to compute the variance of interaction forces.

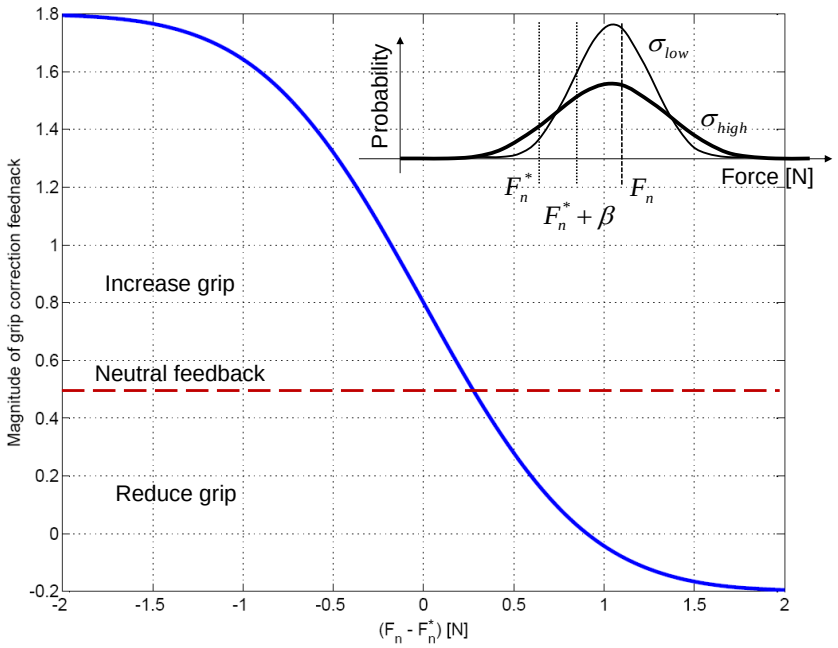

Figure 8.6: Schematic diagram of the probability of failure in a stochastic interaction. With $\delta = 0.3$, the probability of failure feedback signal is biased positively at the critical point $F_n - F_n^* = 0$. Thus, the controller would grip more. If $\delta = 0$, the probability of failure at the critical point is 0.5, which would give the controller no command to grip or relax.

8.4.4 Simulation results

8.4.4.1 Linear spring case

Simulations for pulling an uncertain cylinder against a linear spring of spring constant $K_l = 0.1N/m$ were performed on a cylinder of $R = 4cm$, $K = N(10, 1)[N/m], C = N(0.1, 0.01^2)[Ns/m]$, and $\mu = 0.6$. The learning rate of the controller $\eta = 0.0001$.

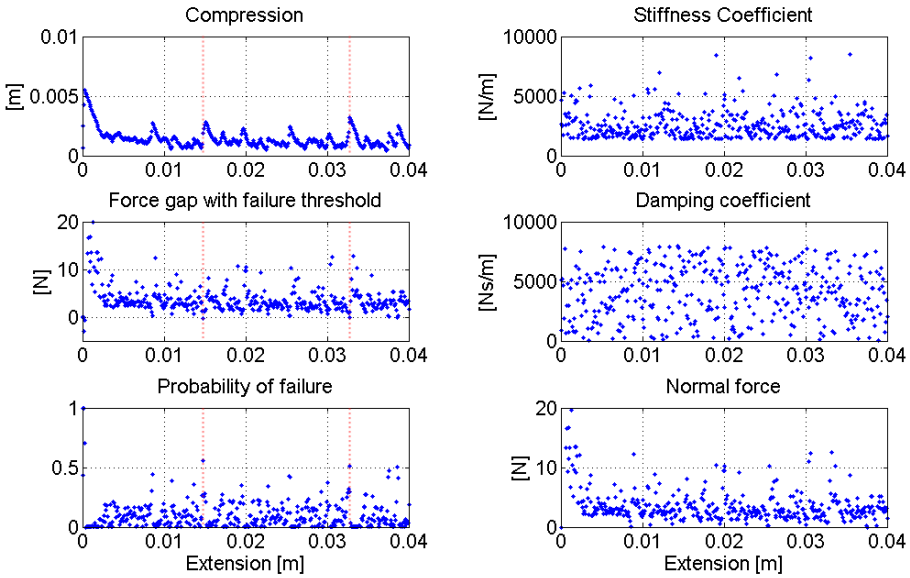

Figure 8.7: Behavior of the probabilistic adaptive grip force controller for pulling an uncertain object against a linear spring.

Fig. 8.7 shows the results of the adaptive controller for pulling an uncertain object against a linear spring.

8.4.4.2 Torsional spring case

Simulations for rotating an uncertain disc against a torsional spring of spring constant $K_\theta = 0.002N/rad$ were performed on a disc of $R = 4cm$, $P = N(25, 5/3)[Psi], W = 10N$, and $\mu = 0.6$. The learning rate of the controller $\eta = 0.0001$.

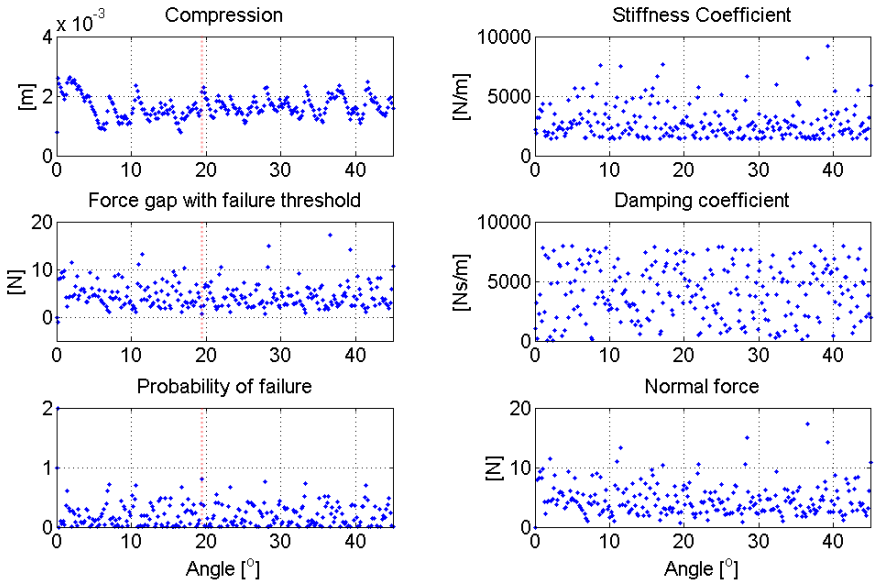

Figure 8.8: Behavior of the probabilistic adaptive grip force controller for rotating an uncertain object against a torsional spring.

Fig. 8.8 shows the corresponding results for rotating an uncertain disc against a torsional spring.

It should be noted that the randomness of the object is mapped to the stiffness and damping coefficients. Both parameters form a normal force F_n within a range of 0 and 20 Newtons for a given compression $x_o(k)$. Although the controller starts at failure due to the lack of normal force knowledge, it soon recovers and manages to maintain the probability of failure to minimum levels. It can be seen that the probability of failure approaches one at sudden extreme compression changes. However, the controller soon recovers and the probability of failure drops with that recovery maintaining it at a safe level. These simulations show that real-time adaptation is achievable with this stochastic controller, when a history of forces has been produced.

8.4.4.3 Variable diameter case

Simulations for the variable diameter case required estimates of the nonlinear behavior of the object's properties. The diameter of the cylinder is changed by regulating the pressure within it, as seen in Fig. 8.10. In order to determine the relationship between the internal exerted pressure and the impedance parameters of the tube, experimental tests were performed to map the internal pressure of the cylinder to the respective stiffness and damping coefficients. It can be observed that a change in pressure causes a more significant change to the stiffness of the tube than to the damping property. These relationships can be seen in Fig.8.10.

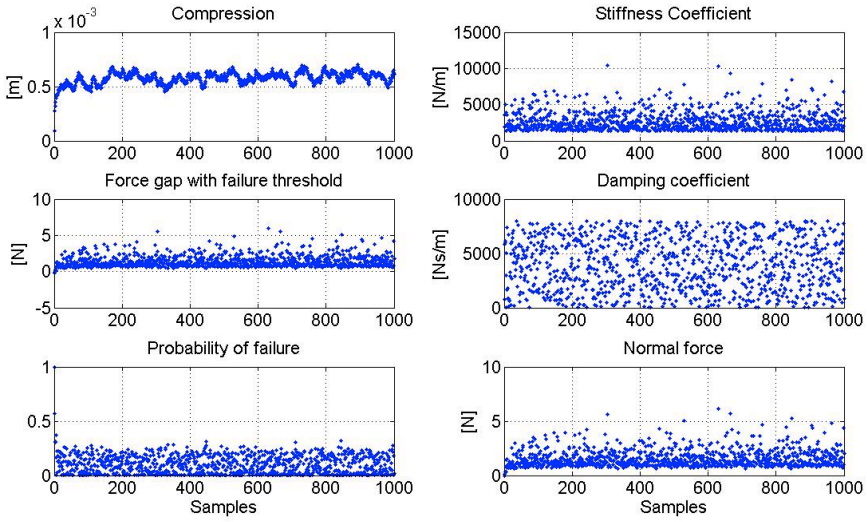

Figure 8.9: Behaviour of the probabilistic adaptive grip force controller for an uncertain object being held by a compliant gripper.

It should noted that the stiffness and damping coefficients undergo random variations, an implementation of Eq. 8.12 in internal pressure, which yield a normal force of random distribution with a mean of 2.5 N. This can be seen in Fig. 8.9. As it can be seen from the comparison of the compression graph and the force gap threshold graph, the adaptive

controller is directing the gripper to compress when the force gap increases and ease when the gap decreases; which suggests that the gripper is behaving as desired. Additionally, the probability of failure starts at high values however; as a more extensive history of the forces is created the probability of failure is kept below 0.25. These simulations suggest that theoretically, the adaptive impedance controller would allow for the correct coupling of impedance parameters of the cylinder with the compression, yielding a suitable gripper. Therefore, it can be deduced that this stochastic control law has the potential of being used for gripping without the previous knowledge of the impedance parameters of the object to be held.

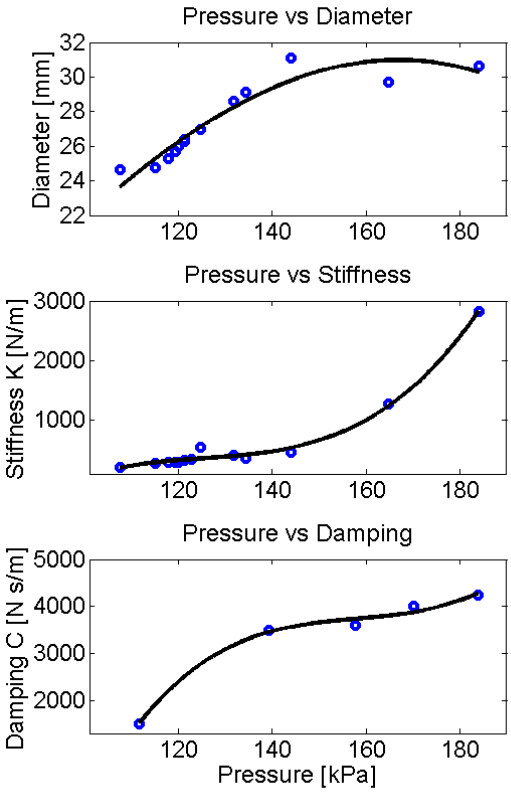

Figure 8.10: Relationships between tube pressure and radius, stiffness, and damping.

Simulations for an uncertain cylinder being gripped by a non-compliant robotic hand

were also performed on a cylinder of the same characteristics as the experimental uncertain object. Tests were performed on the tube to determine its change in diameter, stiffness, and damping when the internal pressure is increased, as seen in Fig. 8.10. For pressures in the range of 101 to 180 kPa, the tube was deflected with an externally applied force of $10.5N$. The deflection distance was recorded and used to calculate the stiffness K of the tube at a given pressure. For damping, the tube was loaded and unloaded at a velocity of 1 mm/sec, with the recorded force data used to calculate the damping coefficient C. These values were then used to mathematically model the change in the physical and impedance properties of the tube.

8.4.5 Experimental results

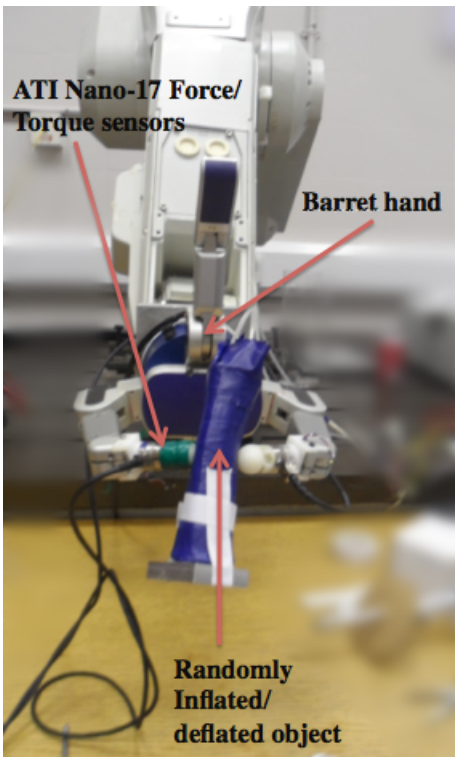

Figure 8.11: Experimental setup for the adaptive grip of an uncertain object randomly changing its diameter.

The experimental setup was taken from the variable diameter object case, in which a Labview-operated, variable stiffness tube was gripped by a ROS-operated Barrett hand with two ATI Nano17 F/T sensors attached to the fingers, as shown in Fig. 8.11. The variable stiffness tube was operated by changes in internal pressure between 101-241 kPa (absolute pressure), changing its diameter, stiffness, and damping properties in the manner seen in Fig. 8.10. A 3-way, 15 Psi Lee Valves solenoid valve was used to inflate the tube via a regulated compressed air tank and to deflate the tube by releasing the pressure to atmosphere. The duty cycle of the valve was set to a normal Gaussian distribution around 50%. The frequency of the valve duty cycle was tuned to be between 0.5 and 1 Hertz. The pressure of the tube was measured by a Honeywell 0-30 PSI absolute pressure sensor.

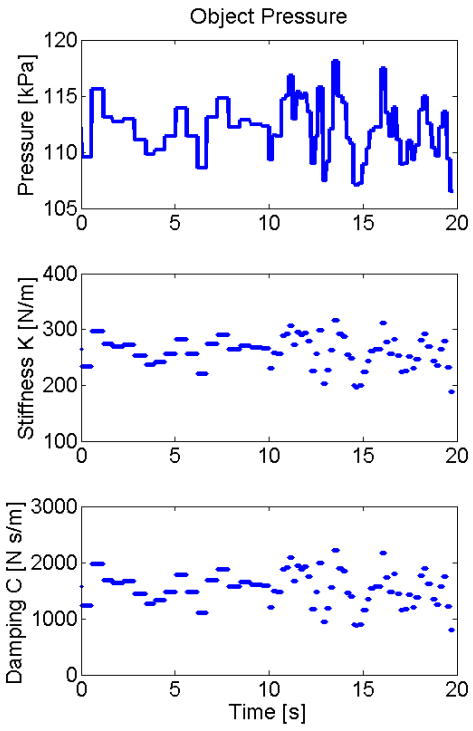

Figure 8.12: Experimental results of a the uncertain tube's pressure, stiffness, and damping properties.

The experiments consisted of two controllers: a tuned PID controller versus the statistics-based controller proposed in Eq. 8.19. The tests were run for two minutes each. Figs. 8.13, and 8.14 are snapshots of the first 20 seconds to show detail. Fig. 8.12 shows the pressure, stiffness, and damping properties of the uncertain object over the same period.

In the experiments, both controllers successfully maintained stable grip on the tube at 0.5 Hz, with a target critical force F_n^* of 2 N. Table 8.1 outlines the comparison between the two controllers at this speed. The PID was tuned to operate ideally with the tube at a 0.5 Hz frequency, while the statistics-based controller was given no prior input.

The results show that the PID controller was overgripping the tube more than the statistics-based controller, as indicated by the larger peak force. However, overall, the PID controller had a smaller mean gripping force.

At the 10 second mark, the frequency was doubled from 0.5 Hertz to 1 Hertz. This was to test the robustness of the controllers.

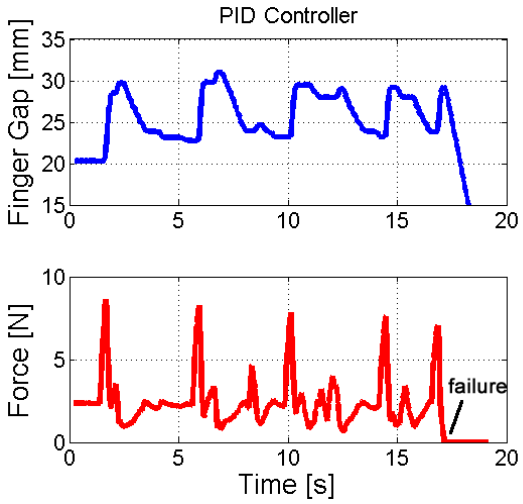

Figure 8.13: Experimental results of a tuned PID controller dropping the object when its randomly pulsating frequency changed at the 10 second mark. The drop occurs at the 17 second mark, as indicated by the zero force. The gripper then continues to close as no forces are detected. This is the first 20 seconds of a 2 minute trial, where the experiment was paused and reset after failure (drops).

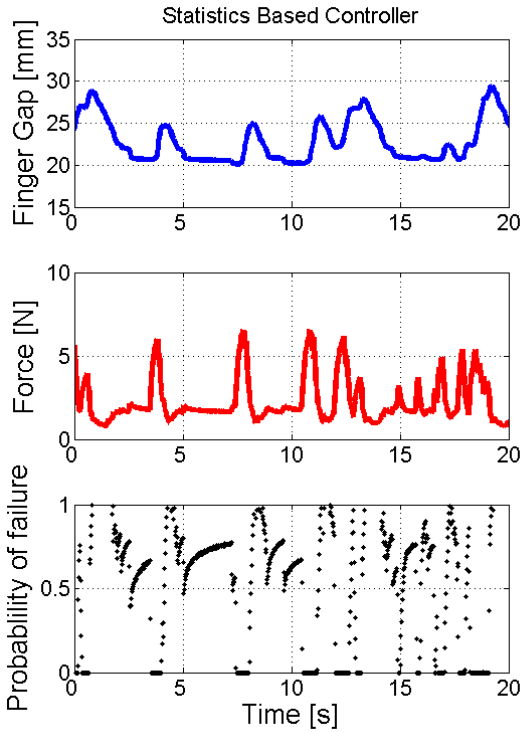

Figure 8.14: Experimental results of the statistics based controller maintaining stable grip on the object when its randomly pulsating frequency changed at the 10 second mark. This is the first 20 seconds of a 2 minute trial.

Fig. 8.13 shows the PID controller dropping the tube 7 seconds after the frequency changed. On the other hand, Fig. 8.14 shows the gripper maintaining a stable grip. The statistics-based controller was able to maintain grip for the remainder of the test. Fig. 8.15 shows a zoomed view of the experimental data. Note that the probability of failure estimate increases when there is a drop in force, and the fingers subsequently begin to close. Also note that from the 17 to 11 second mark, the fingers do not close, despite increases in force, as the probability of failure is not sufficiently high.

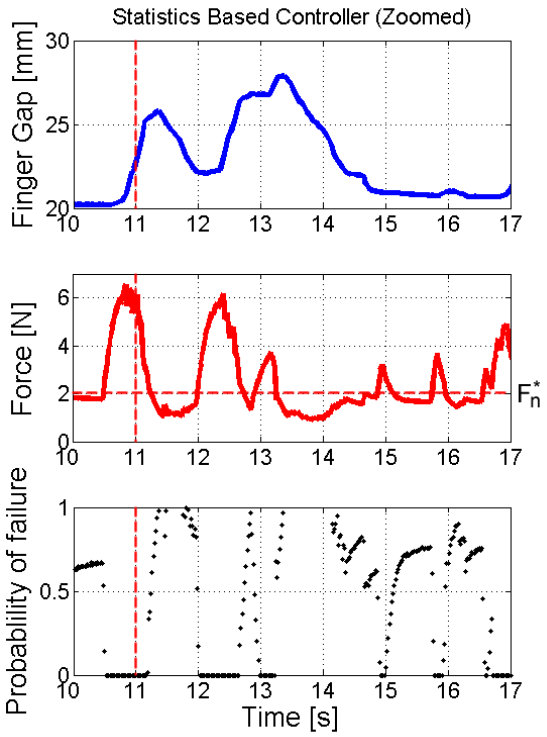

Figure 8.15: Zoomed view of the experimental results of the statistics based controller maintaining stable grip on the object. Note that at several points, the measured force drops below the critical force F_n^*, but the robot was able to recover the grip before failure.

Table 8.1: Comparison between the PID and Statistics Based Controller over the full 2 minute trial. In the case of the PID controller, the trial was paused and reset after each failure.

	PID	**SBC**
Mean force $\overline{F_n}$ (N)	2.44	2.41
Standard deviation σ_{F_n} (N)	1.44	1.18
Peak force (N)	8.61	6.98
Time to failure (s)	17	-

8.5 Discussion

Section 8.2 describes a low-level, open-loop controller to map the global desired stiffness of an actuator bundle to the individual actuators. Given different initial states and noise, the controller shows that the stiffness quickly converges to the desired value after several iterations. Given the implementation of additional sensors to provide feedback, such as a pressure sensor, this controller can be used in a closed-loop, with the feedback signal updating the k_{guess} stiffness value.

Section 8.3 continues with a description of visual servoing, and how it can be implemented with the same actuator bundle. However, rather than focusing on the stiffness of each actuator, this controller would be for the control of the shape of the robot manipulator. With desired bending angles and curvatures derived from a combination of jamming and actuation (elongation), the visual servoing controller is a high-level controller that should also be implemented with low level controllers like the previously mentioned stiffness controller.

Section 8.4 provides an in-depth analysis on a statistics-based adaptive controller. Though experiments with this controller were done with a stiff robotic hand, it can be used in the context of a granular jamming gripper. Instead of the control law adjusting the position of the hand, it can be used to adjust the stiffness or impedance of the fingers. For a snake-like robot, the statistics-based controller can be combined with the stiffness controller in Section 8.2 to dynamically adjust the stiffness of a actuator bundle.

As Fig. 8.7, 8.8, and 8.9 show, the robot must dynamically grip and relax its fingers to maintain static friction. However, the manipulator can simply maintain a large, constant amount of gripping force. For the examples shown in Fig. 8.5(C), it can be true that a constant gripping force can maintain contact with the object without slip. Namely, a high safety margin can be set if the variance σ_{F_n} from Eq. 8.18 is also high. For a pulsating

tube, a tight grip would increase the forces acting on the fingers, and thus increase the variance. Nonetheless, this type of approach is not ideal, as compliance allows the robot to handle more delicate objects. In other cases, such as case (A) (B) in Fig. 8.5, a linear change in grip force would be ill-advised, despite the linear nature of Fig. 8.7 and 8.8. The manipulator needs to actively absorb stochastic variations that may occur. For example, during the use of a hand drill, the robot would be unable to drill a straight hole if it simply increased its pushing force at a constant rate. It must utilize the stochastic information from the vibrating drill to counteract motions that would skew the forward push.

Fig. 8.7 shows the relationship between the received information of the objects stochastic properties, such as stiffness and damping, the probability to failure calculation, and subsequent compression output. From the stochastic data, a high probability of failure is calculated, as there is a large standard deviation of the stochasticity of interaction of the gripper and object. Fig. 8.6 demonstrates how a large standard deviation crosses the failure margin, whereas a small standard deviation, as depicted at 20 degrees onward in Fig. 8.7 has a very little chance of failure. Despite these variations, the compression remains very stable, because the adaptive algorithm is robust and immune to noise. Though the compression from the gripper is steady, however, the object undergoes a varied amount of forces, namely, the normal force between the object and gripper is not constant.

If the coupled dynamics are taken to account, as in Fig. 8.7, then the interaction point can be stabilized. Thus, while the gripper must vary its compression distance, a very steady level of normal force is maintained on the object. Fig. 8.14 demonstrates this effect. As the pressure level in the tube changed, the probability of failure also changed, which drove commands to the gripper to compensate. The motivation for the experimental tests relates to robot-human interaction in medical applications. When a surgical robot grasps

a lung or artery, the robot must compensate for the motion of the tissue while maintaining its force within the threshold defined by the safety margin β without over gripping the organ.

Contrasting the normal force results from Fig. 8.13 and Fig. 8.14, shows higher force peaks of 8 N for the PID control, as opposed to the force peaks of 6 N registered for the statistics based controller. These results suggest that the current position, x(k), was gripping more for the PID than for the stochastic control, as when the position changes to the next position, x(k+1), a higher force was recorded. In simple terms, these results show that the PID is more likely to over-grip the object. This situation is highly undesirable when dealing with delicate objects like organs as over-gripping would cause damage and therefore, it is also a factor to be considered when classifying a gripping manipulator as successful.

Therefore the most crucial part for the success of the gripper is maintaining its grip slightly above the critical force. The critical force depends on the magnitude of the externally imposed force, such as gravity or the pulling of the object. Thus, the critical force should be constantly updated to match the required tangential force imposed from the object as it is being pulled in an uncertain manner. This can be done by monitoring the temporal pattern of the tangential force, but this updating is beyond the scope of this section.

Uncertainty can also come from the friction coefficient itself though it is less crucial in the case of maintaining the grip at a given point as discussed in this section. However, if the gripper were to lose contact momentarily, maintaining a safe grip at the new location may be jeopardized by an inaccurate estimate of the friction dynamics. On the other hand, slip can be used to estimate the friction coefficient. Real time estimation of friction in a given contact surface is an on-going study of the authors. Dynamic modelling of fric-

tion has been extensively studied in the triobology community, and has been applied for friction compensation in systems with bearings, transmissions, hydraulic and pneumatic cylinders, valves, brakes and wheels [95]. The LuGre model can realistically describe the dynamic friction behavior in both pre-sliding and sliding regimes and has been used extensively for simulation of friction control [96].

A robotic manipulator using the adaptive grip approach would only need sensors to measure normal force, compression of the soft object, that of the gripper, and slip at contact point. However, it is fair to say that inherent noise in sensor data, unrelated to the stochasticity of the physical system, could exacerbate the challenges associated with variability of manipulation. Optimal filtering, such as with the Kalman filter, can make distinctions between sensor noise and measured variability. While there remains a possibility for sensor noise to plague the data post-filtering, compliance in a manipulator would absorb the additional randomness. Experiments will be performed in due course to confirm this proposition.

The results presented in this section open up broad opportunities for further research in the area of interacting with objects with uncertain, dynamic internal impedance and surface friction properties. This section presents a statistics-based adaptive controller which uses a stochastic control law to estimate future grip commands. Results show that, without prior tuning or information on an uncertain object, the statistics-based controller is able to maintain a stable grip on a tube of randomly changing stiffness and damping. Compared with a tuned PID controller, the statistics-based controller outperformed it in grip force and reaction time. Additionally, the statistics-based controller was able to maintain stable grip when the frequency of variation of the uncertain objects' stiffness changed, while the PID controller could not.

Future work for this controller includes learning for an optimal gripping force, as well

as learning for the critical force. This involves integrating slip detection to the controller. Other future work involve applying this controller to multiple degrees of freedom.

Chapter 9

Granular Jamming-based Robotic Prototypes

Abstract

With the introduction of the universal gripper, granular jamming as a variable stiffness mechanism for robotics is a rapidly growing field. From the studies performed on the effects of the granules, membranes, and interparticle fluid in jamming, several granular jamming-based robotic prototypes have been introduced. Specifically, this chapter introduces the Core-Snake and the Granular Jamming Assemblable Hand. These prototypes demonstrate the feasibility and range of applications granular jamming can be applied to.

9.1 Introduction

This chapter first introduces the use of granular jamming for a low-cost, variable stiffness retractor and a snake-like robot, dubbed the Core-Snake. Our previous work on the robot joints involved examining granule types [56] and actuation techniques [55] for this minimally invasive surgical tool [58, 59]. For medical robotics, a tethered flexible manipulator is not uncommon, such as with current robotic endoscopes [6], highly articulated probes [21], catheters [16], and surgical platforms [60]. In fact, most robotic surgical tools use tendons, which require a significant amount of space for the backend mechanisms [61]. However, there is an increasing favor for laparo-endoscopic single-site surgery (LESS) and natural orifice translumenal endoscopic surgery (NOTES) [5], and such large backends can cause clashing and obstructions for the surgeons [4]. The first version of the Core-Snake is a 10 mm, tethered, dry-granule, laparoscopic camera.

Lastly, this chapter introduces the Granular Jamming Assemblable Hand, a multi-fingered hand inspired by the universal gripper. The hand has two granular jamming-based fingers, which can be actuated via tendons or passive bending elements. The arm and palm, developed by partners at the Tokyo Institute of Technology, is a multi-part assembly which can be inserted through a 15 mm hole while in a disassembled state and then reassembled.

9.2 A Variable Stiffness Retractor

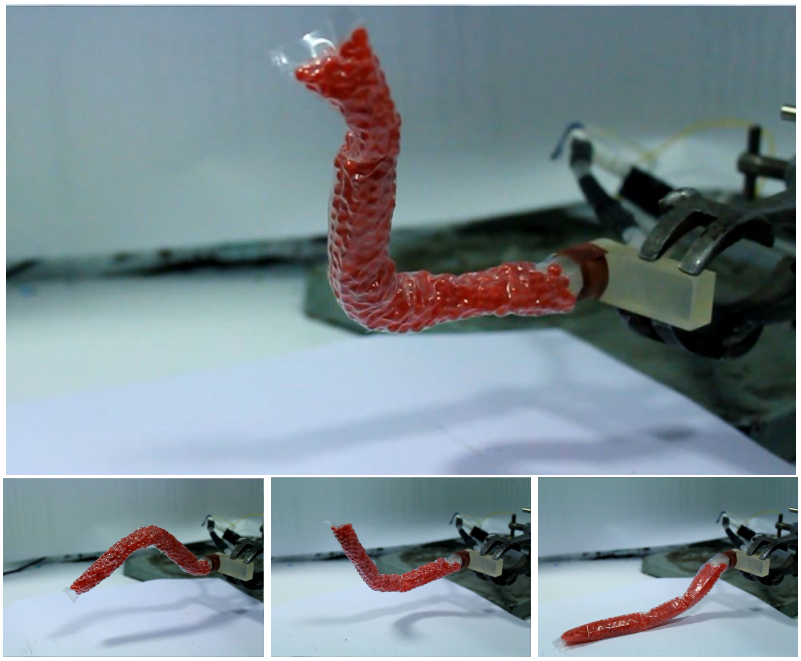

Figure 9.1: Prototype of a variable stiffness retractor stiffened in arbitrary shapes (top, bottom left, bottom center) and in an unjammed state (bottom right). 4 mm spherical granules were used with a polythene membrane.

One of the first applications for a variable stiffness mechanism like granular jamming is for retraction in surgical applications. A retractor is a "scaffold" which holds tissue in place, typically out of the surgeon's way, so that they may perform tasks without obstructions.

When it its soft state, it can be positioned in arbitrary configurations. Then, it can be locked into that shape when vacuum pressure is applied. Fig. 9.1 shows a retractor prototype, made of polythene plastic and matte-surfaced granules.

Additionally, this device can be used as a low-cost endoscope.

9.3 The Core-Snake

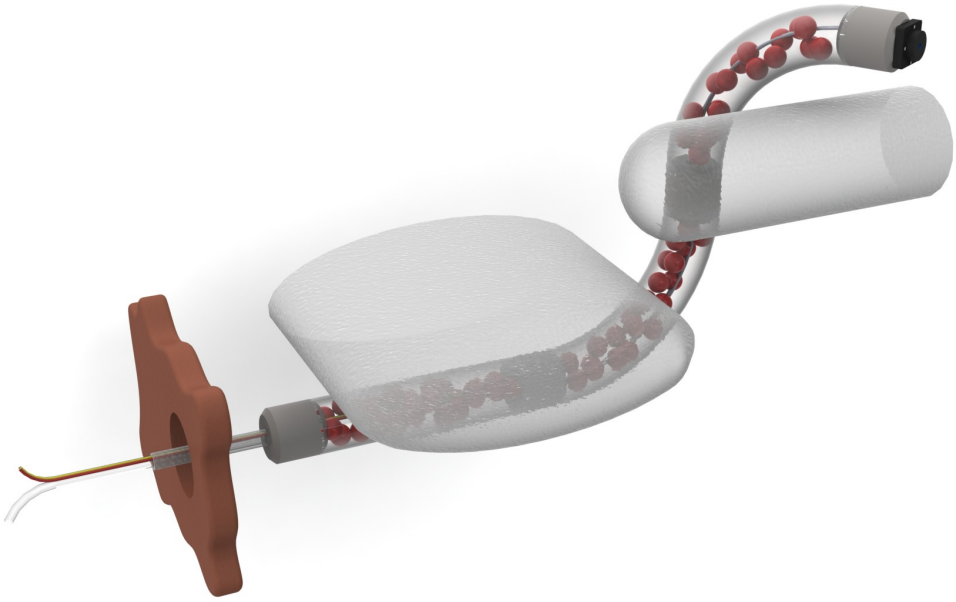

Figure 9.2: The Core-Snake, a low cost, granular jamming-based flexible laparoscopic camera. Shown here its ability to access difficult areas, while occupying 4 mm of trocar port space.

Successful and safe laparoscopic surgery is heavily dependent on its vision system, with the primary emphasis on the viewing angle and image stability [97]. Laparoscopic cameras, such as the Storz 10 mm laparoscope, are typically long, rigid tubes which have poor accessbility to target areas and require a second surgeon to operate. With a shifting enthusiam for natural orifice translumenal endoscopic surgery (NOTES), most groups prefer flexible endoscopes over the traditional rigid laparoscopes. However, these endoscopes were originally designed for intralumenal use, and tend to be application specific [97]. Thus, there is a technological and clinical need for a small, flexible camera designed for NOTES and other minimally invasive surgical procedures. It has been suggested that camera systems for NOTES also be deployable, as flexible endoscopes occupy port space,

hindering the use for additional tools [97]. These tools, like the Olympus GIF TYPE 160, can be 8.6 mm in diameter, occupying over half of a 12 mm port. Deployable camera systems such as Pillcam, are unable to provide real time control due to their wireless connectivity.

The Core-Snake aims to bridge these gaps. The Core-Snake is a 10 mm diameter robot which can alter its body stiffness from being flexible to rigid via granular jamming [64]. Most commonly seen in vacuum packed bags of rice or coffee, granular jamming is a phenomenon where a multitude of particles normally act like a fluid, but lock into a solid-like state when an external stress is applied [7, 8]. Thus, the Core-Snake is naturally compliant and can be pushed into position by the surgeon's laparoscopic tools, then it can lock its current position when a differential between the internal and external pressure is applied. In this case, the differential is induced by vacuuming the interior of the snake. This variable stiffness mechanism not only provides the surgeon with a wide viewing angle and accessibility when the snake is flexible, but also a stable vision platform when the snake is rigid [6]. Though it requires a tether for the video cables and pneumatic tubing, the cable and tube bundle is only 4 mm in diameter. The design of the robot allows the snake to be deployed into the body cavity, thus only occupying 4 mm of port space after initial insertion, a significant improvement over current endoscopes.

9.3.1 Design and materials

The Core-Snake, seen in Fig. 9.2 and 9.3, is 10 mm in diameter, composed of three, 65 mm long segments filled with 1.5 mm diameter plastic spherical granules, and followed by a 4 mm tether. The outer membrane is made with a 0.12 mm thick PVC film. The section dividers are ABS plastic and were printed with a rapid prototyping machine. The tip camera is a 10 mm diameter CMOS sensor with a 640x480 resolution at 30 frames per

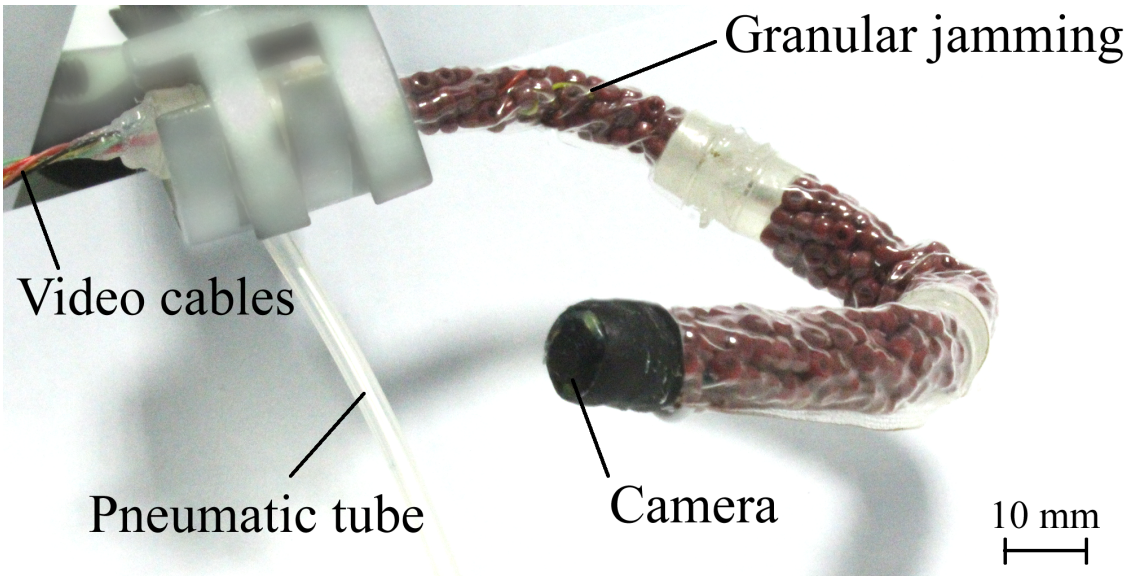

Figure 9.3: Here, jamming the Core-Snake granules locks it into its rigid state, and holding a 180 degree bend. The flexibility and variable stiffness of the camera system allows surgeons to navigate to a area of interest and lock the camera in the position.

second and was connected to a computer via USB. The tip also includes 4 white LEDs for light. The pneumatic line is a 2 mm outer diameter silicone rubber tube. Vacuum pressure is achieved with a Mastercool 90066-2V-220 pump, and measured by a Honeywell 0-30 PSI absolute pressure sensor.

To test the stiffness range of the robot, bending tests were conducted on one segment of the snake. The end of the segment was fixed, and the tip was deflected by 10 mm. The required load for this deflection was measured by an ATI Nano17 Force/Torque sensor. The force and deflection measurements were then converted to Young's modulus E for a comparison of stiffness.

External groups utilizing granular jamming, particularly for snake-like or elephant trunk-like robots have shown that ground coffee is the ideal granule type for jamming [30]. However, in medical applications, concerns for using organic materials in a laparoscopic

camera system resulted in tests to examine if there is a plastic substitute. The synthetic substitute would need to match the stiffness of ground coffee and withstand an autoclave, the most common method of disinfection.

9.3.2 Experimental results

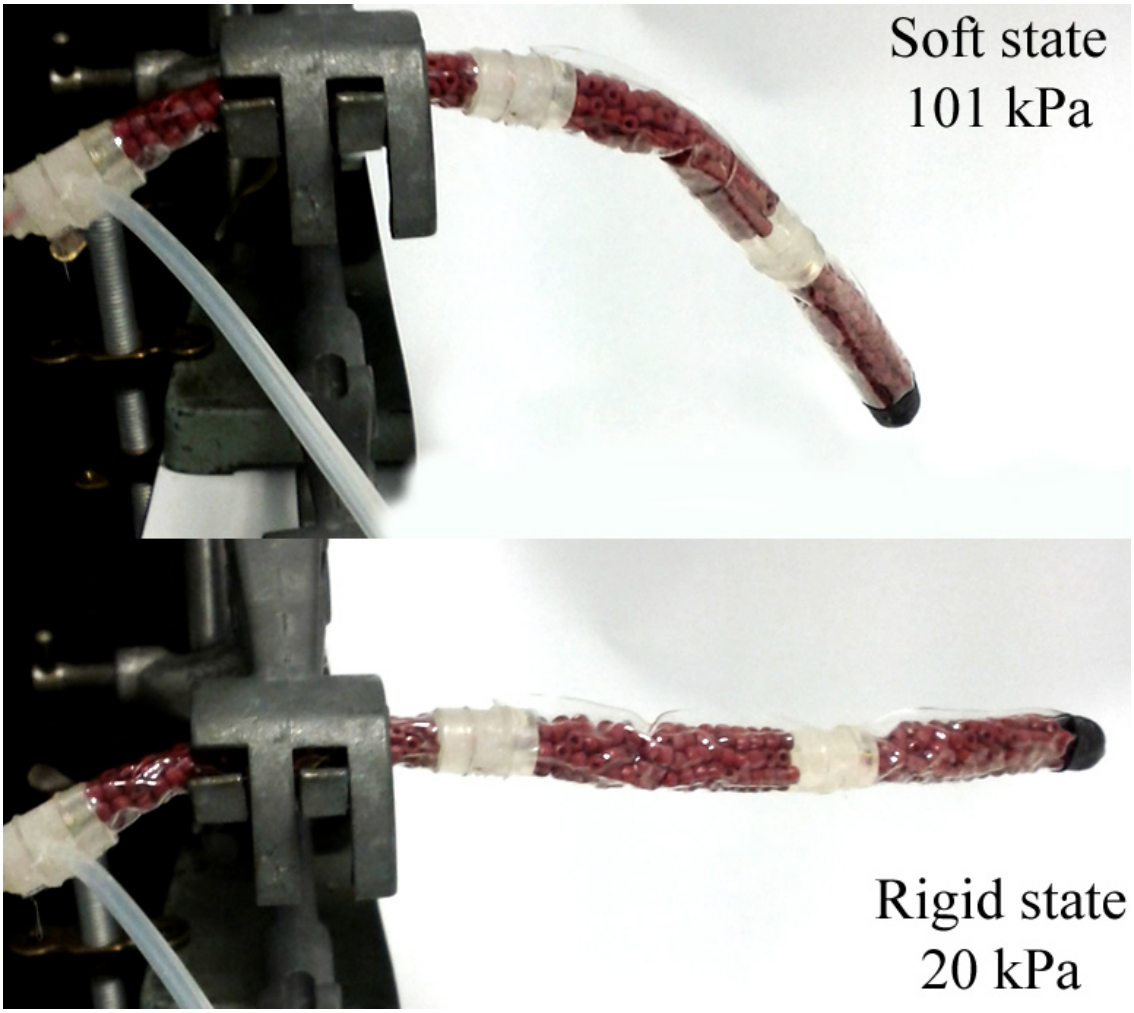

Figure 9.4: The snake bending due to weight when soft (top) vs the snake holding a horizontal position when rigid (bottom).

The bending test results show that, after deflected, one segment can exhibit 0.20 N of force at 101 kPa (soft state) and 0.42 N at 20 kPa (rigid state). The stiffness, Young's

modulus E, is calculated from the bending results by $E = (4FL^3)/(3\pi dr^4)$, where F is the loading force, L is the segment length, d is the deflection distance, and r is the segment radius. Thus, E = 3.73 and 7.83 MPa for the soft and rigid states, respectively. These preliminary results show that the Core-Snake is able to increase its stiffness by 2.1 times. Fig. 9.4 visually shows what these stiffness values represent: the varied ability to hold the Core-Snake in a horizontal position. In other words, the rigidified snake is a stable platform.

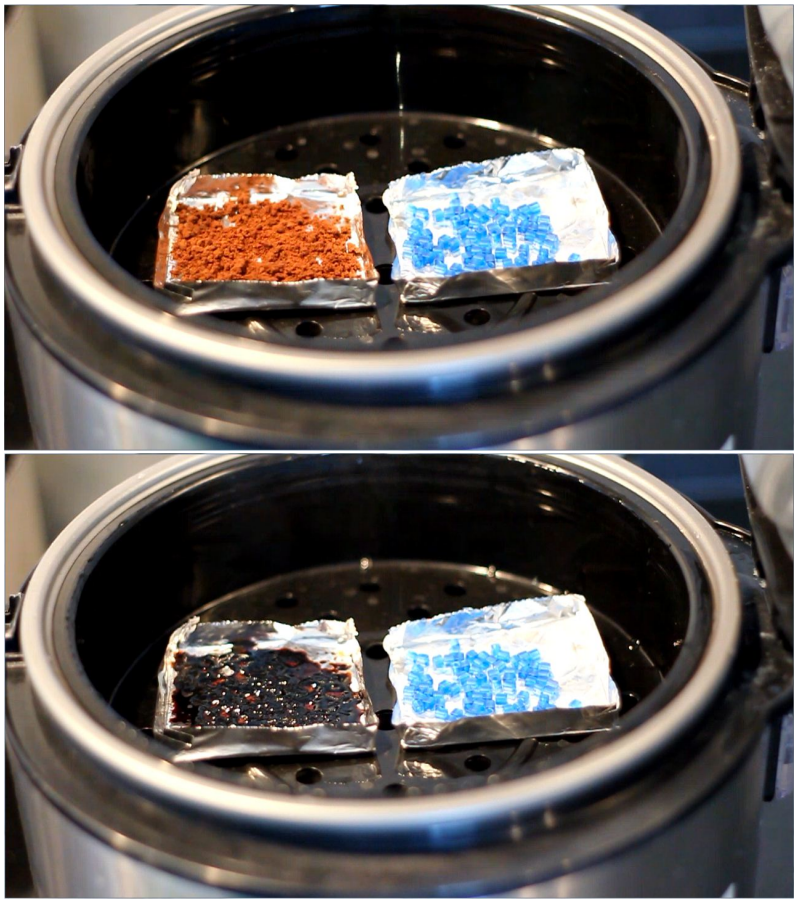

Figure 9.5: Coffee vs synthetic granules before and after steaming, simulating an autoclaving process. After steaming, the coffee granules coagulate irreversibly, whereas the synthetic granules remain intact.

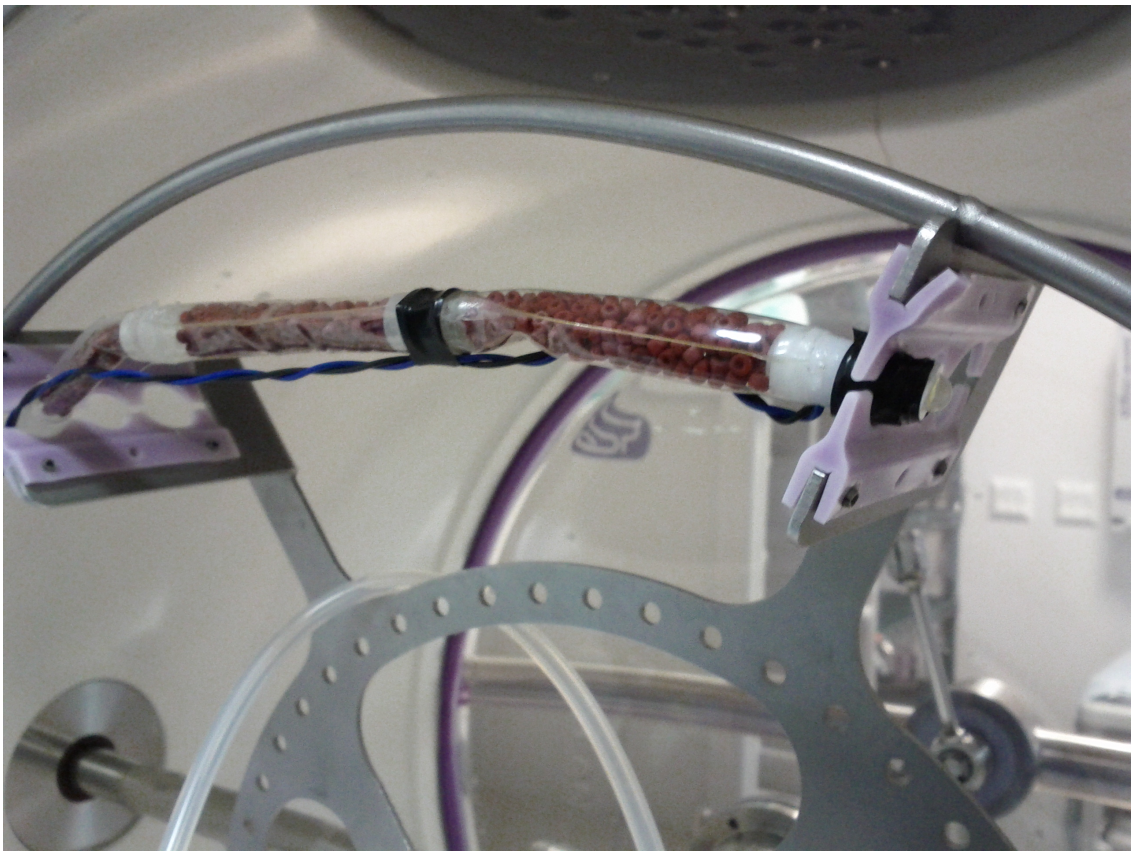

Figure 9.6: The Core-Snake inside a Labcaire Autoscope ISIS Automated Endoscope Reprocessor.

Bending tests, shown in Fig. 9.4, performed between ground coffee and plastic spheres for the rigid case showed that a synthetic substitute improved the stiffness. Unlike coffee particles, the plastic granules are able to withstand the sterilization process via steaming, shown in Fig. 9.5, both validating the use of granular jamming in a medical device and the use of synthetic granules.

9.4 The Granular Jamming Assemblable Hand

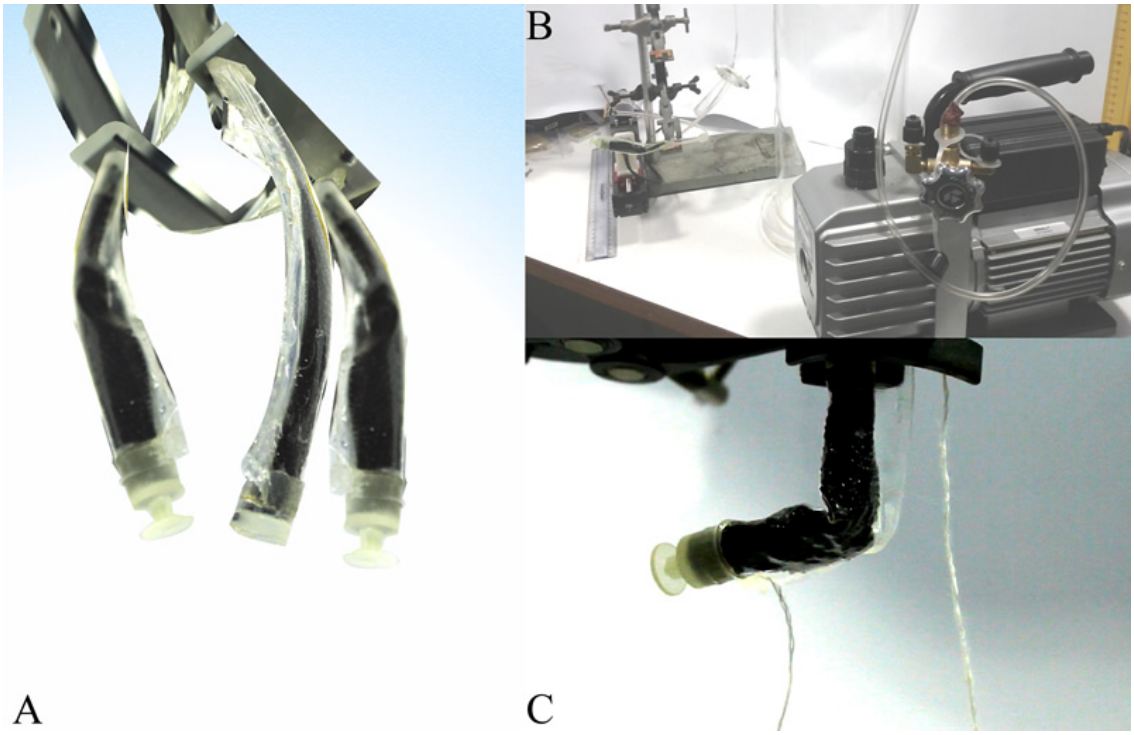

Figure 9.7: (A) The assemblable hand. (B) The backend setup. (C) A granular jammed finger stiffened at 90 degrees.

Commercial robot assisted laparoscopic devices such as the da Vinci are the current gold standard in the field of minimally invasive surgery. These robots not only significantly decrease patient recovery periods, but also overall medical costs. However, Intuitive Surgical's da Vinci and EndoWrist Graptor require multiple trocar ports and high grasping forces to prevent slippage of large organs, which can cause unnecessary trauma to the skin and target tissue [98].

To reduce the number of necessary trocar ports, and to prevent clashing of instruments in natural orifice transluminal endoscopic surgery (NOTES) and laparo-endoscopic single-site surgery (LESS), several groups have proposed the use of assemblable mechanisms, devices which can be inserted in several pieces and re-assembled within the body cavity

[99, 100]. Often for difficult operations, surgeons turn to hand-assisted laparoscopic surgery (HALS), where a large 70 mm incision is made for the surgeon's hand to be inserted. An assemblable hand is advantageous to the surgeon, as it can grasp, retract, and manipulate large internal organs as if the surgeon's own hand were inside the patient, while only requiring a single 12 mm trocar port [101]. Though there exist forceps and fan retractors, a multi-purpose tool with additional degrees of freedom simplifies the procedure.

As mentioned above, the second problem posed by conventional tools is the amount of required grasping force. To compensate for the high grasping forces used by rigid tools, this section proposes the use of a compliant, variable stiffness finger via granular jamming. The main benefit of granular jamming over other compliant systems, such as those developed by [102, 103, 104], is that a pneumatic gripper is unable to vary its impedance with an object in hand, whereas granular jamming-based grippers can.

This section proposes the use of a novel granular jamming finger to be used in an assemblable hand for minimally invasive surgery. The finger uses a pre-curved rubber liner to passively curl. When the finger has wrapped itself around an object, a vacuum is applied to jam and lock the finger into position. To release or straighten, positive pressure is added and the finger's inelastic membrane causes it to straighten. The passive gripping design prevents surgeons from grasping organs with excessive force, while the granular jamming enables the robot to maintain a stable grip at any configuration.

9.4.1 Granular jamming finger designs

9.4.1.1 Finger design: Tendon control

The first finger design is actuated by a tendon and stiffened by granular jamming, as seen in Fig. 9.8. A vinyl membrane was used to create the finger structure and was filled with

Figure 9.8: Actuator design A for the granular jamming, assemblable finger: a tendon actuated mechanism.

1.5 mm diameter round granules. The vinyl membrane material was 0.5 mm thick, which provided the finger with enough structure to passively straighten. Thus, when there was no pressure differential between the interior and exterior of the finger, it would straighten after deflected or bent. This also occurred with the finger upright, indicating that the membrane structure can also overcome the force of gravity.

To bend the finger, however, required an external load. Thus, a tendon was introduced to control the bending of the finger. Fig. 9.8 shows the tendon bending the finger at a 90 degree angle, after which vacuum pressured is applied to jam the granules, and locking the finger in place.

While functional, this design requires an additional motor and control system to operate the tendon.

9.4.1.2 Finger design: Passive bending element

Instead of a tendon-based approach, positive pressure can be introduced to actuate the finger. While typical pneumatic designs use expanding membranes and fiber braids, such as with Mckibben actuators, such designs can change the volume and shape of the internal structure, causing granules to become unevenly distributed. Thus, this design uses posi-

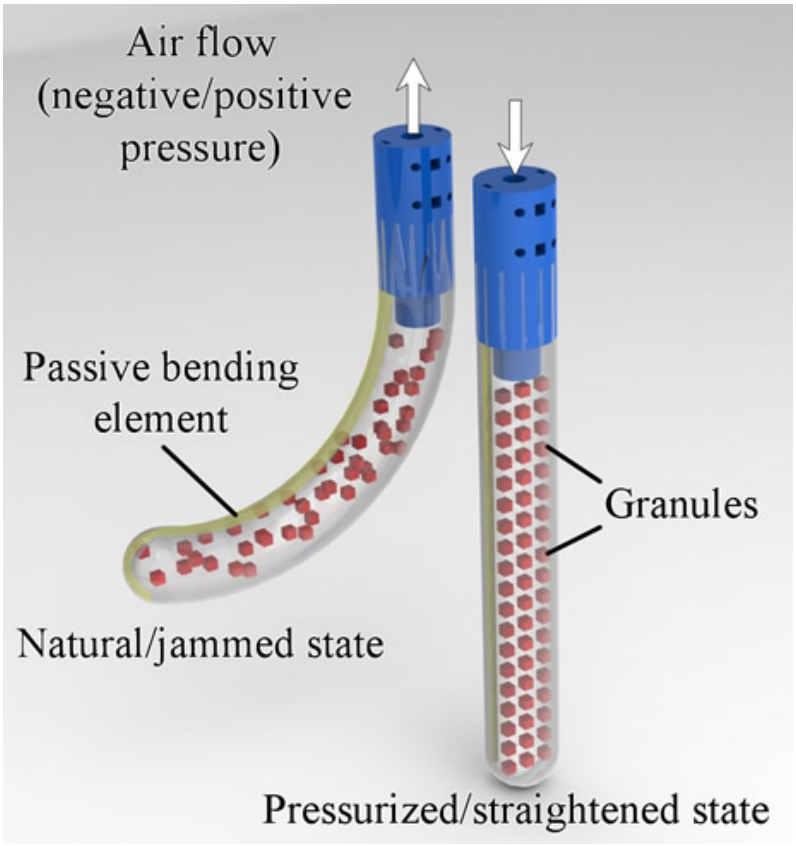

Figure 9.9: Actuator design B for the granular jamming, assemblable finger: a passive bending mechanism.

tive pressure and an inelastic membrane to straighten the finger, while a passive bending mechanism curls the finger when no pressure is applied.

The passive bending mechanism is a pre-curved, 3 mm diameter polyethylene tube, shown in Fig. 9.9, designed with a stiffness greater than the unpressurized finger but less than its pressurized/vacuumed state. A hard polyurethane rubber of Shore 70A hardness was also tested, but proved to be too weak at this scale.

Figure 9.10 shows the finger in its pre-curved, natural state and then in its pressurized, straightened state. The first prototype was able to achieve a 11 degree change in bend at 135.5 kPa (absolute pressure).

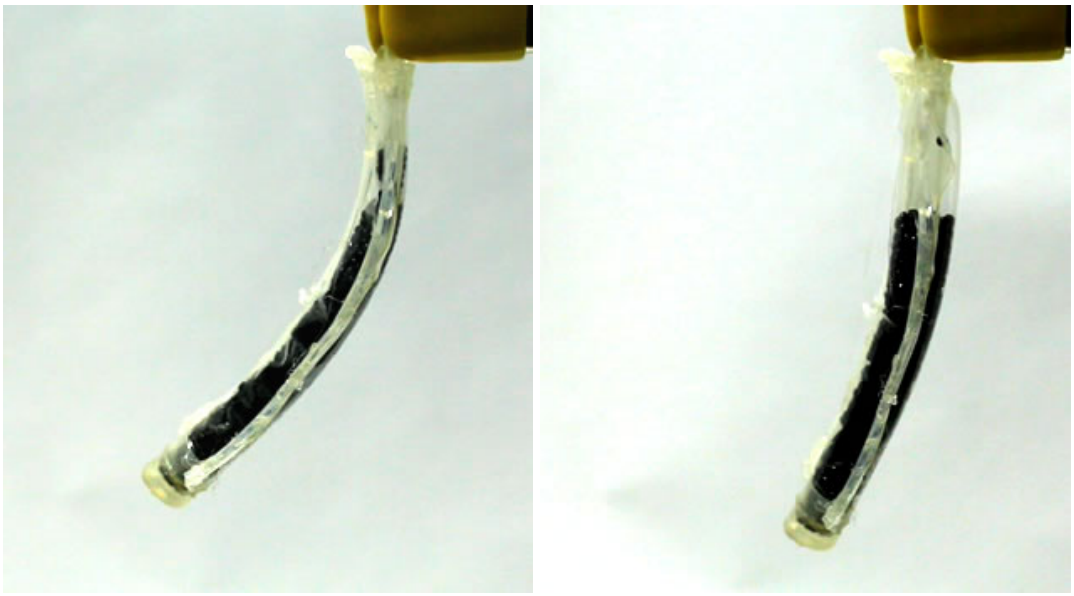

Figure 9.10: Actuator design B for the granular jamming, assemblable finger: a passive bending mechanism. Left: The unpressurized, curved state defined by a passive bending element. Right: The straightened state when pressurized by 135.5 kPa (11 deg change).

9.4.2 Hand assembling

The fingers were tested in a simulated body cavity to validate their applicability to assemblable hand mechanisms. The tests show that the passive curling of the finger does not inhibit it from being inserted into a trocar port.

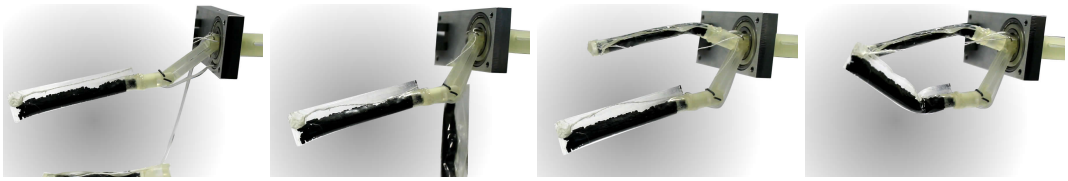

Figure 9.11: Demonstration of the assemblable hand using the tendon-based granular jamming fingers.

Figs. 9.12 and 9.13 show the cross section of the hand. The air tube that actuates the side finger passes inside the parallel link. However, the air tube that actuates the front finger

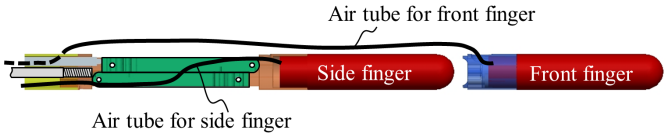

Figure 9.12: Schematic of the assemblable hand during insertion. The front finger is disconnected from the base, while the side finger is collapsed. Both fingers and base are inserted in-line, reducing the cross section to fit through a 12.5 mm diameter Trocar port.

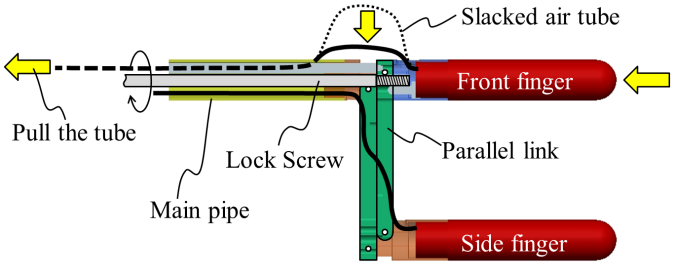

Figure 9.13: The assembled hand. The parallel links for the side finger fold the hand open, and the front finger is pulled into place. The "knuckle" joint between the hand and the front finger is designed to automatically align the front finger as it is locked onto the hand.

has slack and thus sticks out from the main pipe. Therefore, when the front finger is assembled, the slacked air tube is pulled into the main pipe. Moreover, inside the main pipe, there is a lock screw which fixes the parallel link and front finger. This design prevents the assembled hand from backlash, and it can not be disassembled unintentionally.

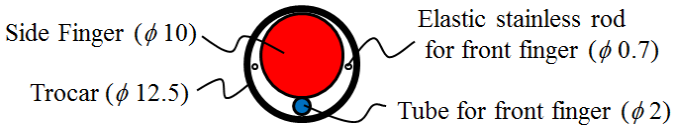

Figure 9.14: Diameters of the trocar and parts of the hand.

In this mechanism, the air tube to actuate the front finger must be connected. Therefore, when the side finger passes through the trocar, the air tube and the stainless rods must

pass at the same time. The diameter of the finger, the air tube and the stainless rods are 10 mm, 2 mm, and 0.7 mm, respectively. These dimensions allow the assembly to pass through the 12.5 mm diameter trocar port (Fig. 9.14).

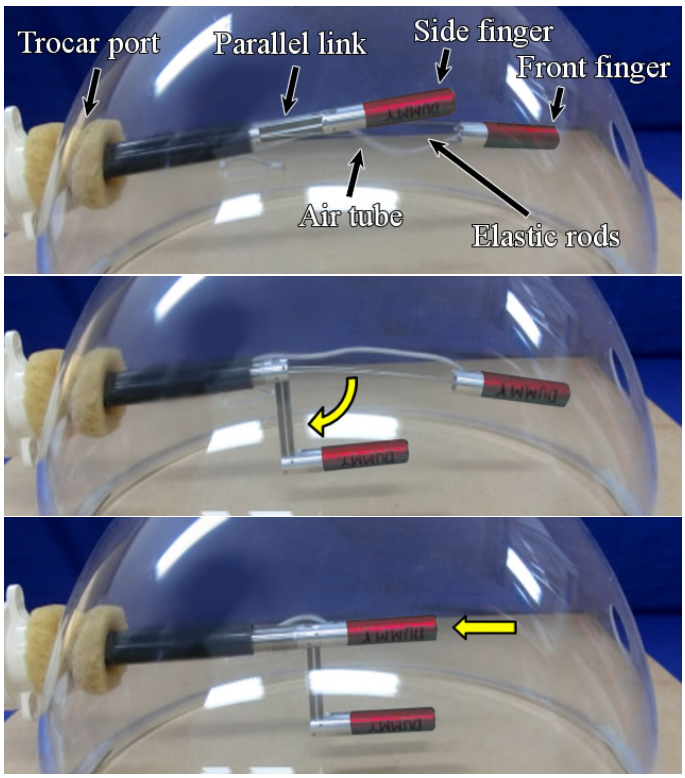

Figure 9.15: The assembling procedure. Top: Components of the assemblable hand during insertion. Middle: Unfolding of the side finger. Bottom: Locking the front finger. Courtesy of Toshio Takayama and the Omata/Takayama Lab at the Tokyo Institute of Technology.

Figure 9.15 shows the assembling procedure. First, the front finger and the side finger are inserted in series into the abdominal cavity through the trocar port. The front finger is supported by two thin elastic stainless rods to prevent it from dropping onto internal organs, further contributing to the safe design of the mechanism. Next, in step two, the side finger is unfolded by the parallel link mechanism. Finally, the stainless rods are pulled and the front finger is locked into the assembly.

The hand assembly technology was first developed by the Omata/Takayama Lab at the

Tokyo Institute of Technology. Collaboration with their lab is to use the assemblable hand as a platform for granular jamming-based fingers developed by the author.

9.5 Discussion

Granular jamming is open to many applications as a variable stiffness mechanism. As shown in Sections 9.2 and 9.3, granular jamming can be used for a medical flexible manipulator such as a retractor or laparoscope. The low-cost nature of the devices has a two-fold benefit. First, these devices raise fewer sterilization concerns, as they can be disposable, rather than reusable. Reusable endoscopes have a history of limited sterilizability, particularly in small mechanisms and electronic components. Secondly, costs are driven down, as similar systems to the granular jamming prototypes can cost up to 50 times more. In fact, the cost of the Core-Snake is around 20 GBP, which is also low enough to offset the the overhead costs of the sterilization process in traditional laparoscopes.

Section 9.4 introduced a granular jamming hand, where the fingers have a controllable stiffness. The actuation achieved can be done similarly to the mechanisms in Chapter 7, or with a passive bending element. Though similar in aim to the universal gripper developed by Cornell and U Chicago, the assemblable hand has a few key advantages. The hand-like structure enables the assembable hand to grip objects of larger diameter, as the fingers can wrap around an object. Moreover, as each finger's stiffness can be independently operated, an adaptive impedance controller such as the one proposed in Section 8.4 can be used to dynamically maintain grip on uncertain objects. A device such as the universal gripper, which has only one controllable surface, would be unable to dynamically grip such objects.

Additionally, the assembable feature of the hand in Section 9.4 enables it to pass through

openings of diameters much smaller to its own. This feature shows that granular jamming can be readily integrated into different systems, and operate in parallel to other mechanisms.

Overall, this chapter presents novel robotic devices which benefit from granular jamming. These prototypes are initial proof-of-concepts that require additional research and development. However, the next stages for these prototypes are beyond the scope of this thesis. This includes phantom organ and animal testing in-vitro, as well as additional investigations on the sterilization process.

Chapter 10

Conclusions

Abstract

The various aspects of granular jamming investigated in this thesis were for the optimization of a variable stiffness flexible manipulator. In this context, the variable stiffness mechanism consists of three parts: the granules, membrane, and vacuum pressure. To increase the stiffness range between the granular transitions, studies were performed on the effect of the granules and membrane at varying levels of vacuum pressure. For the granules, experiments were performed on different granule shapes, sizes, and materials. For the boundary layer applying the external stress, the membrane, different materials and designs were investigated. Lastly, a study was done to evaluate the difference between air and water as the interparticle fluid in the context of the jamming transition. The experimental results show that cuboid granules and polyethe plastic at maximum vacuum gave the largest range of stiffness for a cylindrical structure.

Conclusions

The granular jamming systems and designs presented in this thesis were created to solve fundamental problems current robotics exhibit in the medical field. The variable stiffness aspect of granule jamming will enable medical professionals to utilize single ports (LESS) and natural orifices (NOTES) to lower surgery costs and increase patient recovery rates, as commercial medical robotics such as the da Vinci system have rigid arms which inhibits them from being used in LESS and NOTES. The integrated pneumatic muscles not only have a tunable strength, but can exert much more force than either micromotor or tendon driven systems can.

In Chapter 4 we were able to increase the performance of the granular system, compared to the typical configuration of a smooth rubber membrane engulfing round plastic beads, as well as adding an actuation element to the joint design. While we did not improve the overall stiffness of the granular system, we did lower the variance and attenuate the nonlinearity. We experimentally confirmed several simulation results obtained by external groups on granular jamming, including the emphasizing importance of the volume fraction and inter-particle traction.

Chapter 5 presents the characteristics of five clinically approved membrane materials for a granular jamming-based flexible robot. Latex and nitrile were found to be similar in bending and tension tests, and are "well-rounded" materials. In particular, latex not only has the least variance in E between the bending, tension, and compression tests, but also behaves distinctively between atmospheric, 55 kPa, and 10 kPa. Vinyl and vitrile tend to be quite varied between the load scenarios, working better than latex in some while worse in others. Polythene consistently achieved the highest E values for all the tests, which may be beneficial for applications focused on stiffness. However, for applications desiring a softer state or better stiffness range, latex may be better suited.

In Chapter 6 we demonstrate a novel means of regulating the stiffness of a granular jamming joint by the use of deaired water. The results show that a hydraulic granular jamming system requires 20 times less volume than a pneumatic system to achieve the same stiffness. Additionally, a hydraulic system is able to achieve a 50% lower minimum stiffness than a pneumatic one. This opens a new field in granular jamming research for robotics, as a hydraulic granular jamming system can be used for mobile and field robotics, as well as in the medical field.

In comparison to the simulation results from Chapter 3, the experimental results in Chapters 4, 5, and 6 found the achievable stiffnesses of the systems to be lower than expected. Though the simulation and experimental results were on the same order of magnitude, additional work should be done to improve the model to more closely predict the stiffness of granular jamming given a set of parameters which describe the system.

Chapter 7 presents a variable stiffness pneumatic actuator, which is able to elongate or stiffen. When placed within a bundle, a set of parallel granular jamming integrated actuators can alter its bending angle and curvature independently. The ability to control both angle and curvature increases the workspace of the soft manipulator, opening new opportunities for the field of soft robotic research. With the use of a compliant, non-metallic actuator, potential applications are wide. From medical robotics in magnetic resonance environments to exploratory robots, the introduction of this controllable bending and curvature actuator will help push the envelope of the state of the art. Chapter 9 continues further with the introduction of several robotic prototypes utilizing granular jamming, and Chapter 8 describes several control schemes which can be used to control these actuators and robotic prototypes.

This research project aimed to develop a snake-like soft robot for minimally invasive surgeries (MIS), including the development of soft actuators and variable stiffness mech-

anisms. This was achieved with a granular jamming mechanism integrated into a pneumatic muscle actuator. With each stiffness chamber or actuator independent from each other, the stiffness along the robot can also be controlled independently. In other words, this provides the manipulator the key advantage of stiffening its distal tip and base sections, while keeping the middle sections soft. Moreover, the rigidity of each chamber can be tuned to a range of stiffness levels by varying the vacuum pressure within the membrane. Thus, the robot need not only transition from fluid-like to solid-like states, but take advantage of the wide range in between. This is particularly useful for integrating impedance control to the robot. Lastly, the developed prototypes, such as the Core-Snake, were made with sterilizable materials and only 10 mm in diameter, paving the way for robotic granular jamming to move further into the viability for MIS and other medical applications.

Future Work

Future work include further in-depth investigations of granular dynamics and statics. Quantitative and simulated data should be gathered to better understand the effects of granule size, shape, material, and surface properties in each degree of freedom. This will provide a detailed guideline to designing snake-like manipulators. Likewise, further investigations with the membrane and membrane coupling should be performed.

Miniaturization and sterilization must also be further investigated for the granular jamming system, if it is to be used in a medical context.

Ultimately, the prototypes introduced in this thesis should undergo additional research and development to optimize their systems and effectiveness in the field. This future prospect includes fusion with other technologies, such as force sensors to provide the jamming device with another feedback mechanism.

Appendix A

Publications

The work done in this thesis has lead to many contributions in the field of soft robotics, variable stiffness mechanisms, and granular jamming. The contributions include 8 conference papers and 2 journal papers as the principle investigator. Additional co-authored work has been done in tactile sensors, haptics, and impedance control.

Journal Papers

- A. Jiang, T. Ranzani, G. Gerboni, L. Lekstutyte, K. Althoefer, P. Dasgupta, and T. Nanayakkara, "Membrane analysis for robotic granular jamming," Soft Robotics (SoRo), 2014

- A. Jiang, P. Dasgupta, K. Althoefer, and T. Nanayakkara, "Robotic Granular Jamming: A New Variable Stiffness Mechanism," Journal of Robotics Society of Japan, 2014.

Conference Papers

- A. Jiang, S. Adejokun, A. Faragasso, K. Althoefer, P. Dasgupta, T. Nanayakkara, "The granular jamming integrated actuator," International Conference on Advanced Robotics and Intelligent Systems (ARIS 2014), Taipei, Taiwan, 2014.

- A. Jiang, T. Aste, P. Dasgupta, K. Althoefer, and T. Nanayakkara, "Granular jamming with hydraulic control" ASME 2013 International Design Engineering Technical Conferences & Computers and Information in Engineering Conference (IDETC 2013), Portland, OR, USA, 2013.

- A. Jiang, T. Aste, P. Dasgupta, K. Althoefer, and T. Nanayakkara, "Granular jamming transitions for a robotic mechanism," Powders & Grains 2013, Sydney, Australia, 2013.

- A. Jiang, P. Agrawal, K. Althoefer, T. Nanayakkara, P. Dasgupta, "Bio-inspired connective granular jamming for a robotic limb," 35th International Conference of the IEEE Engineering in Medicine and Biology Society (EMBC 2013), Osaka, Japan, 2013.

- A. Jiang, K. Althoefer, P. Dasgupta, T. Nanayakkara, "The Core-Snake, the variable stiffness laparoscopic camera," The Hamlyn Symposium on Medical Robotics, London, United Kingdom, 2013.

- A. Jiang, G. Xynogalas, P. Dasgupta, K. Althoefer, and T. Nanayakkara, "Design of a variable stiffness flexible manipulator with composite granular jamming and membrane coupling," IEEE/RSJ International Conference on Intelligent Robots and Systems (IROS 2012), Vilamoura, Portugal, 2012.

- A. Jiang, J. Bimbo, S. Goulder, H. Liu, X. Song, and T. Nanayakkara, "Adaptive grip control on an uncertain object," IEEE/RSJ International Conference on Intelligent Robots and Systems (IROS 2012), Vilamoura, Portugal, 2012.

- A. Jiang, K. Althoefer, T. Nanayakkara, and P. Dasgupta, "Granular jamming for minimally invasive surgeries," 30th World Congress of Endourology and SWL (WCE 2012), Istanbul, Turkey, 2012.

- A. Jiang, A. Ataollahi, K. Althoefer, P. Dasgupta, and T. Nanayakkara, "A variable stiffness joint by granular jamming," ASME 2012 International Design Engineering Technical Conferences & Computers and Information in Engineering Conference (IDETC 2012), Chicago, IL, USA, 2012.

Conference Workshop Papers

- A. Jiang, E. Secco, H. Wurdemann, T. Nanayakkara, P. Dasgupta, K. Athoefer, "Stiffness-controllable octopus-like robot arm for minimally invasive surgery," 3rd Joint Workshop on New Technologies for Computer/Robot Assisted Surgery (CRAS 2013), Verona, Italy, 2013.

- H.A. Wurdemann, A. Jiang, T. Nanayakkara, L.D. Seneviratne, K. Althoefer, "Variable Stiffness Controllable and Learnable Manipulator for MIS," IEEE International Conference on Robotics and Automation (ICRA 2012) Workshop, St Paul, MN, USA, 2012.

Co-authored Papers

- T. Nanayakkara, A. Jiang, M. D. R. Armas Fernandez, and J. Bimbo, "Stable Grip Control on Soft Objects With Time Varying Impedance," IEEE Transactions on Robotics, 2014

- M. Li, H. Liu, A. Jiang, L. Seneviratne, P. Dasgupta, K. Althoefer, and H. Wurdemann, "Intra-operative tumour localisation in robot-assisted minimally invasive surgery: a review," Journal of Engineering in Medicine, 2014.

- M. Li, J. Konstantinova, E. L. Secco, A. Jiang, H. Liu, T. Nanayakkara, L. D. Seneviratne, P. Dasgupta, and K. Althoefer, "Combining Pseudo-Haptic and Force Feedback to Enhance Haptic Feedback," Journal of Mechanical Engineering Science, 2014

- J. Konstantinova, A. Jiang, K. Althoefer, P. Dasgupta, and T. Nanayakkara, "Implementation of Tactile Sensing for Robot-Assisted Minimally Invasive Surgery," Sensors Journal, IEEE, 2013

- H. Xie, A. Jiang, H. Wurdemann, H. Liu, L. Seneviratne, K. Althoefer, "Magnetic Resonance-Compatible Tactile Force Sensor using Fiber Optics and Vision Sensor," Sensors Journal, IEEE, vol.PP, no.99, pp.1,1, 0

- S. Sareh, A. Jiang, A. Faragasso, Y. Noh, T. Nanayakkara, P. Dasgupta, L.D Seneviratne, H.A. Wurdemann, K. Althoefer, "Bio-Inspired Tactile Sensor Sleeve for Surgical Soft Manipulators," IEEE International Conference on Robotics and Automation (ICRA 2014), Hong Kong, China, 2014

- A. Faragasso, J. Bimbo, Y. Noh, A. Jiang, S. Sareh, H. Liu, T. Nanayakkara, H. A. Wurdemann, K. Althoefer, "Novel Uniaxial Force Sensor based on Visual Information for Minimally Invasive Surgery," IEEE International Conference on Robotics and Automation (ICRA 2014), Hong Kong, China, 2014

- H. Xie, A. Jiang, L. Seneviratne, and K. Althoefer, "Pixel-based Optical Fiber Tactile Force Sensor for Robot Manipulation," IEEE Sensors 2012, Taipei, Taiwan, 2012.

- F. Bianchi, G. Bartoli, K. Shoar, M. R. A. Fernandez, V. Pereno, J. Zirjakova, A. Jiang, and T. Nanayakkara, "Adaptive internal impedance control for stable walking on uncertain visco-elastic terrains," IEEE/RSJ International Conference on Intelligent Robots and Systems (IROS 2012), Vilamoura, Portugal, 2012.

Bibliography

[1] D. L. Willis, M. L. Gonzalgo, M. Brotzman, Z. Feng, B. Trock, and L.-M. Su, "Comparison of outcomes between pure laparoscopic vs robot-assisted laparoscopic radical prostatectomy: a study of comparative effectiveness based upon validated quality of life outcomes," *BJU International*, vol. 109, pp. 898–905, 2011.

[2] C. K. Rowe, M. W. Pierce, K. C. Tecci, C. S. Houck, J. Mandell, A. Retik, and H. T. Nguyen, "A comparative direct cost analysis of pediatric urologic robot-assisted laparoscopic surgery vs. open surgery: Could robotic surgery be less expensive?" *Journal of Endourology*, 2011.

[3] J. Moreira-Pinto, A. Ferreira, C. Rolanda, and J. Correia-Pinto, "Natural orifice transesophageal endoscopic surgery: State of the art," *Minimally Invasive Surgery*, vol. 2012, 2012.

[4] L. Vyas, D. Aquino, C. H. Kuo, J. S. Dai, and P. Dasgupta, "Flexible robotics," *Bju International*, vol. 107, no. 2, pp. 187–189, 2011.

[5] E. Auyang, B. Santos, D. Enter, E. Hungness, and N. Soper, "Natural orifice translumenal endoscopic surgery (notes): a technical review," *Surgical Endoscopy*, vol. 25, pp. 3135–3148, 2011.

[6] A. Loeve, P. Breedveld, and J. Dankelman, "Scopes too flexible...and too stiff," *Pulse, IEEE*, vol. 1, no. 3, pp. 26 –41, nov.-dec. 2010.

[7] A. J. Liu and S. R. Nagel, "Nonlinear dynamics: Jamming is not just cool any more," *Nature*, vol. 296, pp. 21–22, 1998.

[8] T. Aste and D. Weaire, *The pursuit of perfect packing*. Taylor & Francis, 2008.

[9] K. Chinzei, N. Hata, F. Jolesz, and R. Kikinis, "Mr compatible surgical assist robot: System integration and preliminary feasibility study," in *Medical Image Computing and Computer-Assisted Intervention–MICCAI 2000*. Springer, 2000.

[10] G. S. Fischer, I. Iordachita, C. Csoma, J. Tokuda, S. P. DiMaio, C. M. Tempany, N. Hata, and G. Fichtinger, "Mri-compatible pneumatic robot for transperineal prostate needle placement," *Mechatronics, IEEE/ASME Transactions on*, vol. 13, no. 3, pp. 295–305, 2008.

[11] D. Stoianovici, D. Song, D. Petrisor, D. Ursu, D. Mazilu, M. Mutener, M. Schar, and A. Patriciu, "Mri stealth robot for prostate interventions," *Minimally Invasive Therapy & Allied Technologies*, vol. 16, no. 4, pp. 241–248, 2007.

[12] F. Daerden and D. Lefeber, "Pneumatic artificial muscles: actuators for robotics and automation," *European journal of mechanical and environmental engineering*, vol. 47, pp. 11–21, 2002.

[13] G. Robinson and J. B. C. Davies, "Continuum robots - a state of the art," *Icra '99: Ieee International Conference on Robotics and Automation, Vols 1-4, Proceedings*, pp. 2849–2854, 1999.

[14] W. McMahan, B. Jones, I. Walker, V. Chitrakaran, A. Seshadri, and D. Dawson,

Robotic manipulators inspired by cephalopod limbs. Montreal, Canada: Citeseer, 2004, pp. 1–10.

[15] D. B. Camarillo, C. F. Milne, C. R. Carlson, M. R. Zinn, and J. K. Salisbury, "Mechanics modeling of tendon-driven continuum manipulators," *Ieee Transactions on Robotics*, vol. 24, no. 6, pp. 1262–1273, 2008.

[16] R. J. Webster, J. M. Romano, and N. J. Cowan, "Mechanics of precurved-tube continuum robots," *Ieee Transactions on Robotics*, vol. 25, no. 1, pp. 67–78, 2009.

[17] A. Degani, H. Choset, A. Wolf, and M. A. Zenati, "Highly articulated robotic probe for minimally invasive surgery," *2006 Ieee International Conference on Robotics and Automation (Icra), Vols 1-10*, pp. 4167–4172, 2006.

[18] D. Noonan, "Design of a hybrid joint module for a flexible access platform for mis," *Hamlyn Symposium on Medical Robotics*, p. 2, 2011.

[19] N. Simaan, "Snake-like units using flexible backbones and actuation redundancy for enhanced miniaturization," *2005 IEEE International Conference on Robotics and Automation (ICRA), Vols 1-4*, pp. 3012–3017, 2005.

[20] K. Ning and F. Worgotter, "A novel concept for building a hyper-redundant chain robot," *Robotics, IEEE Transactions on*, vol. 25, no. 6, pp. 1237 –1248, dec. 2009.

[21] A. Degani, H. Choset, B. Zubiate, T. Ota, and M. Zenati, "Highly articulated robotic probe for minimally invasive surgery," *2008 30th Annual International Conference of the IEEE Engineering in Medicine and Biology Society, Vols 1-8*, pp. 3273–3276, 2008.

[22] A. J. Loeve, O. S. van de Ven, J. G. Vogel, P. Breedveld, and J. Dankelman, "Vacuum packed particles as flexible edoscope guides with controllable rigidity," *Granular Matter*, vol. 12, pp. 543–554, 2010.

[23] J. Kobayashi, K. Okumura, Y. Watanabe, and N. Suzuki, "Development of variable stiffness joint drive module and experimental results of joint angle control," *Proc. of The Fifteenth International Symposium on Artificial Life and Robotics*, pp. 946–949, 2010.

[24] S. Wolf and G. Hirzinger, "A new variable stiffness design: Matching requirements of the next robot generation," *2008 Ieee International Conference on Robotics and Automation, Vols 1-9*, pp. 1741–1746, 2008.

[25] N. Cheng, G. Ishigami, S. Hawthorne, H. Chen, M. Hansen, M. Telleria, R. Playter, and K. Iagnemma, "Design and analysis of a soft mobile robot composed of multiple thermally activated joints driven by a single actuator," *2010 IEEE International Conference on Robotics and Automation (ICRA)*, pp. 5207–5212, 2010.

[26] R. Webster, A. M. Okamura, and N. J. Cowan, "Toward active cannulas: Miniature snake-like surgical robots," in *Intelligent Robots and Systems, 2006 IEEE/RSJ International Conference on*. IEEE, 2006, pp. 2857–2863.

[27] P. Dupont, J. Lock, B. Itkowitz, and E. Butler, "Design and control of concentric-tube robots," *Robotics, IEEE Transactions on*, vol. 26, no. 2, pp. 209 –225, april 2010.

[28] Y.-J. Kim, S. Cheng, S. Kim, and K. Iagnemma, "Design of a tubular snake-like manipulator with stiffening capability by layer jamming," in *Intelligent Robots and*

Systems (IROS), 2012 IEEE/RSJ International Conference on, oct. 2012, pp. 4251 –4256.

[29] E. Brown, N. Rodenberg, J. Amend, A. Mozeika, E. Steltz, M. R. Zakin, H. Lipson, and H. M. Jaeger, "Universal robotic gripper based on the jamming of granular material," *Proceedings of the National Academy of Sciences of the United States of America*, vol. 107, no. 44, pp. 18 809–18 814, 2010.

[30] N. G. Cheng, M. B. Lobovsky, S. J. Keating, A. M. Setapen, K. I. Gero, A. E. Hosoi, and K. D. Iagnemma, "Design and analysis of a robust, low-cost, highly articulated manipulator enabled by jamming of granular media," *2012 IEEE International Conference on Robotics and Automation (ICRA)*, pp. 4328 –4333, May 2012.

[31] E. Steltz, A. Mozeika, N. Rodenberg, E. Brown, and H. Jaeger, "Jsel: Jamming skin enabled locomotion," in *Intelligent Robots and Systems, 2009. IROS 2009. IEEE/RSJ International Conference on*, oct. 2009, pp. 5672 –5677.

[32] R. Letts and D. Hobson, "The vacuum splint: an aid in emergency splinting of fractures," *Canadian Medical Association Journal*, vol. 109, no. 7, p. 599, 1973.

[33] T. Mitsuda, S. Kuge, M. Wakabayashi, and S. Kawamura, "Wearable haptic display by the use of a particle mechanical constraint," *Proceedings. 10th Symposium on HAPTICS 2002*, pp. 153–158, 2002.

[34] A. Mazzone, C. Spagno, and A. Kunz, "The hovermesh: a deformable structure based on vacuum cells: new advances in the research of tangible user interfaces," in *Proceedings of the 2004 ACM SIGCHI International Conference on Advances in computer entertainment technology*. ACM, 2004, pp. 187–193.

[35] S. Follmer, D. Leithinger, A. Olwal, N. Cheng, and H. Ishii, "Jamming user interfaces: programmable particle stiffness and sensing for malleable and shape-changing devices," in *Proceedings of the 25th annual ACM symposium on User interface software and technology*. ACM, 2012, pp. 519–528.

[36] J. R. Amend, E. M. Brown, N. Rodenberg, H. M. Jaeger, and H. Lipson, "A positive pressure universal gripper based on the jamming of granular material," *Robotics, IEEE Transactions on*, vol. 28, no. 2, pp. 341–350, 2012.

[37] E. Steltz, A. Mozeika, J. Rembisz, N. Corson, and H. Jaeger, "Jamming as an enabling technology for soft robotics," in *Society of Photo-Optical Instrumentation Engineers (SPIE) Conference Series*, vol. 7642, 2010, p. 63.

[38] S. Edwards and D. Grinev, "Statistical mechanics of granular materials: stress propagation and distribution of contact forces," *Granular Matter*, vol. 4, no. 4, pp. 147–153, 2003.

[39] S. Edwards, D. Grinev, and J. Brujic, "Fundamental problems in statistical physics of jammed packings," *Physica a-Statistical Mechanics and Its Applications*, vol. 330, no. 1-2, pp. 61–76, 2003.

[40] M. Ciamarra, R. Pastore, M. Nicodemi, and A. Coniglio, "Jamming phase diagram for frictional particles," *Arxiv preprint arXiv:0912.3140*, 2009.

[41] R. Guises, J. Xiang, J.-P. Latham, and A. Munjiza, "Granular packing: numerical simulation and the characterisation of the effect of particle shape," *Granular Matter*, vol. 11, pp. 281–292, 2009.

[42] M. Saadatfar, "Computer simulation of granular materials," *Computing in Science Engineering*, vol. 11, no. 1, pp. 66 –74, jan.-feb. 2009.

[43] M. Z. Miskin and H. M. Jaeger, "Adapting granular materials through artificial evolution," *Nature materials*, 2013.

[44] M. Jerkins, M. Schröter, H. Swinney, T. Senden, M. Saadatfar, and T. Aste, "Onset of mechanical stability in random packings of frictional spheres," *Physical review letters*, vol. 101, no. 1, p. 18301, 2008.

[45] L. Goren, E. Aharonov, D. Sparks, and R. Toussaint, "The mechanical coupling of fluid-filled granular material under shear," *Pure and Applied Geophysics*, vol. 168, no. 12, pp. 2289–2323, 2011.

[46] P. Mills and P. Snabre, "Apparent viscosity and particle pressure of a concentrated suspension of non-brownian hard spheres near the jamming transition," *The European Physical Journal E*, vol. 30, pp. 309–316, 2009.

[47] O. Pouliquen, C. Cassar, P. Jop, Y. Forterre, and M. Nicolas, "Flow of dense granular material: towards simple constitutive laws," *Journal of Statistical Mechanics: Theory and Experiment*, vol. 2006, no. 07, p. P07020, 2006.

[48] Y. Yurkovetsky and J. Morris, "Particle pressure in sheared brownian suspensions," *Journal of rheology*, vol. 52, no. 1, pp. 141–164, 2008.

[49] P. W. Rowe, "The stress-dilatancy relation for static equilibrium of an assembly of particles in contact," *Proceedings of the Royal Society of London. Series A. Mathematical and Physical Sciences*, vol. 269, no. 1339, pp. 500–527, 1962.

[50] J. Amend Jr, E. Brown, N. Rodenberg, H. Jaeger, and H. Lipson, "A positive pressure universal gripper based on the jamming of granular material," *IEEE Transactions on Robotics, to appear*, 2012.

[51] A. L. Brody and K. S. Marsh, *The Wiley Encyclopedia of Packaging Technology*, 3rd ed., K. L. Yam, Ed. Wiley-Interscience, 2009.

[52] W. F. Gutmann, "Relationships between invertebrate phyla based on functional-mechanical analysis of the hydrostatic skeleton," *American zoologist*, vol. 21, no. 1, pp. 63–81, 1981.

[53] A. Jiang, P. Agrawal, K. Althoefer, T. Nanayakkara, and P. Dasgupta, "Bio-inspired connective granular jamming for a robotic limb," *Transactions of Japanese Society for Medical and Biological Engineering*, vol. 51, no. Supplement, pp. R–270–R–270, 2013.

[54] W. M. Kier and M. P. Stella, "The arrangement and function of octopus arm musculature and connective tissue," *Journal of Morphology*, vol. 268, no. 10, pp. 831–843, 2007.

[55] A. Jiang, G. Xynogalas, P. Dasgupta, K. Althoefer, and T. Nanayakkara, "Design of a variable stiffness flexible manipulator with composite granular jamming and membrane coupling," in *Intelligent Robots and Systems (IROS), 2012 IEEE/RSJ International Conference on*, oct. 2012, pp. 2922 –2927.

[56] A. Jiang, A. Ataollahi, K. Althoefer, P. Dasgupta, and T. Nanayakkara, "A variable stiffness joint by granular jamming," in *Proceedings of the ASME 2012 International Design Engineering Technical Conferences & Computers and Information in Engineering Conference IDETC/CIE 2012*, vol. 4, no. 36, August 2012, pp. 267–275.

[57] M. Johnson and M. Beatty, "The mullins effect in uniaxial extension and its in-

fluence on the transverse vibration of a rubber string," *Continuum Mechanics and Thermodynamics*, vol. 5, no. 2, pp. 83–115, 1993.

[58] A. Jiang, K. Althoefer, T. Nanayakkara, and P. Dasgupta, "Granular jamming for minimally invasive surgeries," in *30th World Congress of Endourology and SWL (WCE 2012)*, ser. P1-A572, vol. 26, no. S1, August 2012, pp. A403–A404.

[59] H. Wurdemann, A. Jiang, T. Nanayakkara, L. Seneviratne, and K. Althoefer, "Variable stiffness controllable and learnable manipulator for mis," in *IEEE International Conference on Robotics and Automation (ICRA 2012) Workshop*, 2012.

[60] D. P. Noonan, V. Vitiello, J. Shang, C. J. Payne, and G.-Z. Yang, "A modular, mechatronic joint design for a flexible access platform for mis," in *Intelligent Robots and Systems (IROS), 2011 IEEE/RSJ International Conference on*, sept. 2011, pp. 949 –954.

[61] C. Kuo, R. Taylor, J. Dai, and I. Iordachita, "Design of a flexural transmission for a dexterous telesurgical robot for throat and upper airway: a preliminary result," in *Proc. of the Hamlyn Symposium on Medical Robotics*, 2010, pp. 71–72.

[62] A. Jiang, T. Aste, P. Dasgupta, K. Althoefer, and T. Nanayakkara, "Granular jamming transitions for a robotic mechanism," *AIP Conference Proceedings*, vol. 1542, no. 1, pp. 385–388, 2013.

[63] ——, "Granular jamming with hydraulc control," in *Proceedings of the ASME 2013 International Design Engineering Technical Conferences & Computers and Information in Engineering Conference IDETC/CIE 2013*, ser. 37, vol. 4, August 2013.

[64] A. Jiang, K. Althoefer, P. Dasgupta, and T. Nanayakkara, "The core-snake, the variable stiffness laparoscopic camera," in *Proceedings of the Hamlyn Symposium on Medical Robotics*, vol. 7, June 2013, pp. 121–122.

[65] N. Hogan, "Impedance control: An approach to manipulation: Part i-theory," *Journal of dynamic systems, measurement, and control*, vol. 107, no. 2, p. 1, 1985.

[66] ——, "Impedance control: An approach to manipulation: Part ii-implementation," *Journal of Dynamic Systems, Measurement, and Control*, vol. 107, no. 1, pp. 8–16, 1985.

[67] ——, "Impedance control: An approach to manipulation: Part iii-applications," *Journal of dynamic systems, measurement, and control*, vol. 107, no. 2, p. 17, 1985.

[68] S. Tafazoli, S. E. Salcudean, K. Hashtrudi-Zaad, and P. D. Lawrence, "Impedance control of a teleoperated excavator," *Control Systems Technology, IEEE Transactions on*, vol. 10, no. 3, pp. 355–367, 2002.

[69] N. G. Tsagarakis and D. G. Caldwell, "Development and control of a soft-actuated exoskeleton for use in physiotherapy and training," *Autonomous Robots*, vol. 15, no. 1, pp. 21–33, 2003.

[70] Y. Yang, L. Wang, J. Tong, and L. Zhang, "Arm rehabilitation robot impedance control and experimentation," in *Robotics and Biomimetics, 2006. ROBIO'06. IEEE International Conference on*. IEEE, 2006, pp. 914–918.

[71] J. W. Sensinger and R. F. Weir, "User-modulated impedance control of a prosthetic elbow in unconstrained, perturbed motion," *Biomedical Engineering, IEEE Transactions on*, vol. 55, no. 3, pp. 1043–1055, 2008.

[72] G. Aguirre-Ollinger, J. E. Colgate, M. A. Peshkin, and A. Goswami, "Active-impedance control of a lower-limb assistive exoskeleton," in *Rehabilitation Robotics, 2007. ICORR 2007. IEEE 10th International Conference on*. IEEE, 2007, pp. 188–195.

[73] H.-o. Lim, S. A. Setiawan, and A. Takanishi, "Balance and impedance control for biped humanoid robot locomotion," in *Intelligent Robots and Systems, 2001. Proceedings. 2001 IEEE/RSJ International Conference on*, vol. 1. IEEE, 2001, pp. 494–499.

[74] S. Lee and H. S. Lee, "Intelligent control of manipulators interfacing with an uncertain environment based on generalized impedance," in *Proceedings of the IEEE International Symposium on Intelligent Control*, 1999, pp. 61–66.

[75] R. J. Bickel and M. Tomizuka, "Disturbance observer based hybrid impedance control," in *American Control Conference, 1995. Proceedings of the*, vol. 1. IEEE, 1995, pp. 729–733.

[76] A. Saxena, J. Driemeyer, J. Kearns, C. Osondu, and A. Y. Ng, "Learning to grasp novel objects using vision," in *10th International Symposium of Experimental Robotics (ISER)*, 2006.

[77] S. Hirai, T. Tsuboi, and T. Wada, "Robust grasping manipulation of deformable objects," in *Assembly and Task Planning, 2001, Proceedings of the IEEE International Symposium on*. IEEE, 2001, pp. 411–416.

[78] N. Mimura and Y. Funahashi, "Parameter identification of contact conditions by active force sensing," in *Robotics and Automation, 1994. Proceedings., 1994 IEEE International Conference on*. IEEE, 1994, pp. 2645–2650.

[79] A. Petrovskaya, O. Khatib, S. Thrun, and A. Y. Ng, "Bayesian estimation for autonomous object manipulation based on tactile sensors," in *Robotics and Automation, 2006. ICRA 2006. Proceedings 2006 IEEE International Conference on*. IEEE, 2006, pp. 707–714.

[80] J. Laaksonen and V. Kyrki, "Probabilistic approach to sensor-based grasping," in *ICRA 2011 Workshop on Manipulation Under Uncertainty*, 2011.

[81] P. R. Pagilla and M. Tomizuka, "Adaptive control of two robot arms carrying an unknown object," in *Robotics and Automation, 1995. Proceedings., 1995 IEEE International Conference on*, vol. 1. IEEE, 1995, pp. 597–602.

[82] V. N. Christopoulos and P. Schrater, "Handling shape and contact location uncertainty in grasping two-dimensional planar objects," in *Intelligent Robots and Systems, 2007. IROS 2007. IEEE/RSJ International Conference on*. IEEE, 2007, pp. 1557–1563.

[83] F. Stulp, E. Theodorou, J. Buchli, and S. Schaal, "Learning to grasp under uncertainty," in *Robotics and Automation (ICRA), 2011 IEEE International Conference on*. IEEE, 2011, pp. 5703–5708.

[84] R. Kikuuwe and T. Yoshikawa, "Robot perception of environment impedance," in *Robotics and Automation, 2002. Proceedings. ICRA'02. IEEE International Conference on*, vol. 2. IEEE, 2002, pp. 1661–1666.

[85] Z.-H. Jiang, "Impedance control of flexible robot arms with parametric uncertainties," *Journal of Intelligent and Robotic Systems*, vol. 42, no. 2, pp. 113–133, 2005.

[86] D. T. Nanayakkara, K. Kiguchi, T. Murakami, K. Watanabe, and K. Izumi, "Enhancing the autonomy of teleoperated redundant manipulators through fusion of

intelligent control modules," *Journal of Robotics and Mechatronics*, vol. 14, no. 3, pp. 278–289, 2002.

[87] S. Chan, B. Yao, W. Gao, and M. Cheng, "Robust impedance control of robot manipulators." *International Journal of Robotics & Automation*, vol. 6, no. 4, pp. 220–227, 1991.

[88] Y. Kishi, Z. W. Luo, F. Asano, and S. Hosoe, "Passive impedance control with time-varying impedance center," in *Computational Intelligence in Robotics and Automation, 2003. Proceedings. 2003 IEEE International Symposium on*, vol. 3. IEEE, 2003, pp. 1207–1212.

[89] C. D. Takahashi, R. A. Scheidt, and D. J. Reinkensmeyer, "Impedance control and internal model formation when reaching in a randomly varying dynamical environment," *J. Neurophysiol*, vol. 86, pp. 1047–1051, 2001.

[90] T. Nanayakkara and R. Shadmehr, "Saccade adaptation in response to altered arm dynamics," *Journal of neurophysiology*, vol. 90, no. 6, pp. 4016–4021, 2003.

[91] G. Sing, W. Joiner, T. Nanayakkara, J. Brayanov, and M. Smith, "Primitives for motor adaptation reflect correlated neural turning to position and velocity," *Neuron*, vol. 64, no. 4, pp. 575 – 589, 2009.

[92] K. Hsiao, T. Lozano-Pérez, and L. P. Kaelbling, "Robust belief-based execution of manipulation programs," in *Eighth Intl. Workshop on the Algorithmic Foundations of Robotics*. Citeseer, 2008.

[93] A. Jiang, J. Bimbo, S. Goulder, H. Liu, X. Song, P. Dasgupta, K. Althoefer, and T. Nanayakkara, "Adaptive grip control on an uncertain object," in *Intelligent*

Robots and Systems (IROS), 2012 IEEE/RSJ International Conference on. IEEE, 2012, pp. 1161–1166.

[94] R. Tinós and S. Yang, "Use of the q-gaussian mutation in evolutionary algorithms," *Soft Computing*, vol. 15, no. 8, pp. 1523–1549, 2011.

[95] K. Worden, C. Wong, U. Parlitz, A. Hornstein, D. Engster, T. Tjahjowidodo, F. Al-Bender, D. Rizos, and S. Fassois, "Identification of pre-sliding and sliding friction dynamics: Grey box and black-box models," *Mechanical systems and signal Processing*, vol. 21, no. 1, pp. 514–534, 2007.

[96] K. Johanastrom and C. Canudas-De-Wit, "Revisiting the lugre friction model," *Control Systems, IEEE*, vol. 28, no. 6, pp. 101–114, 2008.

[97] V. C. Chang, S.-J. Tang, C. P. Swain, R. Bergs, J. Paramo, D. C. Hogg, R. Fernandez, J. A. Cadeddu, and D. J. Scott, "A randomized comparison of laparoscopic, flexible endoscopic, and wired and wireless magnetic cameras on ex vivo and in vivo notes surgical performance," *Surgical innovation*, 2012.

[98] J. Cartmill, A. Shakeshaft, W. Walsh, and C. Martin, "High pressures are generated at the tip of laparoscopic graspers," *AUSTRALIAN AND NEW ZEALAND JOURNAL OF SURGERY*, vol. 69, no. 2, pp. 127–130, FEB 1999.

[99] M. Osaki, T. Takayama, T. Omata, T. Ohya, K. Kojima, K. Takase, and N. Tanaka, "Single-trocar assemblable retractor-hand for laparoscopic surgery," in *Robotics and Automation, 2009. ICRA '09. IEEE International Conference on*, may 2009, pp. 3490 –3495.

[100] G. Petroni, M. Niccolini, A. Menciassi, P. Dario, and A. Cuschieri, "A novel intra-

corporeal assembling robotic system for single-port laparoscopic surgery," *Surgical Endoscopy*, pp. 1–6, 2012.

[101] R. Oshima, T. Takayama, T. Omata, K. Kojima, K. Takase, and N. Tanaka, "Assemblable three-fingerednine-degrees-of-freedomhand for laparoscopic surgery," *Mechatronics, IEEE/ASME Transactions on*, vol. 15, no. 6, pp. 862–870, 2010.

[102] R. Deimel and O. Brock, "A compliant hand based on a novel pneumatic actuator," in *2013 IEEE International Conference on Robotics and Automation (ICRA)*, May 2013.

[103] R. V. Martinez, J. L. Branch, C. R. Fish, L. Jin, R. F. Shepherd, R. Nunes, Z. Suo, and G. M. Whitesides, "Robotic tentacles with three-dimensional mobility based on flexible elastomers," *Advanced Materials*, 2012.

[104] F. Ilievski, A. D. Mazzeo, R. F. Shepherd, X. Chen, and G. M. Whitesides, "Soft robotics for chemists," *Angewandte Chemie*, vol. 123, no. 8, pp. 1930–1935, 2011.